Department of
Electronic and
Electrical
Engineering

The University of Sheffield

Time-Modulated Reflector-Arrays

A thesis submitted for the Degree of Doctor of Philosophy

PhD Candidate: Yang Wang
Student registration number: 100256112
Supervisor: Dr A. Tennant
Second supervisor: Prof. R.J. Langley
Internal examiner: Dr. S. Khamas
External examiner: Dr. James Flint

ACKNOWLEDGEMENTS

I would like to show my best regards and gratitude to my supervisor Dr Alan Tennant. Without his support, encourage, commitment and friendship I would not have been able to complete this research.

I would like to thank every one of you in communications group and the department. Being with you, I would able to finish this research with joy, friendship and happiness.

I would like to thank my family: my parents, grandparents, uncles, aunts, cousins for understanding and supporting me. Especially I would like to thank my wife Simo who encourage, help and comfort me throughout every steps of my PhD.

ABSTRACT

This PhD thesis introduces the time-modulated reflector-arrays which are a hybrid of conventional time-modulated array (TMA) systems and reflectarrays. The TMRAs use a similar layout of reflectarray feed by a source. Compared to conventional phased arrays, reflectarrays and time-modulated arrays, a TMRA is potentially simpler to implement in hardware as it does not need a complicated feeding network or the use of the phase shifting units. Instead of phase shifting units, TMRAs use discrete time-switching to achieve beamforming functions. The concept and operating mechanism of the TMRA is explained using a simple model based on isotropic scatterers. A more sophisticated TMRA based on an 8 element array of PIN-diode controlled bow-tie dipole elements is designed and analysed using a full-wave commercial simulator. A hardware implementation of the bowtie dipole TMRA system, including control circuitry, is also described and measured data is presented. The simulated and measured results confirm that the time-modulated reflector array system performs the required function of harmonic beam steering. Moreover, TMRAs can provide functions such as sidelobe suppression and adaptive beamforming. The thesis also provide solutions to the challenges of TMRAs such as low system efficiency and phases variances caused by feeding paths. Overall TMRAs combine the benefits of conventional TMA systems and reflectarrays. They can provide similar functions of conventional TMAs, phased arrays and reflectarrays without the need of expensive phase shifters and lossy transmission lines. This makes TMRAs a very good candidates in applications over millimetre-wavelength frequency band.

PUBLICATIONS

[1] Yang Wang; Tennant, A.; , "Experimental time-modulated reflector array," IEEE Trans., Antennas and Propagation, Vol. 62 No. 12, Dec. 2014

[2] Yang Wang; Tennant, A.; , "LCMV Beamforming Applied to a Time-Modulated Reflector-Array: Concept and Simulations," The 5th IEEE International Symposium on Microwave, Antenna, Propagation, and EMC Technologies for Wireless Communications, Oct. 2013

[3] Alan Tennant; Y Tong; Y Wang;, "Time-Switched Arrays and Reflect-Arrays" Antennas and Propagation (APS), The 2014 IEEE International Symposium on, 2014 Memphis, 6-11 June 2014

[4] Yang Wang; Tennant, A.; , "Adaptive beamforming applied to time-modulated reflector array," Antennas and Propagation Conference (LAPC), 2013 Loughborough ,pp.1-4, Nov. 2013

[5] Yang Wang; Tennant, A.; , "Sidelobe control of time-modulated reflector array," Antennas and Propagation Conference (LAPC), 2012 Loughborough ,pp.1-4, Nov. 2012

[6] Yang Wang; Tennant, A.; , "Time-modulated reflector array," Electronics Letters , vol.48, no.16, pp.972-974, August 2 2012

[7] Yang Wang; Tennant, A.; Langley, R.; , "Direction dependent modulation of an RFID tag," *Antennas and Propagation (EUCAP), Proceedings of the 6th European Conference on* , 2012

[8] Yang Wang; Tennant, A.; Langley, R.; , "A phase-modulating RF tag," Antennas and Propagation Conference (LAPC), 2011 Loughborough , vol., no., pp.1-4, 14-15 Nov. 2011

CONTENTS

LIST OF ACRONYMS

AF	Array Factor
CW	Continuous Wave
dB	decibel
DOA	Direction of Arrival
FET	Field-effect transistor
FSS	Frequency Selective Surface
GA	Genetic Algorithm
Harmo.	Harmonic
JNR	Jammer Noise Ratio
LC	Liquid Crystal
LCMV	Linear constrains minimum variance
LMS	Least Mean Square
LNA	Low Noise Amplifier
MVDR	Minimum variance differential response
NRL	Navy Research Laboratory
PCB	Printed Circuit Board
RF	Radio Frequency
RECAP	Reconfigurable Aperture
Rx	Receiving

SLL	Side Lobe Level
SNR	Signal Noise Ratio
SBM	Single-board microprocessor
SPST	Single Pole Single Throw
TMA	Time Modulated Array
TMRA	Time Modulated Reflector Array
Tx	Transmitting
V.M.	Vector Modulator

LIST OF SYMBOLS

E	Radiation pattern
r_i	distance from the i-th element to field
j	square roof of -1
k	wavenumber/propagating constant
d	inter-element distance
θ	angle of direction from broadsight
φ	phase
$\boldsymbol{S_k}$	steering vector
$\boldsymbol{W}$	weight vector
$\boldsymbol{C}$	constraints matrix
$\vec{R}_{mn}$	element position vector
$\vec{r}_0$	direction of the desired beam
f	frequency
$I_n(t)$	Time wave form
a_n	element phase
A_n	element amplitude
$p(\theta)$	single element scattering pattern
b_n	element steer factor
t	time
T	time period
m	harmonic number

Chapter 1 INTRODUCTION

Nowadays, applications of electromagnetic science are everywhere in the daily life. Antenna systems, as an application of the electromagnetic science, are terminals to transmit and receive electromagnetic waves. The modern wireless communication industry requires antennas to be smart, compact, powerful, durable, affordable and etc. Antennas benefit from the boom of information technology, material science and fabrication engineering, have developed into devices in various layouts, geometry and material. The antenna can be a single antenna controlled by reconfigurable elements. Sometimes it is better to use multiple antennas, which are called antenna arrays, to provide functions that a single simple antenna cannot achieve.

The time-modulated reflector-arrays (TMRAs) consists of a feeding antenna and a grid of switch-controlled scatterers. By controlling the switches ON/OFF states, TMRAs aim to provide functions of conventional phased arrays such as adaptive beamforming, beam steering and sidelobe handling without the need of phase shifting units and cooperate feeding network. Comparing to phased arrays, TMRAs are simpler in hardware configurations, which makes TMRAs a cheaper approach in applications such as object tracking, direction finding, satellite communications and TV broadcasting. The absence of cooperate feeding network makes TMRAs a good choice in mm-wavelength applications.

1.1 Background and initiatives

The Time-modulated reflector-array is a member of time modulated arrays. The concept of time-modulated array (TMA) or time-switched array (TSA) was first proposed

in the late 1950s [**1**] by Shanks and Bickmore. They used a parabolic antenna with a fast notating primary horn feed to obtain a multi-pattern operation simultaneously at the fundamental frequency and the first sideband. Kummer et al. [**2**] developed the time-modulation concept to antenna arrays in 1963. The experimental prototype was an eight-element array of X band collinear slot antennas. The time modulation was realized by controlling the array elements' on-off states using switches in a pre-calculated sequence. They attained ultra-low sidelobes levels comparing to the results without sidelobe control [**2**]. The TMA has shown a great advantage in the control of aperture excitation since the time parameter can be easily and dynamically applied to the array elements. However, it must be noted that sidebands are generated when antennas are periodically switching between different states.

In recent years, scientists have adopted various approaches to reduce the amount of power radiated into the sideband frequencies and to increase the system power efficiency. A common approach is to use optimization algorithms to reduce the sideband radiation. J. C. Bregains *et al.* [**3**] formalized the mathematical model of a TMA and derived an expression for total sideband radiation used in the dynamic optimization. L. Poli et al. [**4**] used a method based on particle swarm optimization to minimize the power losses in time-modulated array. S. Yang et al. [**5**] adopted genetic algorithm to design a uniform amplitude TMA system with low sidelobe levels and low sideband levels simultaneously. Another approach to reduce sideband levels is to design a particular antenna configurations. In [**6**] L. Poli et al. demonstrate that sideband radiation was reduced by using a directive TMA, while Y. Tong and A. Tennant [**7**] suggest a technique based on half-power sub-arraying.

More recently, TMAs have been configured to mimic the functions of a conventional, electronically controlled phased array antenna. Phased arrays apply vector

weighting matrix to array elements using phase shifters. Instead, in TMAs, the vector weighting matrix are interpreted into elements switch ON/OFF times and beamforming can be achieved on the radiation patterns of harmonic frequencies. TMAs were demonstrated to provide functions such as beam steering [**8**], adaptive beamforming [**9**] and interference nulling [**10**]. TMA have also been applied to direction of arrival (DoA) estimation [**11**], direction finding [**12**] and multi-channel communication [**13**].

However, all the TMA systems reported in the open literature are configured to operate as variants of conventional antenna array systems in either transmitting or receiving mode. This thesis introduces a different topology: the Time-modulated Reflector-Arrays (TMRAs). Similar to traditional reflector arrays, the TMRA is illuminated by a feed. Without a complex corporate feed network used in phased arrays or TMAs, the TMRA is simpler to be embedded in hardware. However, compared to the conventional reflectarray the radiation characteristics of the array are managed by the elements' ON/OFF times instead of elements' phases. In other words, TMRAs use simple binary switches rather than expensive phase shifting units to realize the functions provided by conventional reflectarrays with minimum hardware. Moreover the TMRAs are able to provide an additional function to form the desired radiation patterns at multi-bands.

This thesis is the first report to introduce the concept of time-modulated reflector-arrays. The content covers the TMRA operating mechanism, functions, the numerical analysis, simulations, the TMRA prototype and measurements performance. The TMRA features powerful functions as beam steering, beamforming and sidelobe control with minimal hardware requirement. The idea is applicable on small scale device, e.g. RF tags, remote sensors. Moreover, the TMRA can be used on medium scale applications, e.g. multi-beam scanning sensors, retro-directive antenna, multi-channel stations. The

potential large and super large scale applications is the deep-space radio telescope station, weather monitor stations.

The contributions of the thesis are

(1) A proposal of the time modulated reflector arrays (TMRAs). The thesis provides a comprehensive analysis of TMRA system using numerical analysis, full wave simulations, prototype measurements.
(2) Sidelobe management of the time modulated reflector arrays. The thesis shows that the TMRA can reduce the side lobe radiation of a formed beam pattern.
(3) The time modulated reflector arrays performs the adaptive beamforming. The minimum variance differential response (MVDR) beamforming and linear constrains minimum variance (LCMV) beamforming were used in phased array and TMAs to form a desired beam. These two beamforming schemes have been successively reproduced on TMRAs. The TMRA can allocate the peaks and nulls of a beam pattern.
(4) A proposal of a parabolic TMRA. The planar TMRAs are assumed to be illuminated by a plane wave, which requires the feeding antenna must be placed in a farfield distance. However, parabolic TMRAs can have the feeding antenna placed at a close distance. The thesis show that parabolic TMRAs can perform the same functions of planar TMRA, without a sacrifice of performance.
(5) A proposal of a double layer TMRA. Single layer TMRAs has a low power efficiency as the radiation of the feeding antenna is 'wasted' when element is OFF (non-scattering state period). The thesis performed an efficiency study on TMRAs and propose double layer TMRAs to improve the system efficiency.

1.2 Thesis structure

The contents are arranged as follow,

Chapter 2 is the literature review. Section **2.1** reviews common approaches used in reconfigurable antennas or antenna arrays. Reconfigurable antennas benefit from active components to provide additional features comparing to passive antenna such as system

freedom, multi-functionalities and additional flexibility. Then the focus moves to antenna array system. Section **2.2** summarizes the concept, objectives, numerical analysis and current development of the antenna array, especially the phased array system. Section **2.3** reviews the history of time-modulated arrays, from the beginning of the invention to the most recent developments in the last two decades. The TMAs are compared with phased array systems in aspects of functions, system complexity and cost.

Chapter 3 introduces the concept of the time-modulated reflector array (TMRA) along with a numerical analysis. The chapter builds a theoretical model based on switchable isotropic elements, which is analysed using Fourier series and array factor theory. Such an ideal TMRA is modulated by a set of predefined periodical control sequences to provide a function of beam-steering on fundamental and harmonic frequencies. In addition, the report shows that the TMRA can also provide a pattern control function to reduce the side lobe radiation on the fundamental frequency.

Chapter 4 demonstrates an experimental TMRA prototype with simulation and measurement results. The proposed prototype consists of a grid of bow-tie dipole elements loaded with PIN diodes at the midpoint. Each element is switched between a scattering state and the non-scattering state by changing the direct current applied on the loaded PIN diode. By energizing the PIN diodes in predefined sequences, the TMRA is able to form desired scattering patterns. The prototype was simulated in a full wave electromagnetic simulator combined with numerical analysis. The experimental result was measured in a NLR arch reflectivity measurement system. The simulated and measured performances were compared with the theoretical results.

Chapter 5 applies adaptive beamforming algorithms to the TMRAs. Two popular beamforming techniques, Minimum Variance Distortionless Response (MVDR) beamforming and Linearly Constrained Minimum Variance (LCMV) beamforming, were

adopted to control the scattering pattern of the TMRA. A numerical analysis is given to build a connection between the conventional weighting matrix and the TMRA modulating sequence. By transferring the pre-existing weighting matrix to element switching ON/OFF times of the sequence, the TMRA can produce the beamforming functions using only simple switches. An example of the TMRA based on PIN diode loaded dipole elements is analysed using a full wave simulator. The simulated and theoretical results are provided to support the TMRA functionalities.

Chapter 6 introduces a parabolic TMRA. Previously, the feeding antenna of the TMRA was assumed to be placed in the farfield from the TMRA that every TMRA element scatterers with the same amplitude and phase. However, when feeding antenna is placed close to the TMRA, elements have different path loss. In another word, the signals from the feed antenna arrive at each element with different amplitudes and phases. Different amplitude and phases provide a weight matrix as a new parameter in the closed-feed TMRA. The proposed parabolic TMRA aims to provide a solution to the closed-feed TMRA. This chapter gives an explanation of parabolic TMRA along with a full wave simulation followed by the performance of the parabolic TMRA when conducting beam steering and beamforming.

Chapter 7 discusses efficiency of the TMRA and introduces the double-layer TMRA. Conventional TMRA, which consists of single layer reconfigurable elements, suffers energy loss due to the wasted energy when scattering element is OFF (non-scattering). This results in a low power efficiency. The proposed double-layer TMRA aims to increase the overall system performance by adding a second layer of elements which scatter when first layer elements are OFF. The double-layer TMRA is explained using a simple theoretical model. A realistic bowtie dipole two-layer TMRA is then analysed in a

full wave simulation. The performance of a double-layer TMRA conducting a beam steering function is carried out to compare with that of a single layer TMRA.

Chapter 8 contains conclusion and discussion. Section **8.1** summarises time modulated reflector arrays. The characteristics of time modulated reflector arrays are outlined. The novelty and contributions are discussed. The future works are also noted in the last part of Chapter 8.

1.3 Engineering functions and potential applications

Time modulated reflector arrays can provide functions such as sidelobe control, beam steering and adaptive beamforming. Combining the benefits of conventional TMA systems and reflectarrays, TMRAs have advantages over conventional phased array without the need of expensive phase shifters and lossy transmission lines. The use of switches instead of phase shifters can lower the cost in hardware. The absence of lossy transmission lines make TMRAs suitable for applications over millimetre-wavelength frequency band.

TMRAs could be used in applications such electronic scanning, object tracking, direction finding, direction dependent communications, satellite communications, radio telescoping. They are suitable for mm-wavelength applications as well. The absence of phase shift units reduces the overall size of the system which might be useful in portable applications.

Chapter 2 LITERATURE REVIEW

2.1 Introduction

This part of the thesis reviews the basic background knowledge of time modulated reflector arrays.

Section 2.2 introduces the concept of reconfigurable antennas. It reviews and summarizes various approaches to reconfigure antenna systems. It aims to find the best option to control the scattering elements of TMRAs.

Section 2.3 reviews array systems including phased array systems and reflectarrays. TMRAs borrows many techniques used in phased array and reflectarrays. The paragraph aims to provide a brief knowledge of phased arrays and reflectarrays which help readers to understand TMRAs in the later chapters.

2.2 Reconfigurable antennas

Reconfigurable antennas are hardware radiators which can operate in two or more states, and reconfigurable devices allow a single antenna for different system purposes. The performance of an antenna (e.g. gain, radiation pattern, polarization, operating frequency, bandwidth etc.) is sensitive to its configuration (e.g. shape, size, substrate and position of feed etc.). By altering the current on the antenna, using movable parts, phase shifters, diodes, tuneable material, attenuators, or any other form of active materials, the antenna can be reconfigured to meet the new specifications. For example, a reconfigurable microstrip patch antenna [**14**] can be tuned between 5 GHz and 7 GHz.

We can categorize reconfigurable antennas according to the method used to configure the antennas,

- Mechanical: moving parts, rotating radar, flexible wires, etc.
- Electrical: RF switches, varactors, ferro-eletric devices, liquid crystals, etc.

The following content reviews examples of reconfigurable antennas.

2.2.1 Mechanical reconfigurable antennas

Initially, the idea of 'reconfigurability' was achieved by mechanically moving or changing the shape of the antennas. In 1931, E. Bruce and A. C. Beck [**15**] designed a stretchable rhombic antenna to tune the operating frequency band. Using a stretchable wire to change the length of parallel wires, a rhombic antenna can be tuned to a specific frequency band. Another excellent example of mechanical reconfigurable antennas is the Arecibo Observatory in Puerto Rico [**16**] shown in **Fig.2.1**. The mechanically rotating long range radar [**17**] is also a classic example of a mechanic reconfigurable antenna. The radar consists of a very large reflector antenna and a rotating platform. The radar system

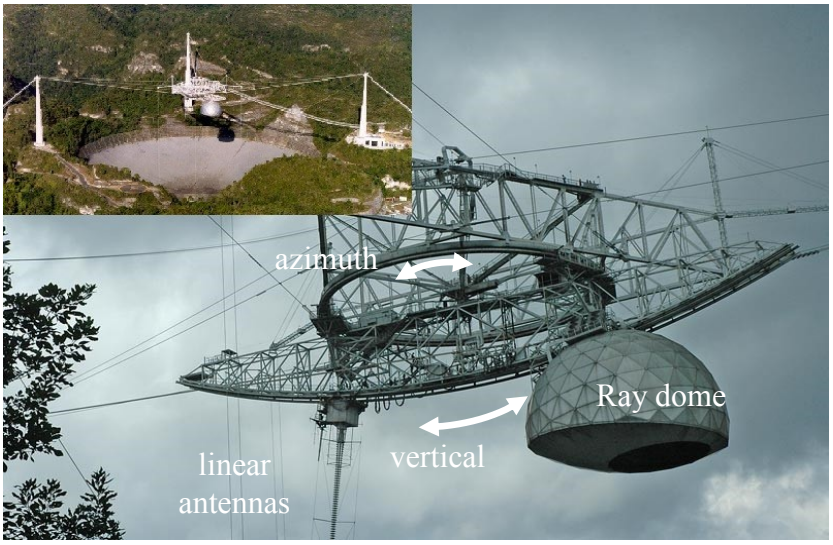

Fig.2.1 A picture of the Arecibo Observatory (up left) and the movable central feeding platform (photo from [**16**] Photo by J. Condon)

rotates the narrow antenna beam 360° to scan the free space, identifying and tracking objects.

The advantage of a mechanical reconfigurable antenna is that the design is straight forward. It provides great additional functionality for early age antennas. However, it is limited as the implementation of movable parts requires precision engineering and additional cost.

2.2.2 Electrical reconfigurable antennas

Nowadays electrical and electronic devices are more common methods to reconfigure antennas. These devices can be in the form of a discrete components such as PIN diode switches, FET switches, MEMS switches, varactor diodes and ferro-electric devices. Other techniques to reconfigure antenna systems are tuneable electromagnetic materials such as ferro-electric films and liquid crystals. Phase shifters which control the phases of the antenna feeding signals are popular devices in antenna array systems.

RF switches

RF switches (PIN diode switch, FET switches, MEMS switches) operate to manage the current flow of the antenna and guide the current in a desirable path. By controlling the voltage or current applied, the RF switches can be tuned to operate in various bias states. Two typical bias states are ON and OFF. In the 'ON' state, the impedance of switches is low and the electrons can flow between the switches' terminals. The switches operate as a closed circuit. Whereas in the 'OFF' state, the impedance of switches is high and no current flows between the switches terminals. The switches operate as an open circuit. Changing of the current path changes the radiation properties of the antenna and also the characteristic impedance. The choice of a RF switch depends on several parameters [**18**],

- Characteristic impedances when the switch is ON (forward biased) and OFF (zero-biased or reverse biased)
- Bandwidth and central frequency
- Switching speed: on/off switch times
- Robust or life time: number of switching until faulty
- Power handling

A typical mechanical RF switch is the micro-electromechanical system (MEMS) switch. Shown in **Fig.2.2**, MEMS switches are tiny devices made on a substrate. Two types of MEMS switches are presented in different clamp configurations: a fixed-fixed beam and a cantilever arm. By controlling the bias voltage of the MEMS switches, they can be configured to switch between ON and OFF states as shown in **Fig.2.2**. When the anchors are loaded with voltage, the beam will be attracted by the electrode due to the electrostatic force between the beam and the electrode. On the contrary, when the loaded voltage is removed, the electrostatic force disappears and beam returns to its original position. MEMS switches can be used as switches if they were placed between two contacts. The two contacts are connected when beam is attached to the electrode and disconnected when beam if in its original position. MEMS are known for their 'low power consumption, low insertion loss and high isolation, linearity, power handling and Q factor' but they need a package to protect their fragile beams [**19**].

MEMS switches have become popular in reconfigurable antennas. They have been used in frequency selective surfaces (FSS) [**20**] [**21**], antennas [22-24][**22**][**23**][**24**], antenna arrays [**25**] [**26**] and reflectarrays [**27**] [**28**]. Anagnostou et al. [**22**] applied RF MEMS switches to a fractal antenna which is tunable between 0.1 GHz and 6 GHz. Besides the antenna operating frequency. RF MEMS switches are used to change antenna polarizations. As shown in **Fig.2.3**, by applying MEMS switches in the feeding network, reconfigurable antennas can also switch between linear polarization, dual polarization and

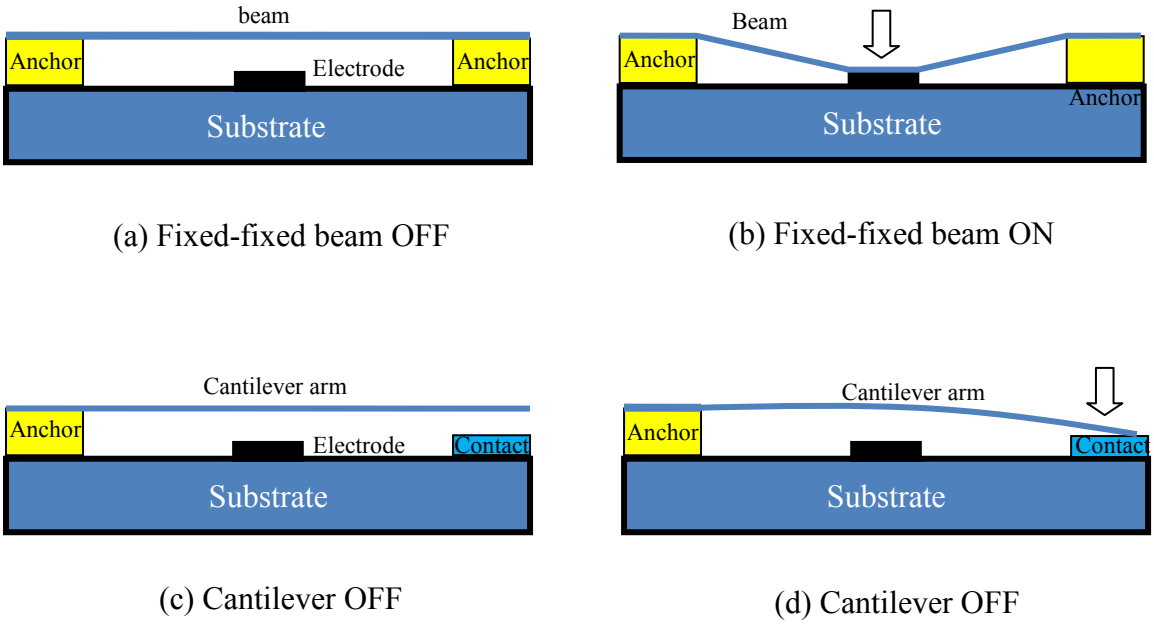

Fig.2.2 MEMS switches in their OFF and ON positions

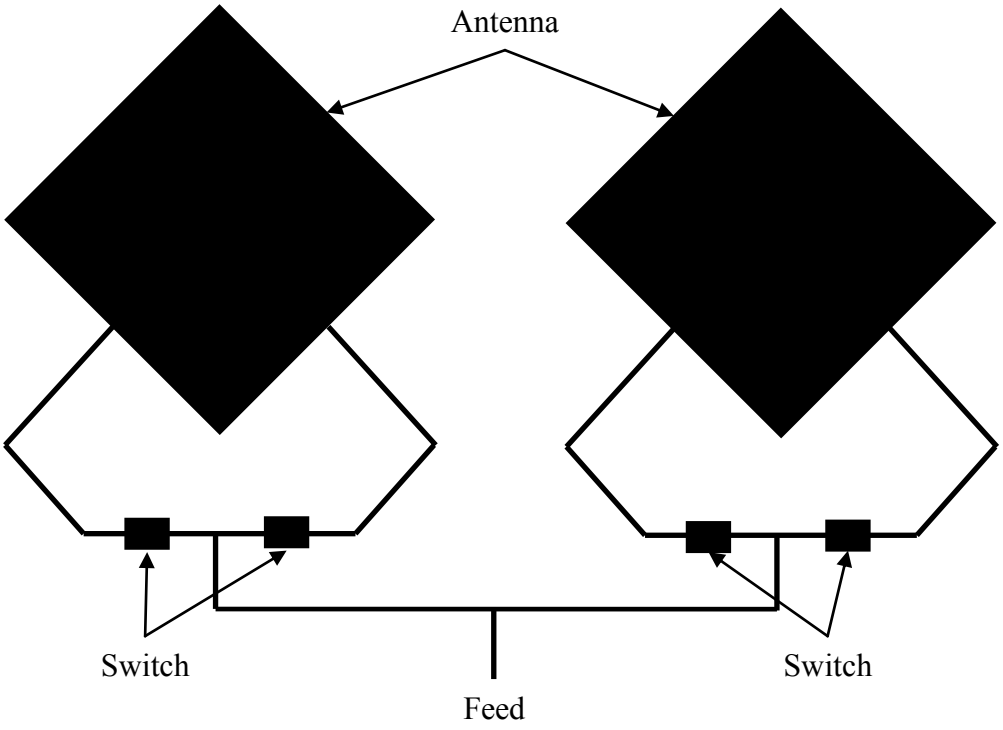

Fig.2.3 A two-element reconfigurable antenna array controlled by MEMS switches with linear, dual and circular polarizations [**24**]

circular polarization [**24**].

The field-effect transistor (FET) switch is a semiconductor RF switch. As **Fig.2.4** shows**,** a FET switch has four terminals, the *source*, the *drain*, the *gate* and the *substrate*. The carrier or RF signal enters at the *source* and leaves the channel at the *drain*. The *gate* modulates the channel conductivity. The *substrate* terminal is designed to bias the FET into operation. The shape of the channel beneath the gate depends on the voltage at the gate. FET changes the conductivity of the channel by controlling the channel shape using variable voltage. Hence, by controlling the voltage applied to the gate, the current flow (the channel) between the source and the drain can be controlled. Compared to RF MEMS switches, the cost of FET switches is lower and the hardware implementation is simpler. However, FETs have poor power handling due to the fragile insulating layer between the gate and the channel, which makes them vulnerable to electrostatic damage [29].

An example of a FET-controlled antenna can be found in a reconfigurable ultra-wide band (UWB) monopole antenna designed for cognitive radio [**29**]. The monopole

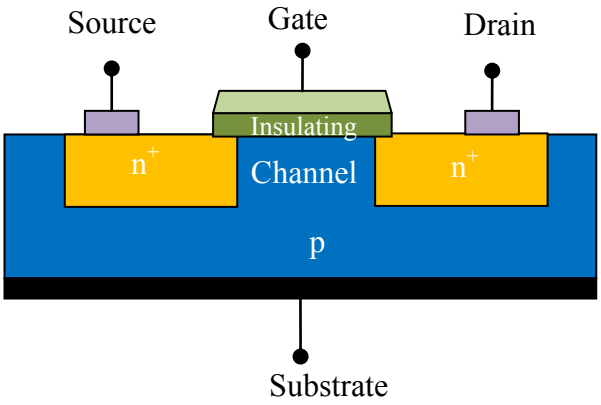

Fig.2.4 A diagram of a MOS field-effect transistor (FET). By controlling the voltage at the gate, the current flow between the source and drain can be managed.

antenna consists of a group of stubs connected by FET switches. The switches can change the length of the monopole in order to change the operating frequency band: UWB, multi-band.

Moreover, it is interesting to see a reconfigurable aperture (RECAP) antenna [**30**]. As **Fig.2.5** shows, the elements of the RECAP antenna were connected by FET based switches. By controlling the switches, the current flow of the aperture can be altered. The results in [**30**] suggest the RECAP antenna can change the bandwidth of operation and steer the pattern of the antenna.

The PIN diode is another type of semiconductor RF switch. As shown in **Fig.2.6,** a PIN diode consists of heavily doped p-type and n-type regions which are separated by a wide intrinsic region. In contrast to the FET switches, PIN diodes are controlled by current, and have good power handling up to several amps of RF current [**31**].

When the PIN diode is not biased or reversed biased, there is little charge in the

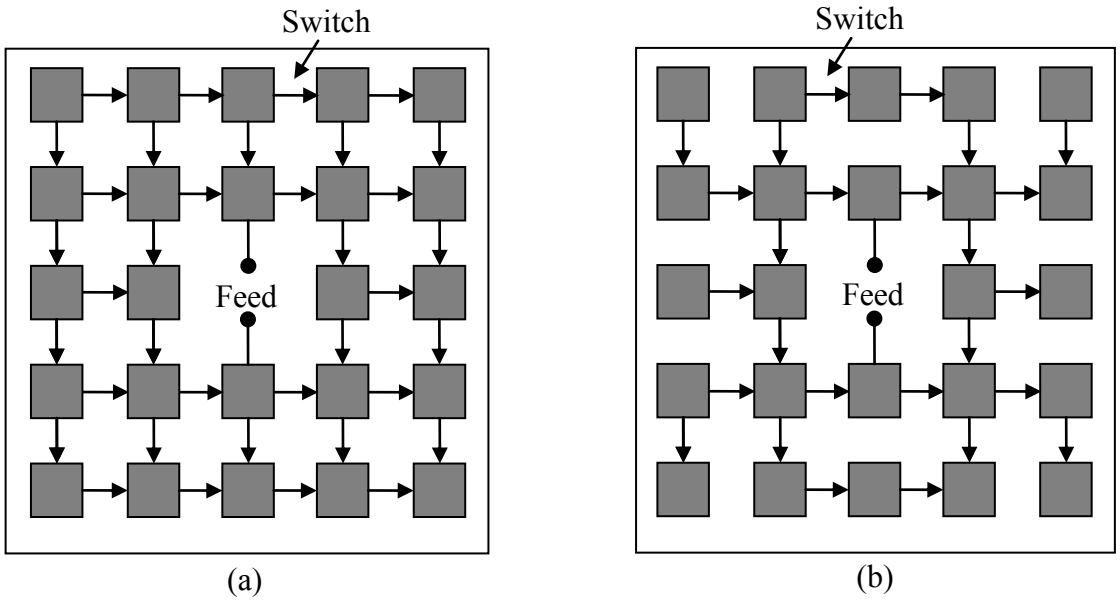

Fig.2.5 Shematic drawing of a reconfigurable aperture antenna: (a) all switches ON, (b) part of the switches are off to route the current [**30**]

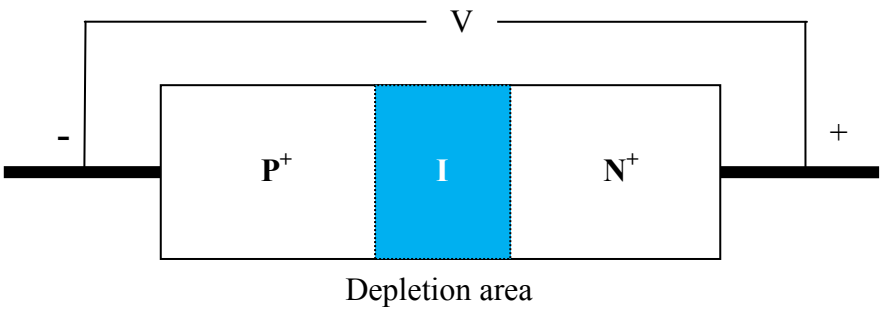

Fig.2.6 Model of a PIN diode. The diodes consists of P-node and N-node separated by the intrinsic region.

intrinsic region which means it forms a very large depletion area. Under such circumstances, the PIN diode has a very high impedance. When the PIN diode is forward biased, the injected carrier concentration is much higher than that of the intrinsic region. Thus the electrons and holes will flood into the intrinsic region. Once the level of electrons and holes in the intrinsic region reaches a balanced point where the numbers of electrons and holes are equal, the depletion area in the I region becomes very narrow. The electric field extends into the depletion area which helps the transportation of charges between the N and P regions. The fully forward biased PIN diode has a very low impedance.

Applying the PIN diode to a reconfigurable device, S. Nikolaou et. al. [**32**] developed an annular slot reconfigurable antenna. This antenna can change its operating frequency and its radiation patterns. Jong-Hyuk Lim *et. al.* [**33**] designed planar inverted-F antenna controlled by PIN diodes and a varactor for mobile devices. The antenna can be tuned between US-PCS, WCDMA, WiMax and WLAN bands.

P.D. Grant et. al. have compared the performance data of RF MEMS and semiconductor switches [**34**]. They claimed that FET switches, PIN diodes and MEMS switches are all suitable for wireless communications. However, due to the benefits of high isolation and low power consumption of MEMS switches, MEMS technology can

bring improved performance especially for hand held devices. However, it is must be noted that FET switches and PIN diodes do not require complex package and bias network. Also finally semiconductor components are not only mature products which are widely available in today's market, but also they do not need an advanced fabrication facilities.

Varactors diodes

Varactors, also called variable capacitance diodes or tuning diodes, are used in reconfigurable antennas for tuning the antenna's frequency range. Similar to PIN diodes, varactors have a depletion layer as the insulating dielectric. However, the thickness of the depletion layer varies with the applied reverse bias voltage. So the capacitance of the varactor can be tuned. The capacitance is inversely proportional to the applied reverse

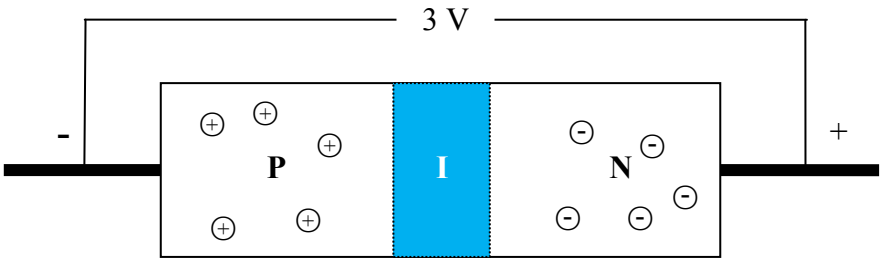

Depletion area

a. Low voltage, thin depletion area, high capacitance

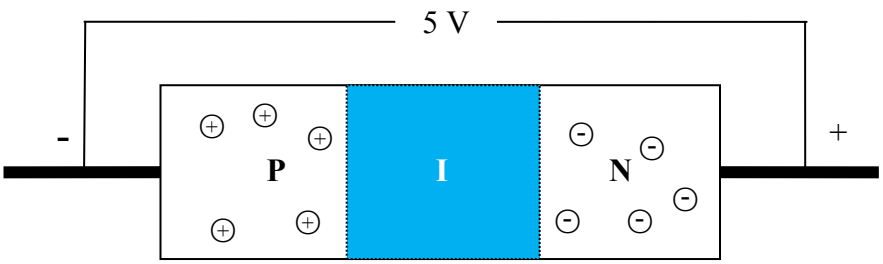

Depletion area

b. High voltage, thick depletion area, low capacitance

Fig.2.7 Models of a varactor with variable capacitances

bias voltage. In **Fig.2.7**, when reverse bias voltage is low, the depletion area is narrow. Thus the capacitance is high. On the contrary, when being applied with high reverse bias voltage, the varactor has a low capacitance. For instance, a SANYO SVC704 varactor [**35**] has an inter-terminal capacitance of 30 pF applied 1V and 4 pF applied 7 Volt at 1 MHz .

Varactors are popular in applications for tuning antenna operating frequency. Apart from the Jong-Hyuk Lim's tuneable PIFA antenna for mobile phone applications [**33**], the varactors are used to tune a dual band slot antenna [**36**], a tuneable reflectarrays [**37**], a Quasi-Yagi folded dipole antenna [**38**] etc. Varactors are also applied to configure the antenna radiation patterns [**39**].

Ferro-electric material

Ferro-electric material is a tunable material which can be tuned by applying an external bias electric field. The permittivity of the ferro-electric material can be changed using a d.c. electric field. The idea of ferro-electricity is not new and was discovered by Valasek in his experiment with Rochelle salt [**40**]. However, their applications in the microwave industry has been limited due to their high dielectric losses. In the last two decades, scientists have addressed the high loss issue by developing some thin ferro-electric films with low dielectric loss tangents and good tunabilities **[41-43]**[**41**][**42**][**43**]. The improved ferro-electric films are very good substrate for tuneable antennas.

Y. Yashchyshyn and J. W. Modelski have investigated electronically-scanning antennas using ferroelectric substrate [**44**]. The electrical scanning property was based on the idea of leaky-wave antennas. The substrate was made using a polymer containing the ferro-electric powder $Ba_{0,65}Sr_{0,35}TiO_3$. The permittivity of the polymer can be changed by the electric field applied. Numerical analysis has showed that the beam direction can change by over 30 degrees if the d.c. biased field is applied at 200V.

Romanofsky R. R. designed and manufactured scanning reflectarray antennas based on ferro-electric film phase shifters [**45**]. The reflectarray antennas consists of a feed antenna and a grid of flat reflector elements which is controlled by ferro-electric phased shifters. The phase shifters took the form of the ferro-electric material $Ba_{0,65}Sr_{0,35}TiO_3$ laser-ablated on the $LaAlO_3$ substrate. The results of [**45**] showed the reflectarray antennas based on ferro-electric phase shifters can provide an efficient low cost scanning solution above X-band frequencies.

The first advantage of ferro-electric films is elasticity. The material is normally in the form of a polymer which can be in any dimension. They are suitable candidates in large reconfigurable antenna applications such as reconfigurable reflectarray antennas. The recent development of ferro-electric films brings attractive features such as low loss, analog controlling, etc. More devices based on the ferro-electric materials will be reported in the future.

Other techniques

Other known techniques includes photo-conductive material, liquid crystals and graphene. Photo-conductive materials becomes electrically conductive due to the absorption of electromagnetic radiation such as visible light, ultraviolet light, infrared light, or gamma radiation. In [**46**] a visible light has been used to create photoinduced plasma inside the nsemiconductor substrate of a reflectarray. However, photo-conductive materials have a significant loss as their dielectric loss tangents are high.

Liquid crystal (LC) has been shown to modulate the phase of signals in the microwave and mm wave bands by applying electric field. In last two decades, several examples based on tunable liquid crystal have been proposed in publications. These examples include an LC-based reconfigurable reflectarray, which operates in the frequency range from 96 to 104 GHz [**47**], a multi-resonant unit cells for reflectarray

which operates at X band [**48**] and a 77 GHz microstrip reflectarray with beam reconfiguration capability [**49**].

Graphene is a meta-material with extraordinary properties [**50**]. The material strength of graphene is about 100 times higher than steel by weight. It is nearly transparent and have great conductivity of heat and electricity. Recently, the use of graphene becomes an option in reconfigurable devices. A graphene-based reflectarray for beam-scanning at 1.3 THz has been proposed in [**51**]. [**52**] applied a single layer graphene onto a tunable frequency selective surface (FSS) for terahertz (THz) applications. The use of graphene is still on its early age. More graphene based reconfigurable devices are expected in the future.

2.2.3 Summary

There are many available technologies for controlling the electromagnetic waves in antenna systems. However, they are different in terms of maturity, performance, integration complexity, frequency band. To select the best option for their design, engineers need to choose the reconfigurable components based on their needs. Semiconductor switches such as FET switches, PIN diodes and varactor diodes are commonly used in reconfigurable antenna designs for their reliability and availability. They are still a good choice in antenna designs. RF MEMS switches have become a popular choice due to their low loss up to mm-wave frequencies [**28**] [**53**]. Ferro-electric films are a low loss and elastic material which provide freedom in antenna dimensions. Ferro-electric films are analog controlled but can be digital if they are created as a hybrid with semiconductor switches [**45**]. Photo-conductive material, graphene and liquid crystals have been used in reconfigurable antennas of mm-wavelength frequency range.

Initially, the concept of reconfigurability allows a single antenna to perform multiple functions. In the future, with the development of semiconductors and the meta-

materials, antennas may advance in order to exploring new missions. Combined with the technology discovered in digital signal processing and artificial intelligence, future antennas may be able to reconfigure themselves based on objectives. Time modulated reflector arrays are actually based on this idea of giving similar functionalities as compared to the conventional phased array.

2.3 Antenna arrays, phased arrays and reflectarrays

An antenna is defined as a device to transmit or receive electromagnetic radio waves [**54**]. An antenna can operate on its own. However, there are benefits of assembling two or more antennas to achieve functions such as electronically scanning and beamforming. The overall radiation field of the array is a vector sum of the radiation fields of the individual elements. There are a lot of parameters in determining an antenna array's overall radiation patterns. Apart from the characteristics of the individual elements (radiation pattern, power, polarization, etc), other factors brought by the antenna array are [**55**]:

- "the geometrical configuration of the overall array (linear, circular, rectangular, spherical, etc.) ";
- "the relative displacement between elements";
- "the relative phase differences between elements";

2.3.1 Numerical analysis of antenna array

Assume an array of two isotropic radiators is placed along the x-axis, as shown in **Fig.2.8**. The individual elements are identical to each other in excitation magnitudes and phases. The radiation fields of the two single dipole antennas can be described as

$$E_0 = \frac{\boldsymbol{E}(\theta_0)e^{-jkr_0}}{r_0}$$
$$E_1 = \frac{\boldsymbol{E}(\theta_1)e^{-jkr_1}}{r_1} \qquad \textbf{Eq.2.1}$$

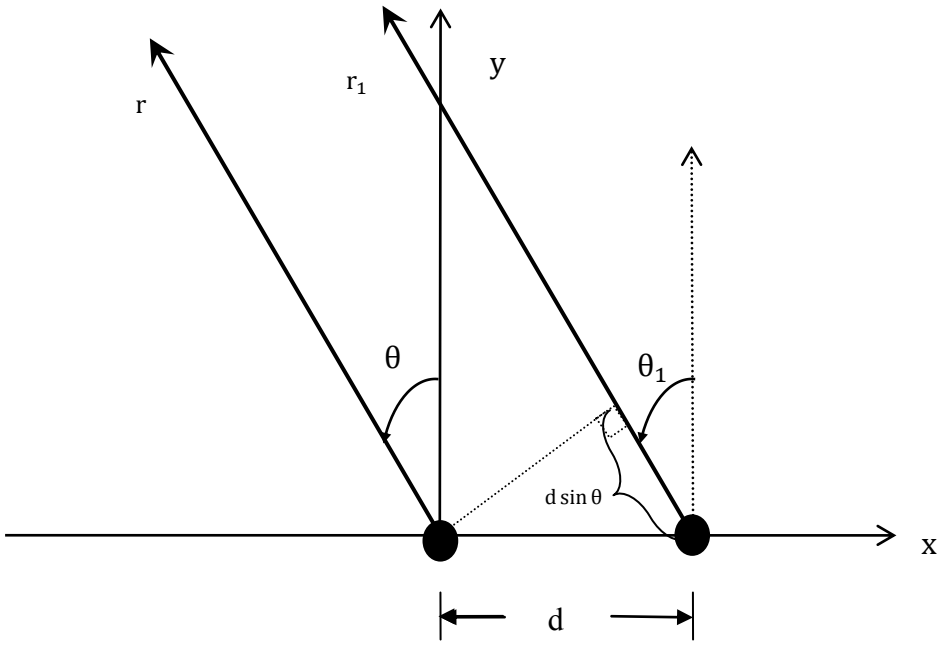

Fig.2.8 Farfield observation of a 2-element antenna array

where r_0, r_1 are the distances from the dipoles to the point where the fields are evaluated. θ_0 and θ_1 are the observation angles. k is the wavenumber. $E(\theta)$ is the radiation pattern of the single element. Observed from a long distance as in **Fig.2.8**, approximations for amplitude and phase variations are

$$\begin{aligned} &\theta_0 \cong \theta_1 \\ \text{Phase variations} \quad &r_1 \cong r_0 + d\sin\theta \\ \text{Amplitude variations} \quad &r_0 \cong r_1 \end{aligned} \qquad \textbf{Eq.2.2}$$

where d is the inter-element distance. If the coupling between elements is not considered, the total farfield radiation of the array is equal to the sum of the two antennas, which is given as [**55**]

$$\begin{aligned} E_0 + E_1 &= \frac{E(\theta_0)e^{-jkr}}{r_0} + \frac{E(\theta_1)e^{-jkr_1}}{r_1} \\ &= E(\theta_0)\left(\frac{e^{-jkr_0}}{r_0} + \frac{e^{-jkr_1}}{r_1}\right) \\ &= \frac{E(\theta_0)}{r_0}\left(e^{-jkr_0} + e^{-jk(r_0 + d\sin\theta)}\right) \end{aligned} \qquad \textbf{Eq.2.3}$$

$$= \frac{E(\theta_0)}{r_0} e^{-jkr_0}(1 + e^{-jkd\sin\theta})$$
$$= \frac{E(\theta_0)e^{-jkr_0}}{r_0} * AF$$

Hence the total radiation field is equal to the field of a single element multiplied by the array factor (AF). The array factor for this 2 element array is then given as

$$AF_2 = 1 + e^{-jkd\sin\theta} \qquad \textbf{Eq.2.4}$$

For an *N*-element linear array, assume the elements are identical and the inter-element distance is *d*. A general form of array radiation can be written as

$$\begin{aligned} E_{total} &= E(\theta_0)\frac{e^{-jkr_0}}{r_0} + E(\theta_1)\frac{e^{-jkr_1}}{r_1} + \cdots + E(\theta_n)\frac{e^{-jkr_n}}{r_n} \\ &= E(\theta_0)\left(\frac{e^{-jkr_0}}{r_0} + \frac{e^{-jkr_1}}{r_1} + \cdots + \frac{e^{-jkr_n}}{r_n}\right) \\ &= \frac{E(\theta_0)e^{-jkr_0}}{r_0} * \left(e^{-jkr_0} + e^{-jk(r_1 + d\sin\theta)} + \cdots + e^{-jk(r+(n-1)d\sin\theta)}\right) \\ &= \frac{E(\theta_0)e^{-jkr_0}}{r_0} * \sum_{n=1}^{N} e^{-j(n-1)(kd\sin\theta)} \\ &= \frac{E(\theta_0)e^{-jkr_0}}{r_0} * AF \end{aligned} \qquad \textbf{Eq.2.5}$$

where *n* is an integer. The array factor for the N-element linear array is

$$AF_N = \sum_{n=1}^{N} e^{-j(n-1)(kd\sin\theta)} \qquad \textbf{Eq.2.6}$$

2.3.2 Phased array and beamforming

A phased array is an array of antennas of which relative phases of signals generated by individual elements are adjusted to enhance the radiation in desired directions and to reduce the radiation in undesired directions [**56**]. It was first introduced in 1905 by Karl Ferdinand Braun as part of his research into enhanced radio transmission systems [**57**]. For over a hundred years, phased arrays attracted researchers' interests as well as industrial enterprises' investments. Now the concept is used in modern radar

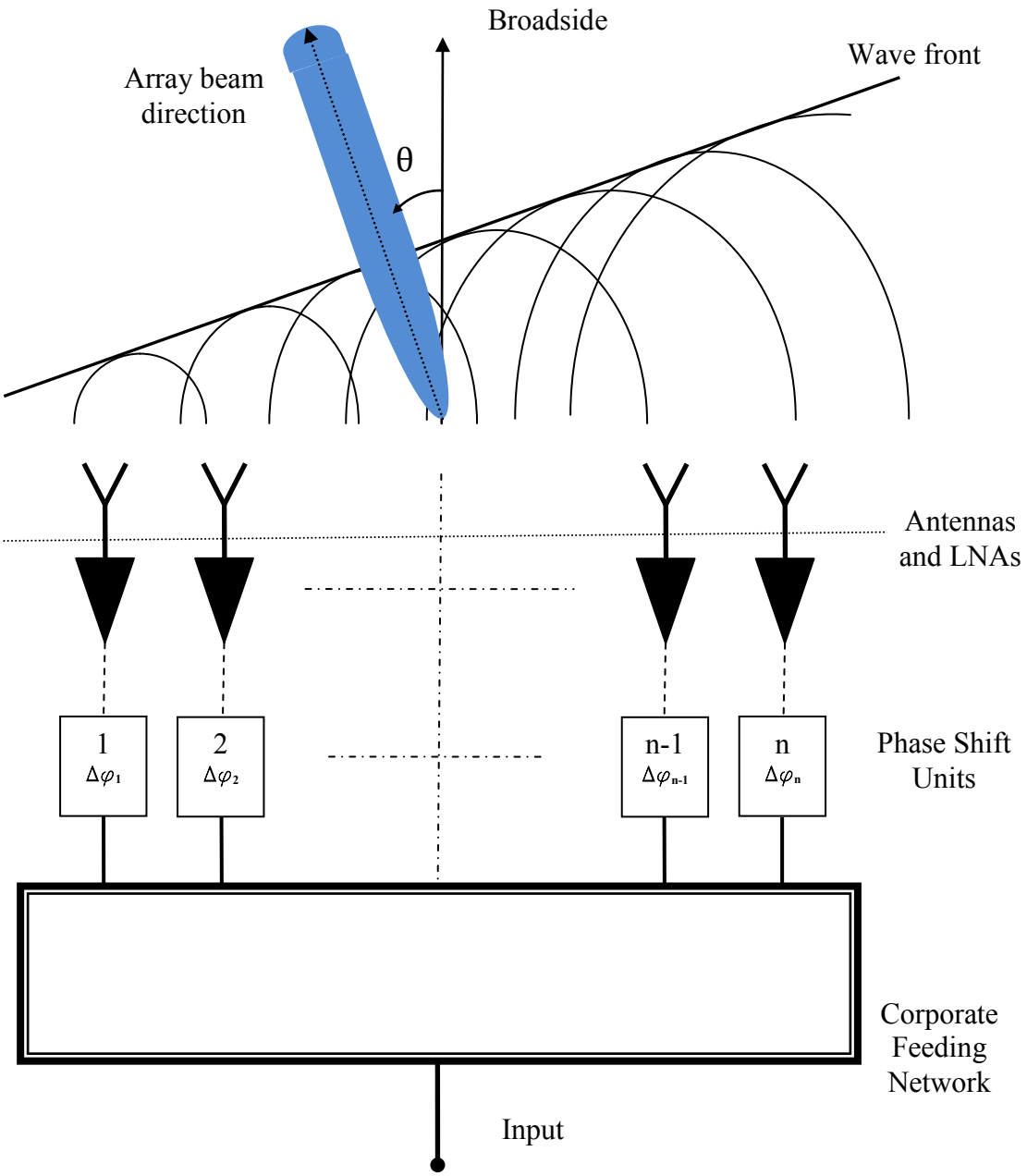

Fig.2.9 Model of a corporate fed linear phased array system in transmitting mode.

system [**56**], television broadcasting [**58**], space-probing [**59**], weather forecasting [**60**] and mobile communications [**61**]. The phased array system consists of a grid of individual antennas connected to phase shift units. It can be used in both transmitting and receiving modes. Phase shift units can apply relative phase variances to the signals transmitted to or received from antennas. By controlling the phase variances, generate

directive beams can be generated in the desired directions and the radiation magnitudes can be reduced in un-desired directions.

Fig.2.9 shows the simple model of the linear phased array operating at the transmitting mode. It consists of a corporate feeding network, phase shift unites, low noise amplifiers (LNAs) and antennas. The objective of the system is to generate a directive beam at an angle of θ from broadside of the array. The input of the system is normally a continuous wave (CW) generated by an oscillating source. The CW is then transmitted through the feeding network and arrives at each phase shift unit with an identical peak-power magnitude and phase. The core process of the phase array is to apply the phase variances $\Delta\varphi_n$ to the CW using phase shift units. The processed waves are then amplified by the LNAs before being emitting to free space by the array antennas.

The beam direction is steered by adding a phase taper to the array elements. The phase taper is actually a phase weight applied by the phase shifters. If define the weight as a *weight vector* $\mathbf{W} = \left[e^{j\Delta\varphi_1}\ e^{j\Delta\varphi_2}\ \cdots\ e^{j\Delta\varphi_n} \right]$, **Eq.2.5** can be written as

$$AF = \sum_{n=1}^{N} e^{-j(n-1)\left(kd\ sin\,\theta + \Delta\varphi_n\right)} \qquad \textbf{Eq.2.7}$$

For example, in a two-element array with half-wavelength element spacing, a phase of $\Delta\varphi_1 = 0^o$ and $\Delta\varphi_2 = 40^o$ could be applied to the two elements. Assume the two radiators have an identical isotropic radiation pattern. Then the beam is steered to 20^o as shown in **Fig.2.10**.

In the receiving mode (**Fig.2.11**), the phased array is able to monitor several transmitters at the same time. The receiving phased array consists of an array of antennas and several groups of vector modulators. All the signals are received by the antenna arrays and transmitted to each group of vector modulators. The received signals of each

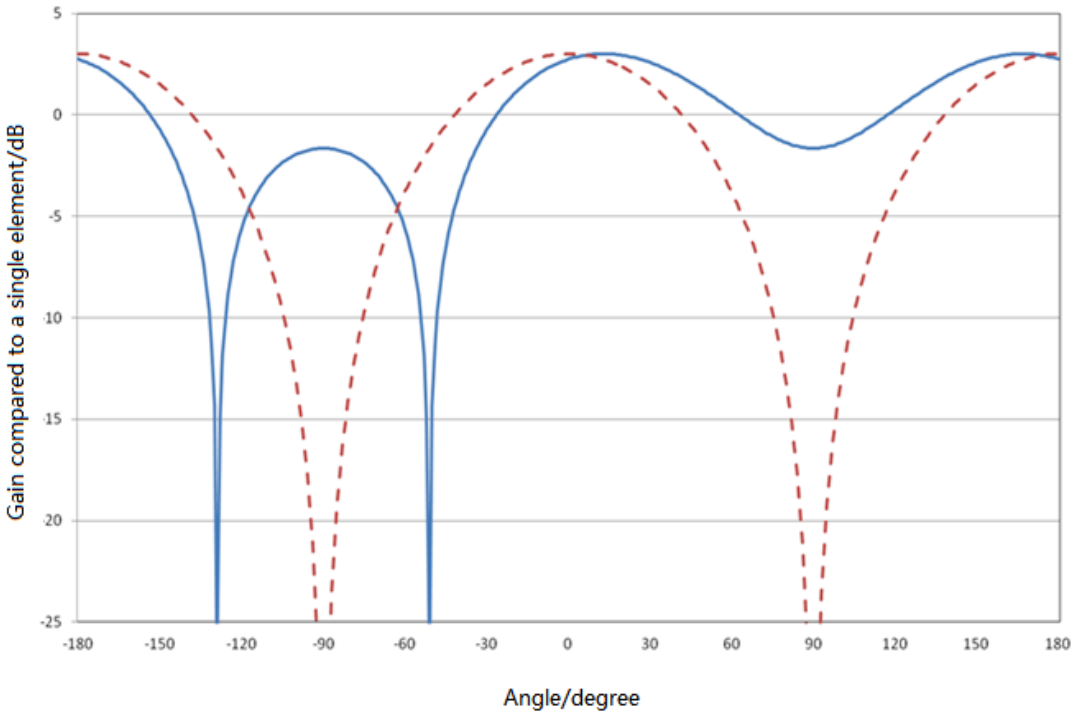

Fig.2.10 Radiation patterns of two element linear phased array: solid line is steered to 20°, dashed line is non phase-tapered reference.

transmitter can be expressed as an array factor where each signal corresponds to a relevant signal vector $\mathbf{S_k}$ which is usually called the *steering vector*. *k* is the wavenumber of the transmitter. This method is a common way to calculate a *weight vector* **W** to steer the main beam direction [**55**],

$$\boldsymbol{W} = \frac{1}{N}\boldsymbol{S_k} \qquad \textbf{Eq.2.8}$$

where N is the number of elements. By putting $\frac{1}{\mathrm{N}}$ before the steering vector, the weight vector can be normalized to form a unity response in the desired direction. For M transmitters, M associated steering vectors can be determined. If there are enough vector modulator groups and associated DSP devices as shown in **Fig.2.11**, a phased array system can track multiple moving targets or operate multi-channel communications.

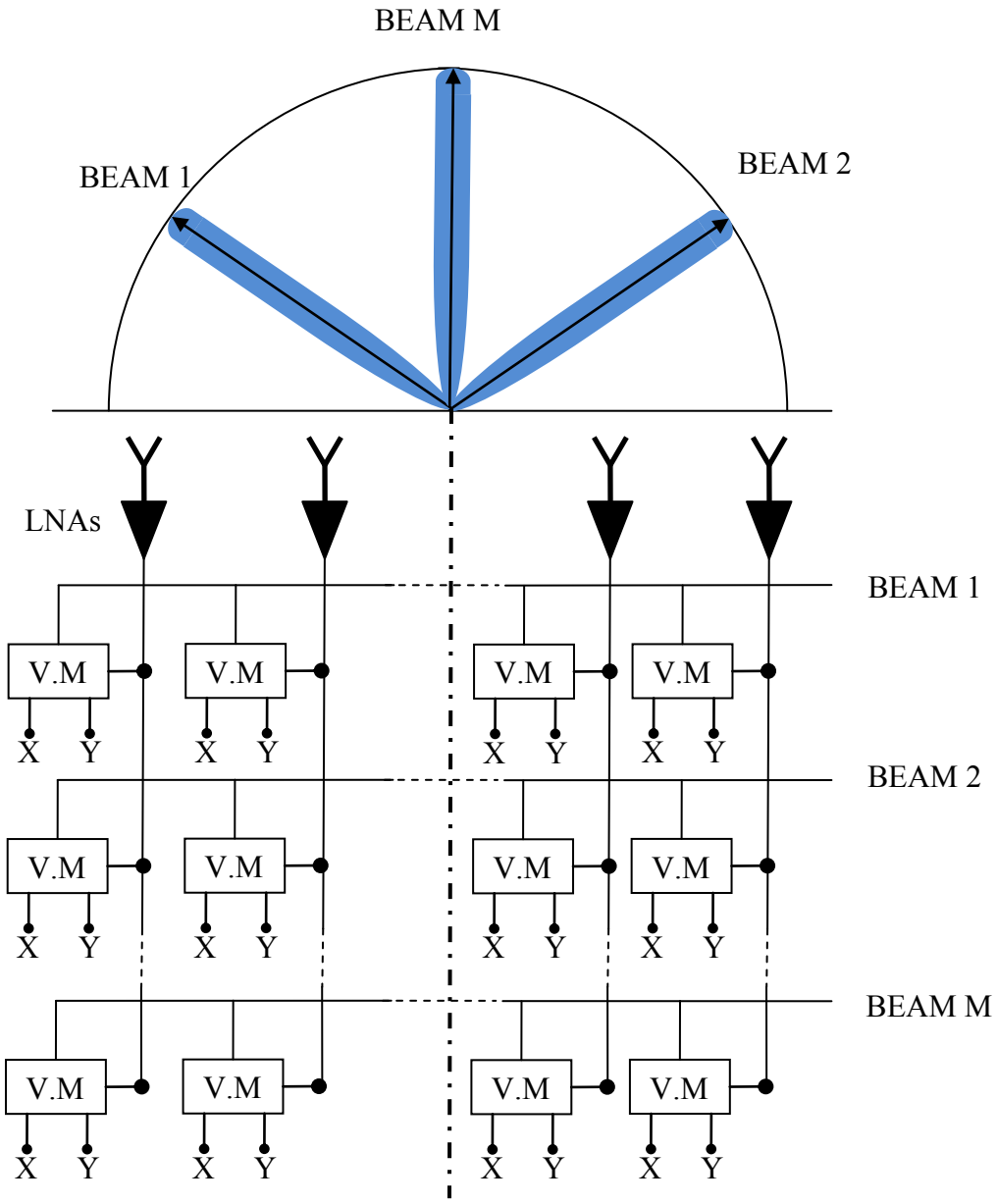

Fig.2.11 A linear phased array system operating at the receiving model. System consists of antennas, low noise amplifiers and vector modulator

For example, assume a four-element linear phased array is expecting a signal from a transmitter at an angle of 30 degree of array broadside. Assuming the array elements have an identical isotropic radiation pattern and are spaced apart by $d = \lambda/2$, the steering factor of the transmitter is calculated by **Eq.4.6**,

$$\boldsymbol{S_0} = [e^0\ e^{j\pi sin(30^o)}\ e^{j2\pi sin(30^o)}\ e^{j3\pi sin(30^o)}\ ]$$
$$\boldsymbol{S_0} = [1\ \ e^{\frac{j\pi}{2}}\ e^{j\pi}\ e^{\frac{j3\pi}{2}}\ ] \qquad \textbf{Eq.2.9}$$

Hence, the weight vector for this transmitter is

$$\boldsymbol{W_0} = 0.25\ [1\ \ e^{\frac{j\pi}{2}}\ e^{j\pi}\ e^{\frac{j3\pi}{2}}\ ] \qquad \textbf{Eq.2.10}$$

If there are two additional transmitters located at -20^o (-0.436 in radians) and 70^o (1.222 in radians) respectively. The calculated weight vectors for -20^o and 70^o transmitters are

$$\boldsymbol{W_1} = 0.25\ [1\ \ e^{-0.342j\pi}\ e^{-0.684j\pi}\ e^{-1.03j\pi}\ ]$$
$$\boldsymbol{W_2} = 0.25\ [1\ \ e^{0.94j\pi}\ e^{1.88j\pi}\ e^{2.82j\pi}\ ] \qquad \textbf{Eq.2.11}$$

By applying the weight vectors using vector modulators, the phased array can receive the three signals from the transmitters individually and simultaneously. **Fig.2.12** shows the formed pattern based on the calculated weight vectors. Also it must be noted that this is a simple way to filter the desired signals. Applying advanced signal processing algorithms, phased arrays can achieve powerful functions such as adaptive beamforming, sidelobe control and nulling. Moreover, two or more functions can be operated at the same time.

In **Fig.2.12**, the acquired beams are steered to the desired directions. However, for the beam pointed to 70^o, it has a large sidelobe in the direction of -80^o. If there were interferences or jamming signals in that direction, the system cannot identify the real transmitter. One approach to eliminate the interference is to steer a null to that direction. The weight vector must fulfil the following constraints [**62**],

$$\begin{aligned} \boldsymbol{W^H S_0} &= 1 \\ \boldsymbol{W^H S_1} &= 0 \\ &\cdots \\ \boldsymbol{W^H S_k} &= 0 \end{aligned} \qquad \textbf{Eq.2.12}$$

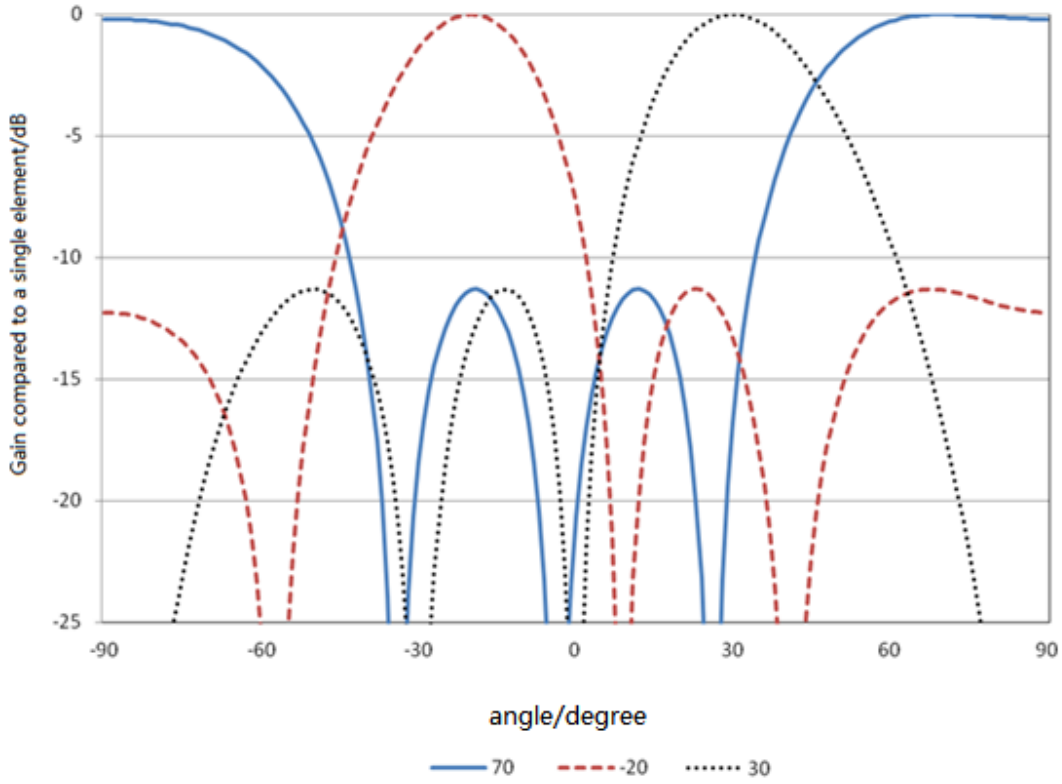

Fig.2.12 Radiation patterns of a 4 element linear phased array: the 3 beams are steered to $30^{o}, -20^{o}$ and 70^{o} respectively.

where $\boldsymbol{S_0}$ is the steer vector of the transmitter, $\mathbf{S_1} \cdots \mathbf{S_k}$ are the directions of the interferences and $\boldsymbol{W^H}$ is the conjugate transpose, i.e. Hermitian, of weight vector $\boldsymbol{W}$. **Eq.2.13** is a set of constrains to retain a fixed unit response at the direction of transmitter but nulls at the direction of interferences. Assume that the matrix $\boldsymbol{A}$ contains all the steering vectors, and the constraints matrix **C** is

$$\boldsymbol{A} = [\boldsymbol{S_0} \quad \boldsymbol{S_1} \quad \cdots \quad \boldsymbol{S_k}]$$
$$\boldsymbol{C} = [\mathbf{1} \quad \mathbf{0} \quad \cdots \quad \mathbf{0}]^{\boldsymbol{T}} \qquad \textbf{Eq.2.13}$$

The solution for the weights in **Eq.4.10** is given as [**62**],

$$\boldsymbol{W^H} = \frac{\boldsymbol{C^T A^H}}{\boldsymbol{A A^H}} \qquad \textbf{Eq.2.14}$$

For example in a 4-element linear array with half wavelength inter-element spacing, the array is expecting a transmitter at the direction of 30^{o}. Three jammers are located at

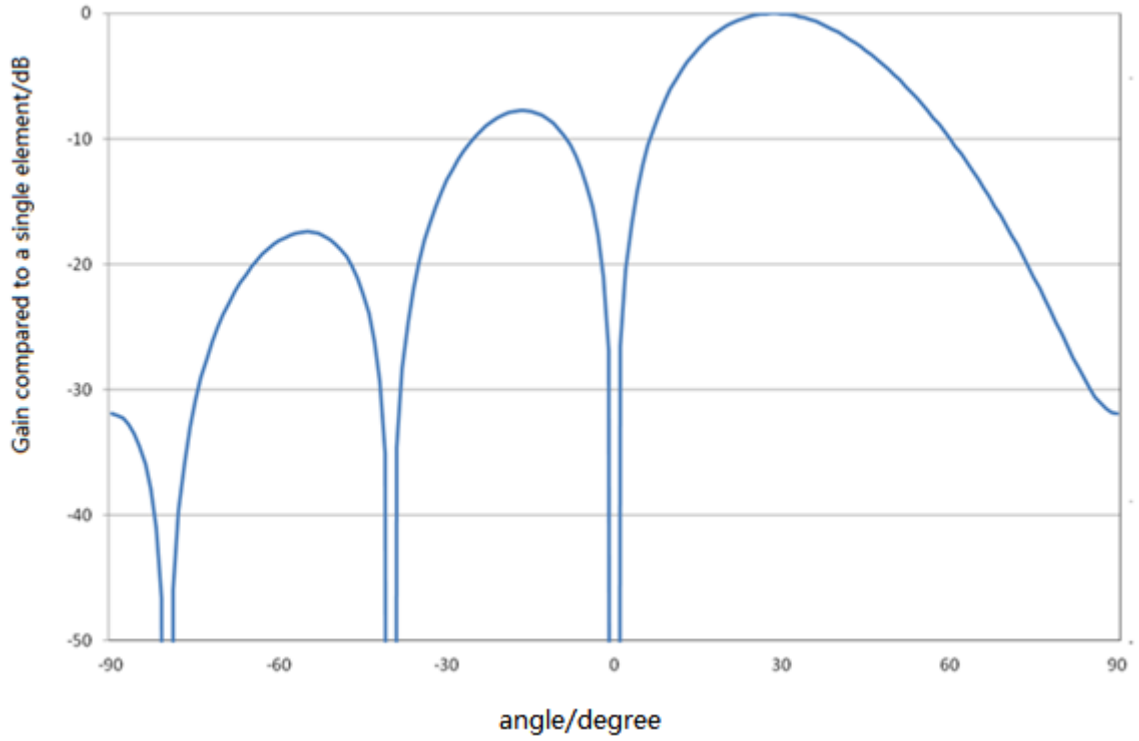

Fig.2.13 Radiation patterns of a 4 element linear phased array with half-wavelength inter-element spacing: the main beam is steered to 30^o and nulls are at $0^o, -40^o$ and 80 respectively.

$0^o, -40^o$ and 80^o respectively. The resulting radiation pattern is depicted in **Fig.2.13**. In addition, there are other ways to control radiation patterns such as the Least Mean Square (LMS) algorithm, the Direct Matrix Inversion (DMI) algorithm, the Minimum Variance Distortionless Response (MVDR) beamforming and the Linearly Constrained Minimum Variance (LCMV) beamforming. These advanced approaches carry additional functions such as sidelobe control, noise reduction, gain improving, system capacity and etc. Further detailed discussions of these algorithms can be found in [**56**] [**62**] [**63**].

2.3.3 Reflectarrays

Phased arrays provide electronic reconfiguring and scanning of the beam patterns. However, the disadvantage of phased arrays is the complex feeding network which require dedicated transceiver modules for each of the antenna elements. The feeding

network becomes lossy when the operating frequency goes higher (millimetre-wave). Reflectarrays combines the technologies of aperture antennas and antenna arrays. Recent developments of reflectarrays have realized functions such as beamforming, beam steering without the need of the complex feeding network.

Reflectarrays take the form of reflector antennas, which consists of a feeding antenna and a grid of reflecting elements. The reflecting elements can be fixed or reconfigurable. Fixed reflectarrays typically provide functions such as fixed directive beamforming. The reconfigurable reflectarrays can dynamically control the beam patterns. In **Section 2.2**, different approaches to reconfigure antennas have been reviews, which are found in reflectarrays (e.g. varactor diodes [**37**], PIN diodes [**64**], MEMES switches [**28**] [**65**], ferro-electric films [**45**], photo-conductive material [**46**], graphene [**51**] and liquid crystals [**47**]). These technologies make the reflectarrays a useful beamforming system combining the merits of reflector antennas and phased arrays. Not only have they provided simplicity and high directivity for the reflector antenna, but also offered adaptive beamforming functions of phased arrays. Furthermore, reflectarrays are highly efficient due to the absence of complex lossy feeding networks and the overall cost of the system is reduced as less transceivers are required.

Basic model of a reflectarray

The reflectarray normally takes the form of a planar antenna, which is shown in **Fig.2.14**. The centre of the reflectarray is placed at the point $(0, 0, f)$where f is the focal length. The array elements collimates waves from the feeding antenna (placed at origin (0, 0, 0)) into a sharp beam by applying phase corrections to each of the scattering elements on the reflectarray. The phase corrections must be chosen to keep the scattered field of the reflectarray constantly normal to the direction of the desired beam so that [**66**],

$$k_0(\vec{r}_{mn} - \vec{R}_{mn} \cdot \vec{r}_0) - \Delta\phi_{\mathrm{mn}} = 2\pi N \qquad \textbf{Eq.2.15}$$

where k_0 is the free space wavenumber. $\vec{r}_{mn}$ is the position vector of the *mn*-th element. $\vec{R}_{mn}$ is the position vector of the *mn*-th element relative to the centre of the reflectarray (0, 0, *f*). $\vec{r}_0$ is the direction of the desired beam and N is an integer. $\Delta\phi_{mn}$ is the phase correction between the source field and the mn-th element of the scattering field. The narrow directive beam is one of the applications of the reflectarrays. They can synthesise multi-beams, contoured-beam as well as multi-feed systems using more sophisticated designs.

The combination of reflector antennas and phased arrays show the superior benefits over conventional phased arrays in mm-wavelength applications. However, realizing the phase corrections in the reflectarray is not easy. The phase shift unit must provide a large range of phase for scattering elements. The phase variances must be as linear as possible [**66**] for a potential good operating bandwidth. In addition, the magnitude of the scattering field must not change with the changing of the phase. In fact, it is more practical to start with reflectarrays with static phase corrections.

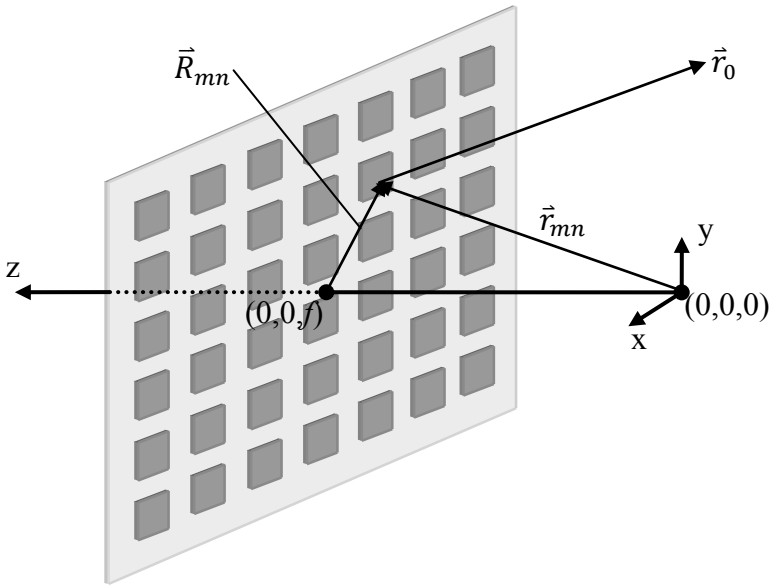

Fig.2.14 Spatially-fed reflectarray geometry

Fixed reflectarray

Many fixed reflectarrays are designed in various shapes and sizes. D.M. Pozer et al. designed a microstrip square-patch reflectarray shown in **Fig.2.15** [**67**]. They explored different feeding methods (prime focus, Cassegrain focus) and geometry (6 inch square and 9 inch square elements). The phase corrections are realized using variable patch length. The millimetre wave frequency (22 GHz and 77 GHz) microstrip reflectarrays were made to measure. The results showed the microstrip reflectarray can synthesis a high gain radiation pattern without the transmission line losses in conventional microstrip arrays. Another fixed reflectarray design is in the shape of slots. In the slot reflectarray design as shown in **Fig.2.16** [**68**], the phase corrections were obtained by adjusting the length of the slots. Both simulated and measured results suggested that the microstrip slot reflectarray can allocate the beam into a fixed direction. When compared to the variable-size patch reflectarray, the author claimed the slot reflectarray provide better performance on operating bandwidth. Besides squares and slots reflectarrays, fixed reflectarrays can be realized in patches of variable rotation angles [**69**] and loops [**70**]. A study in

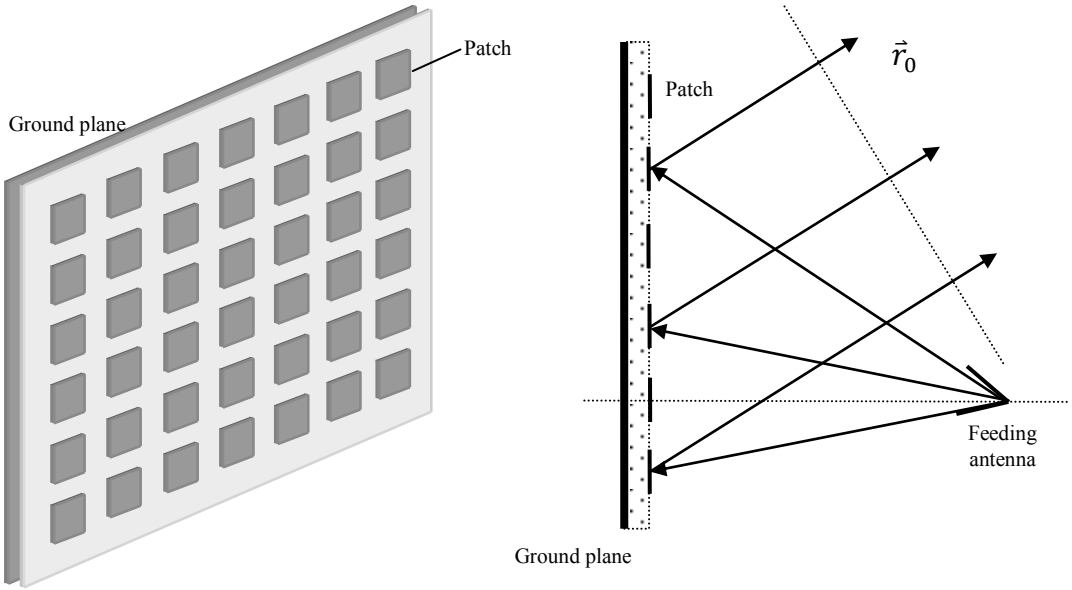

Fig.2.15 Geometry of the fixed microstrip patch reflectarray

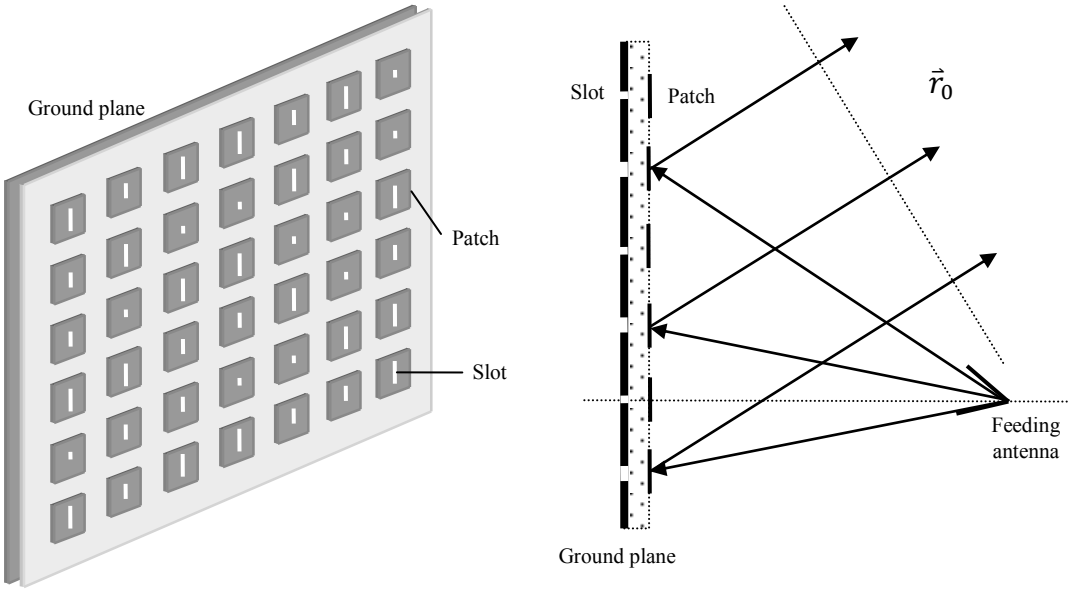

Fig.2.16 Geometry of the fixed slot reflectarray

[**71**] compared the performances of printed reflectarrays in different element shapes. The report compared reflectarrays in the configurations of rectangles, rectangles with stubs, ridge and dog-bone. The latter two designs showed a good trade-off between the range of the phase variances, fabrication complexity, the bandwidth and the cross-polarization level. The author suggested double-layer structures could improve the performance of the reflectarrays.

Reconfigurable reflectarrays

We know reconfigurable antennas brings great advantages in system functionality and freedom. As the development of emerging technologies continues, a great number of novel technologies will be used in reflectarrays.

A survey [**66**] summarized three general approaches to reconfigure reflectarrays: tunable resonator, guided-wave, and element rotation. Fixed reflectarrays modify their element geometry to change the operating frequency. Tunable resonators have been known for a long time to tune the antennas electronically, for example, varactor diodes. The varactor diodes integrated in the resonators can tune the phases of resonators. Another way to reconfigure a reflectarray is using guided wave. Guided waves such as

transmission lines can change the current path and electronic length of the resonator. As shown in **Fig.2.17**, one unit cell of a resonator reflectarray consists of multiple conducting strips connected by switches. The lengths of the resonators are changed by configuring the switches such as PIN diodes, MEMS switches. The element rotation technique is a specific method for circular-polarized (CP) reflectarrays. As shown in **Fig.2.18**, the unit cell of a CP spiraphase-type reflectarray [**72**] consists of a circular ring resonator and radial stubs connected by reconfigurable components e.g. PIN diodes. The geometry of the spiraphase resonators are optimized to operate at the millimetre-wavelength frequency. Electronically switching the elements can steer the beams between 0° and 50°. More sophisticated systems can provide features such as dual-polarizations [**73**], dual band [**27**] etc.

2.3.4 Summary

The field of antenna arrays is full of challenges. Many of the antenna arrays and reflectarrays can provide powerful functions such as beamforming and beamsteering. There are also challenges such as bandwidth, tuning ability/linearity, mm-wavelength frequency applications, hardware cost, polarizations etc. Scientists have proposed

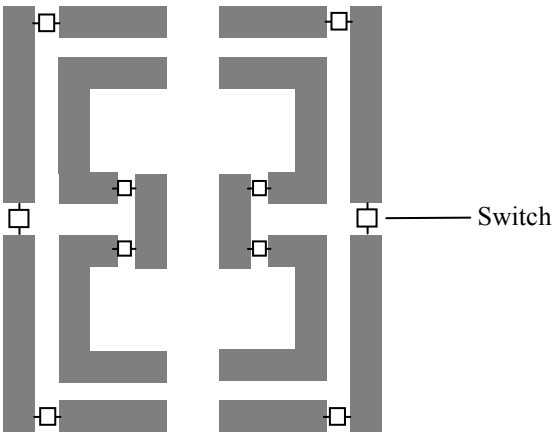

Fig.2.17 An example of a resonator reflectarrays unit cell. The element consists of switch-connected strips. The length of the resonator is configured by the switches.

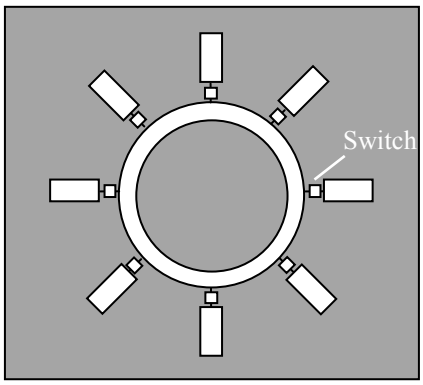

Fig.2.18 The unit cell of a circular polarized spiraphase reflectarray [**72**]. The scattering element consists of a ring slot resonator and switchable radial stubs.

solutions to these challenges using new materials, various reconfigurable approaches, different shapes and element layout, multi-layer structures. TMRAs benefit from previous research outcome on antenna arrays and try a new perspective to minimize the hardware cost without sacrifice of performance.

2.4 Conclusion

Section 2.2 has reviewed several approaches to reconfigure antennas. Every technique has their own merits and disadvantages. A good reconfigurable device should be examined in various perspective including bandwidth, power handling, power consumption, loss, maturity, price, robust, fabrication complexity, etc. PIN diodes, as mature technology, have both stable performance and reasonable cost. They are a good choice as the switches of time-modulated reflector-arrays.

Section 2.3 reviewed antenna arrays especially phased arrays and reflectarrays. Antenna arrays can provide functions such as beam steering and beam forming. They are used in applications such as object finding and tracking, multi-channel communications, space telescoping, directive communications, direction finding, etc. Scientists have tried various approaches to improve the functionalities and performance of antenna arrays and

lower the cost. Comparing to conventional approaches use in antenna array especially reflectarrays, TMRAs can produce beamforming and beam steering functions with simpler hardware structure. They aim to provide an affordable alternative to antenna array application with similar functions.

Chapter 3 TIME-MODULATED ARRAYS AND REFLECTOR-ARRAYS

Chapter 2 have reviewed methods to control the radiation characteristics of antenna systems. Some of these approaches are static such as change of antenna sizes, shapes and layouts. Some dynamic techniques employ electronically reconfigurable components such as PIN diodes, MEMS switches, varactor diodes and ferro-electric materials. More sophisticated methods includes hybrids of two or more technologies. These reconfigurable technologies help the antenna systems provide useful features such as multi-band, high gain, adaptive beamforming, beam steering, etc. Phased arrays are one of the popular techniques, which manage the radiation characteristics by changing the phases of individual antenna elements. Sometimes, it is an advantage using 'time' to control the element states.

Time-modulated arrays are antenna arrays where 'time' is added as a parameter to control the element states. Shown in **Fig.3.1,** the layout of a TMA is similar to that of phased arrays (in **Fig.2.9**) driven by phase shifters and corporate feeding networks. In a TMA however, simple SPST switches are used to control the operating states of individual antennas. The switches are used to energize the antenna elements of the TMA, in a predefined periodical sequence. The shape of the periodical sequence determines the radiation characteristics of the TMA system. Because of the periodically switching the elements, the TMA radiates signals not only at the fundamental (or driven) frequency of the array, but also at harmonic frequencies. The harmonic, or sideband, frequencies occur both above and below the fundamental frequency at offsets determined by multiples of the element switching frequency.

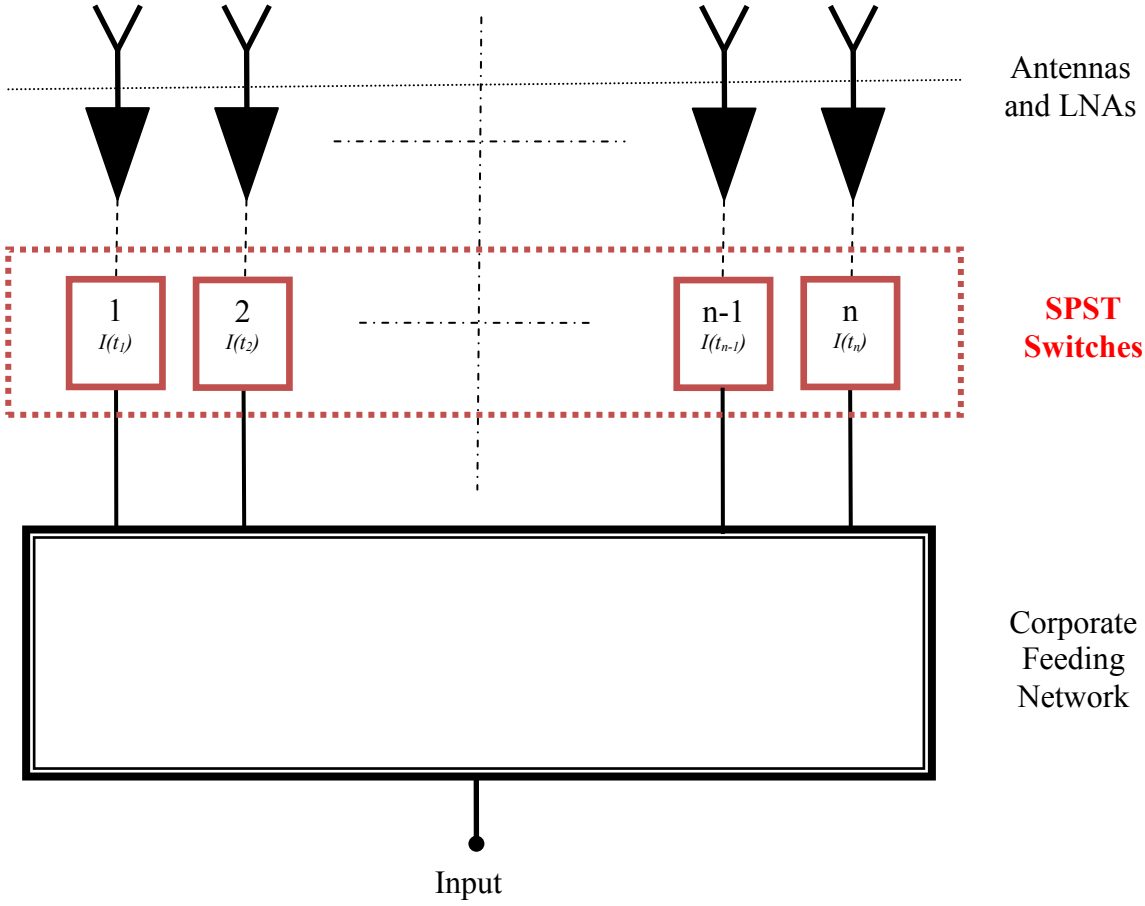

Fig.3.1 Topology of an N element time modulated array: Antenna elements are controlled by SPST switches, array are fed by corporate feeding network.

These main disadvantage of TMAs is power efficiency. Since sidebands are generated at harmonic frequencies, it is un-avoidable that energy will spread to sidebands. Scientists have tried use various methods **[3-7]** to increase efficiency. However, it is still impossible to eliminate sidebands. Secondly, the switching of elements must be precisely controlled by time. This requires the switches to have a instant response to control signals. If the switches have a significant delay to the control signals, distortions will be found in formed beam patterns. Thirdly, by the time of this thesis, most of the research activities on TMAs are focus on theoretical analysis of TMAs and simple linear TMA prototypes. There are very few publications introducing TMAs as a part of a comprehensive system

or an application. More research contributions on TMA prototypes and applications is expected.

3.1 Time modulated array numerical analysis

Now consider an N element linear time modulated array of equally spaced switch-controlled elements. Assume each element is excited by a source with an amplitude A_n and phase a_n. The elements have an identical radiation pattern $p(\theta)$, where θ is the radiation angle. The antennas are operating at the frequency of *f*. The output of the array is given as [**8**]

$$E(\theta,t) = p(\theta)e^{j2\pi ft}\sum_{n=1}^{N} A_n e^{ja_n}e^{jb_n}I_n(t) \qquad \textbf{Eq.3.1}$$

where element steer factor $b_n = (n-1)kdsin\theta$, k is the wavenumber in free space, d is the element spacing. $I_n(t)$ is the periodic element switch on-off time sequence. Suppose the repetition period is *T*. The total array output in **Eq.3.1** can be expressed in the Fourier series as

$$E(\theta,t) = \sum_{m=-\infty}^{\infty} C_m \cdot e^{\frac{-j2\pi mt}{T}} \qquad \textbf{Eq.3.2}$$

where m is a integer. C_m is Fourier coefficients of $E(\theta,t)$,

$$C_m = p(\theta)e^{j2\pi ft}\sum_{n=1}^{N} \mathrm{A_n}e^{ja_n}e^{jb_n}\cdot\frac{1}{\mathrm{T}}\int_0^{\mathrm{T}}\left[I_n(t)\mathrm{e}^{\frac{-j2\pi mt}{T}}\right]dt \qquad \textbf{Eq.3.3}$$

For simplicity, assume the all element phases a_n and amplitudes A_n are equal where $a_n = 0$ and $A_n = 1$. All elements are assumed to share an isotropic radiation pattern so that $p(\theta) = 1$. Hence, the total array output in **Eq.3.2** can be rewritten as

$$E(\theta,t) = \sum_{m=-\infty}^{\infty} e^{j2\pi ft}\cdot e^{j\frac{2\pi mt}{T}}\sum_{n=1}^{N} e^{jb_n}\cdot\frac{1}{T}\int_0^{T}\left[I_n(t)e^{\frac{-j2\pi mt}{T}}\right]dt \qquad \textbf{Eq.3.4}$$

As a consequence of periodically time-switching the elements, **Eq.3.4** shows the reflected signal contains not only signals at fundamental or illumination frequency f but also sidebands at harmonic frequencies given by $f \pm \frac{m}{T}$, where m is an integer (see **Fig.3.2**). The radiation pattern for the m-th harmonic frequency ($m \neq 0$) is

$$\mathrm{E}_m(\theta) = \sum_{n=1}^{N} e^{jb_n} \cdot \frac{1}{T} \int_0^T \left[I_n(t) \mathrm{e}^{\frac{-j2\pi mt}{T}} \right] dt \qquad \textbf{Eq.3.5}$$

A 4 element linear time modulated array is given an example. We assume that the antenna elements have an identical radiation pattern and exciting sources. The array elements are equally spaced by $d = \lambda/2$, where $\lambda = \mathrm{c}/\mathrm{f}_0$ is one full wavelength of the operating frequency of the array. The array element are presumed to be switched according to a pre-defined periodic time sequence shown in **Fig.3.3**. The time sequence is similar to the time sequence used in [**8**] to steer the beam of harmonic patterns in a 16 element linear time-modulated array. A full cycle of the time period T is 4 μs and the pulse width is 1 μs. **Eq.3.5** are used to calculate the theoretical performance of the four element time modulated array.

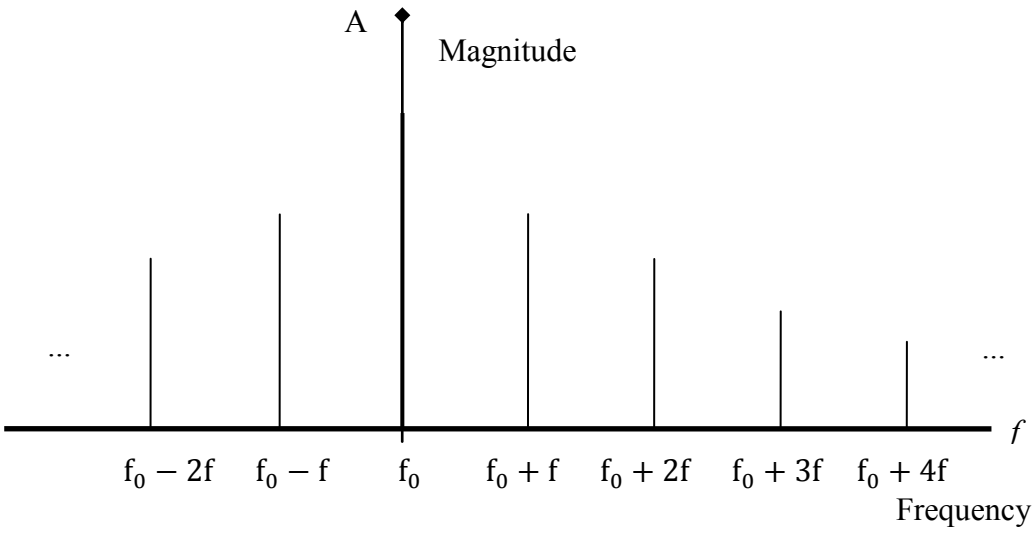

Fig.3.2 Magnitude spectrum of TMRA outputs: fundmental frequency and harmonic frequencies.

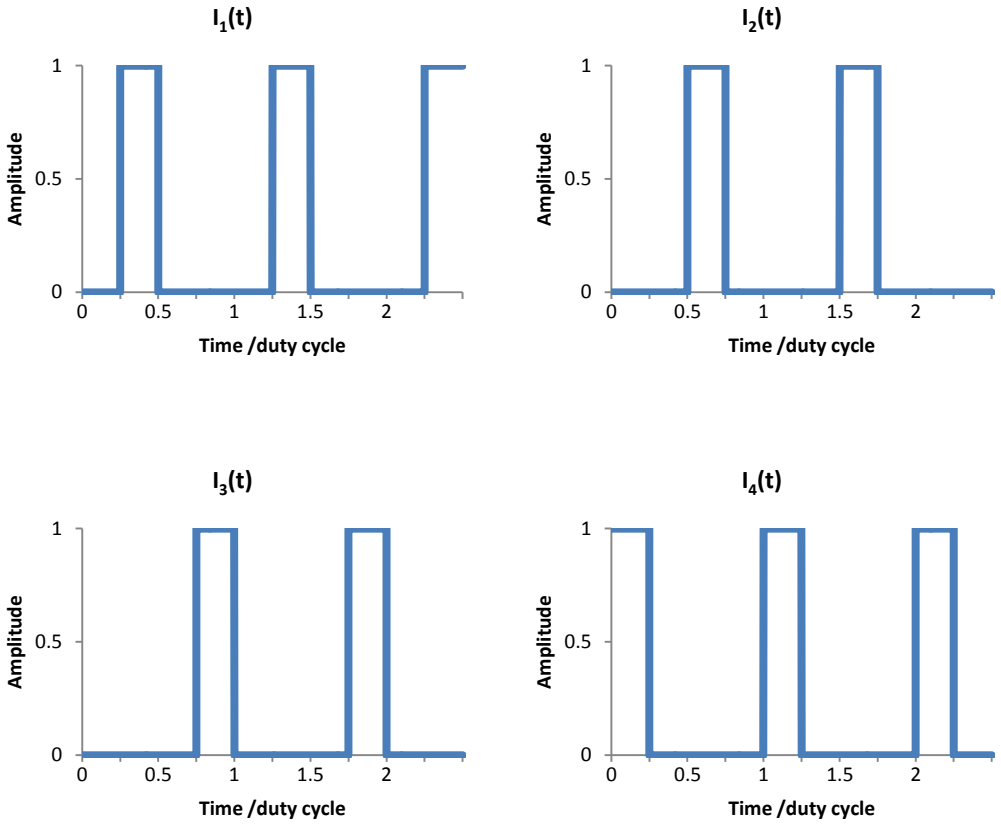

Fig.3.3 TMRA element switching sequence: elements are switched sequentially and progressively

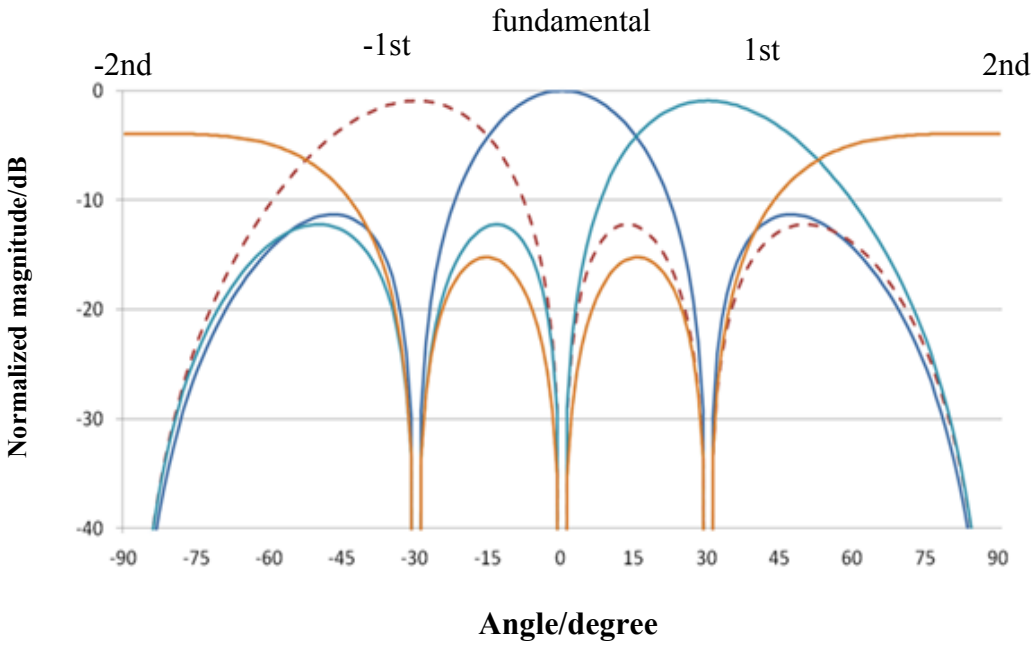

Fig.3.4 Beam patterns of the TMA. The magnitudes are normalize to the peak of the fundamental frequency.

In **Fig.3.4**, patterns of the fundamental and the first 2 positive and negative harmonic frequencies are shown with the formed beams steered to -90°, -30°, 0°, 30° and 90° respectively. A function of beam steering is realized by controlling the element switch time instead of using phase shift units.

3.2 Time modulated reflector-array description and modelling

Similar to the conventional reflector arrays, the proposed TMRAs consist of scattering elements and a feeding antenna. However, in the traditional reflector array, phases of scattering signals of the elements are controlled by phase-shifting units to change the radiating characteristics of the whole array system, for instance, beamforming. In a TMRA system, the phase shifting elements are replaced by time-controlled elements and beamforming is obtained by controlling the time-domain scattering characteristics of the array elements. Using pre-calculated time sequences, the TMRA is shown to produce functions such as beam steering and sidelobe control.

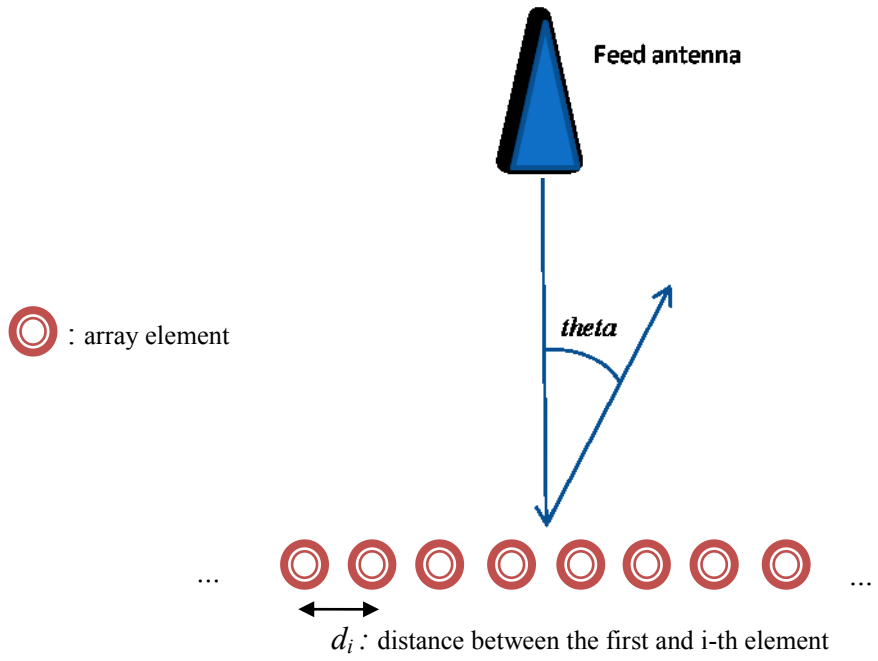

Fig.3.5 Time modulated reflector array model

Assume a simple model of a TMRA based on a linear array of scattering elements in **Fig.3.5**. The scattering elements of the array are considered to be reconfigurable in that they can be switched between non-reflecting (OFF) and strongly-reflecting (ON) states. In this model, inter-element coupling is ignored. It is assumed that the array elements radiate isotropically when active/ON. On the contrary, the elements have no reflected power when they are in-active/OFF. Consider now an *N*-element linear array fed by a plane-wave in the broadside direction. Assume that the *i-th* element *(i=1,N)* is switched between ON and OFF periodically at times defined by t_{ion} and t_{ioff}, where $nT_0 \leq t_{ion} \leq t_{ioff} \leq (n+1)T_0$ and T_0 is the time of one complete switching duty cycle and n is an integer. Under these circumstances, the periodic time-domain waveform generated by the TMRA may be described as

$$f(t,\theta) = e^{j2\pi ft} \sum_{i=1}^{N} E_i(\theta)\, exp(jb_i)\, I_i(t) \qquad \textbf{Eq.3.6}$$

In **Eq.3.6**, $E_i(\theta)$ is the scattering power pattern of the n-th element, $b_i = kd_i sin\theta$ is the element steer factor, $k = \frac{2\pi}{\lambda_c}$ is the wave number in free space, d_i is the position of the element and λ_c is the wavelength of the illuminating continuous wave signal. The element switching function, $I_i(t)$, is described by

$$I_i(t) = \begin{cases} 1, & nT_0 + t_{i_{on}} \leq t < nT_0 + t_{i_{off}} \\ 0, & others \end{cases} \qquad \textbf{Eq.3.7}$$

The equation of waveform of the TMRA is generally identical to that of the conventional TMA. The main difference is the switched controlled antenna elements are replaced by switchable scatterers.

A Fourier series expansion of **Eq.3.6** provides the far-field scattering pattern of the time modulated reflector array at any harmonic m $(m \neq 0)$, as

$$F_m(\theta) = \sum_{i}^{N} E_i(\theta)\, exp(jb_i)\, s_{im} \qquad \textbf{Eq.3.8}$$

where $s_{im}$are the Fourier series coefficients of $I_i(t)$

$$s_{im} = \frac{1}{T_0}\int_0^{T_0} I_i(t)\, e^{-jm\frac{2\pi}{T_0}t}\, dt \qquad \textbf{Eq.3.9}$$

s_{im} can be written in exponentiation form as,

$$s_{im} = \frac{sin\{\pi m(\tau_{ioff}-\tau_{ion})\}}{\pi m} e^{-j\pi m(\tau_{ioff}+\tau_{ion})} \qquad \textbf{Eq.3.10}$$

where $\tau_{ioff} = \frac{\mathrm{t_{ioff}}}{T_0}$ and $\tau_{ion} = \frac{\mathrm{t_{ion}}}{T_0}$. The derivation from **Eq.3.9** to **Eq.3.10** can be found in Appendix II. Hence, by controlling the ON/OFF switching times of individual elements, a set of equivalent complex weights $s_{im} = w_i = |w_i|e^{-j\beta_i}$ can be synthesized to control the scattering properties of the array elements. The relationship between complex weights and switching times for a particular element is [8]

$$\begin{aligned} |w_i| &= \frac{sin\{\pi m(\tau_{ioff} - \tau_{ion})\}}{\pi m} \\ \beta_i &= \pi m(\tau_{ioff} + \tau_{ion}) \end{aligned} \qquad \textbf{Eq.3.11}$$

Since the connection between the time sequence and weight is established, the weighting techniques using modern digital signal processing can be applied to the TMRA. In the following parts, TMRA reproduces two beamforming functions using conventional weighting methods.

3.3 Beam-steering characteristics of TMRA

Beam-steering is a function to change the main lobe direction of the overall array radiation pattern. It is used in the modern Digital Signal Processing (DSP) technology, and to realize commercial product such as digital radar [**74**] and directive loudspeakers [**75**]. Moreover, such idea is adopted in the optical system by changing the refractive index of the medium to realize beam-steering in the optical compact products [**76**]. Conventionally, relative magnitudes and phases of the elements signals are adjusted to

accomplish the beam steering function. However, in TMRA, the beam-steering can be realized by control the switch ON/OFF times of scattering elements.

Consider a specific example of time modulated reflector array. The proposed array contains 8 scattering elements, which are assumed to be identical isotropical scatterers. The scatterers are electronically controlled by switches, which can switch the scatterers between fully resonating and non-resonating states. The inter-element distance is half of the wavelength of the operating frequency ($d_i = (i-1)\lambda_c/2$).

The TMRA scattering elements are periodically switched according to the sequence shown in **Fig.3.6**. Such time sequence produces progressive phase shifts, β_i, at the harmonic frequencies defined by m ($m \neq 0$) [**8**]. The resulting scattered patterns at the fundamental frequency and the first 3 positive/negative harmonic frequencies are shown in **Fig.3.7**. The patterns resemble those obtained from a TMA described in [**8**] controlled by the same switching time sequence and demonstrate the characteristics of harmonic beam steering.

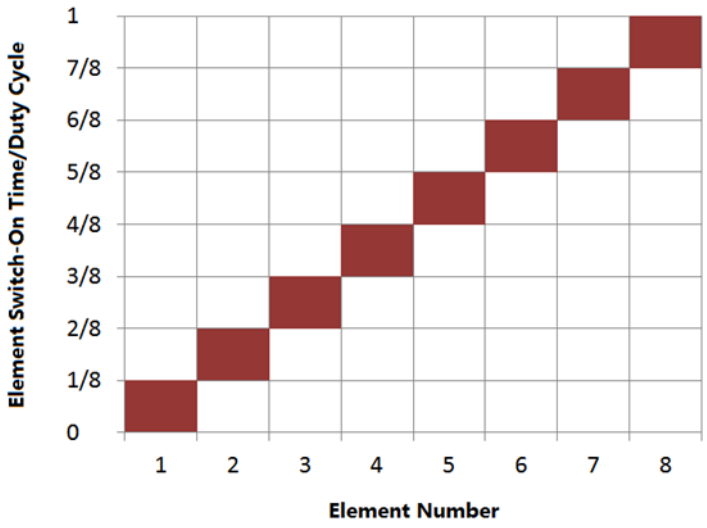

Fig.3.6 TMRA element switching sequence: elements are switched sequentially and progressively

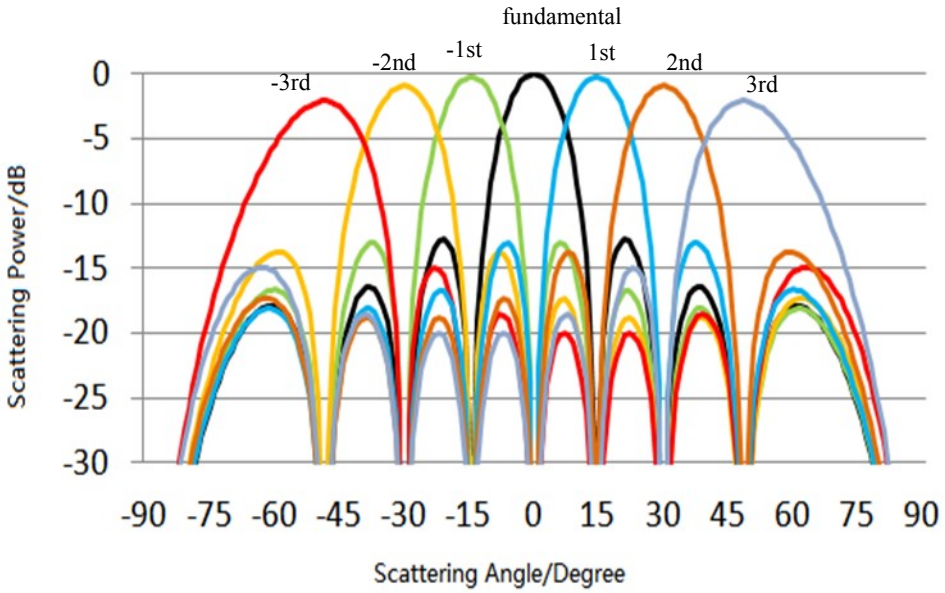

Fig.3.7 Scattering patterns from the ideal TMRA. These results are calculated using isotropic element patterns without element mutual coupling

Unlike the conventional phased array, the TMA and TMRA forms the scattering patterns of the fundamental and harmonics frequencies at the same time. One beam of a frequency has a maximum response at a certain direction where the rest of the beams of other frequencies has sharp nulls. This prevents the interferences between fundamental and harmonic frequencies so that the system can identify the direction of arrival by simply comparing the received powers at fundamental and harmonic frequencies.

3.4 Sidelobe control of TMRA

3.4.1 Minimum beamwidth sidelobe control

As shown in **Fig.3.8**, sidelobes are lobes local maximums of a radiation pattern, which are not the main lobe. In certain circumstances, sidelobes are unwanted, such as a directional antenna, which aims to emit the RF energy in one desired direction. The objective of sidelobe control is to suppress the sidelobe levels, which can reduce the interferences and improve the overall system robustness.

Beamforming functions are used to suppress sidelobes. Some dynamic adaptive beamforming techniques use optimization algorithms to increase the main lobe to sidelobes ratio. This methods involves advanced digital signals processing such as second-order cone approach [**77**] and gives a good suppression performance with additional features (beamforming). On the contrary, the mathematical beamforming weighting functions are easier to implement as no complex DSP modules required. The major focus of the mathematical approach is on the Dolph-Chebychev weighting, which produces constant sidelobes and a minimum beamwidth for sidelobes. In addition, Taylor weighting is also a choice when a constant sidelobe behaviour is not desirable [55].

The formula for Dolph-Chebychev weighting used in sidelobe suppression are summarized in [**78**]. The Chebyshev or Tschebyscheff polynomials are defined by a recursion relation [**78**]:

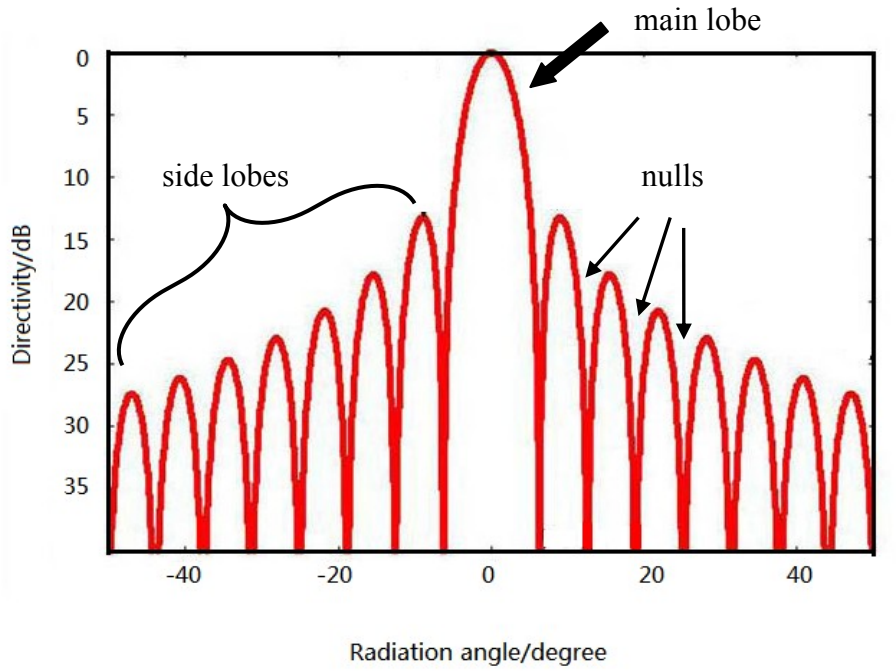

Fig.3.8 Radiation pattern of a typical antenna system with main beam and sidelobes

$$T_0(z) = 1$$
$$T_1(z) = z$$
$$T_2(z) = 2z^2 - 1$$
$$T_M(z) = 2zT_{m-1}(z) - T_{m-2}(z), m = 2, 3, \ldots \quad \textbf{Eq.3.12}$$

As shown in **Fig.3.9**, one important feature of the Chebyshev polynomials is that all polynomials have the equal wave crests in the range between $z = -1$ and $z = 1$. Dolph-Chebychev weighting uses the polynomials' coefficients to calculate the weights and produce a similar pattern with equal sidelobes. For an equally spaced linear array of antenna elements, assume the array is symmetric that the weight applied at the elements at location - d_i and + d_i are identical. If the array is centred at zero, the array factor can be written as [73],

$$AF = \sum_{n=1}^{M} w_n e^{-\frac{jk(2n-1)d}{2}cos\theta} + \sum_{n=-M}^{-1} w_n e^{-\frac{jk(2n-1)d}{2}cos\theta} \ (Even\ array)$$
$$AF = \sum_{n=-M}^{M} w_n e^{-jkndcos\theta} \ (Odd\ array) \quad \textbf{Eq.3.13}$$

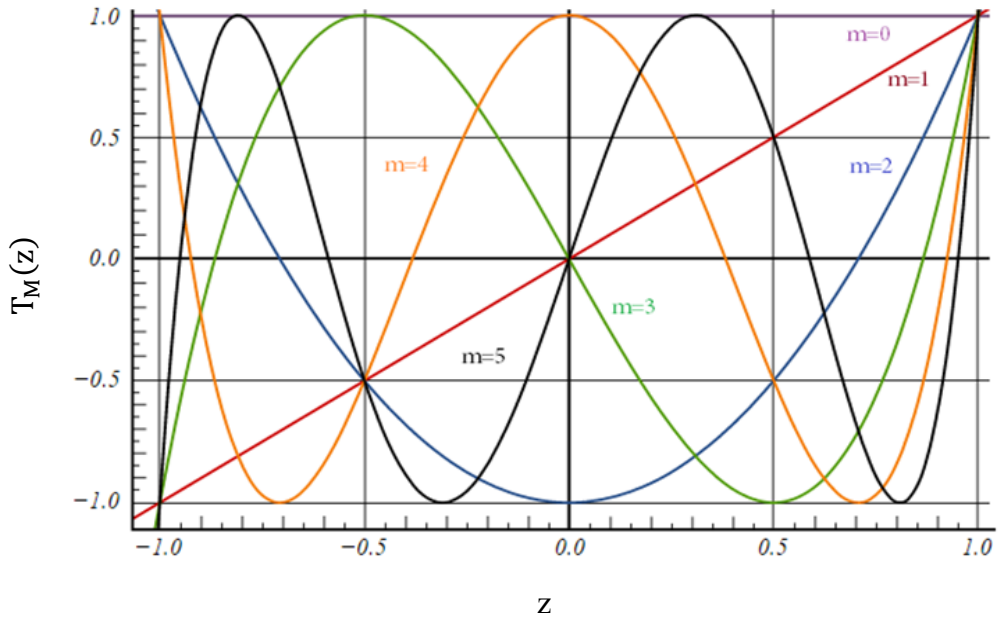

Fig.3.9 The first few Chebyshev polynomials in the domain $-1 < z < 1$: $T_0(z), T_1(z), T_2(z), T_3(z), T_4(z), T_5(z)$

where *d* is the inter-element distance, *k* is the wave number, *M* is the number of elements on one side of the array. We now use the complex-exponential formula $cos(x) = \frac{e^{jx}+e^{-jx}}{2}$ to rewrite **Eq.3.13** as

$$AF = \sum_{n=1}^{M} w_n \, cos[(2n-1)u] \;\; (Even\ array)$$
$$AF = \sum_{n=0}^{M} w_n cos\,(2nu) \;\; (Odd\ array) \qquad \textbf{Eq.3.14}$$
$$u = kdcos\theta/2$$

Next step is to expand **Eq.3.14** to match the form of a Chebychev polynomial in order to obtain the unified-level sidelobes. We need the following cosine functions

$$\begin{aligned} &cos(0) = 1 \\ &cos(u) = cos\,(u) \\ &cos(2u) = 2\,cos^2(u) - 1 \\ &cos(3u) = 4\,cos^2(u) - 3cos\,(u) \\ &cos(4u) = 8\,cos^4(u) - 8\,cos^2(u) + 1 \\ &\quad ... \end{aligned} \qquad \textbf{Eq.3.15}$$

Then *cos(u)* is substituted by t/t_0, where t_0 is the parameter to control the sidelobe levels [**78**]

$$t_0 = cosh\left(\frac{acosh(S)}{N-1}\right) \qquad \textbf{Eq.3.16}$$

where *S* is the linear value for side lobe levels (SLL). N is the total number of elements. The array factor *AF* can be finally in a form of polynomial, which is now used to match a Chebyshev polynomial $T_m(t)$. The weights w_n are calculated by the polynomial coefficients.

We now consider a specific example of an 8 element antenna array using Chebychev weighting. Assume the isotropic scattering sources are spaced at half wavelength of the operating frequency. Design a Chebychev weight results in sidelobes reduced at 30 dB ($S = 31.6223$) , the array factor is

$$AF = \sum_{n=1}^{4} w_n \cos[(2n-1)u] \qquad \textbf{Eq.3.17}$$
$$u = \pi \cos\theta / 2$$

Using the cosine function in **Eq.3.15**, *AF* can be rewritten as,

$$AF = w_1 \cos(u) + w_2 \cos(3u) + w_3 \cos(5u) + w_4 \cos(7u)$$
$$AF = \cos(u)\,(w_1 - 3w_2 + 5w_3 - 7w_4) + \cos^3(u)(4w_2 - 20w_3 + 56w_4) \qquad \textbf{Eq.3.18}$$
$$+ \cos^5(u)(16w_3 - 112w_4) + \cos^7(u)(64w_4)$$

the SLL parameter t_0 is

$$t_0 = \cosh\left(\frac{a\cosh(31.6223)}{N-1}\right) = 1.1807 \qquad \textbf{Eq.3.19}$$

Substituting *cos(u)* for *t/1.1807*,

$$AF = t\frac{(w_1 - 3w_2 + 5w_3 - 7w_4)}{1.1807} + t^3\frac{(4w_2 - 20w_3 + 56w_4)}{1.1807^3}$$
$$+ t^5\frac{(16w_3 - 112w_4)}{1.1807^5} + t^7\frac{64w_4}{1.1807^7} \qquad \textbf{Eq.3.20}$$
$$= T_7(t)$$
$$= 64t^7 - 112t^5 + 56t^3 - 7t$$

hence the calculated weighting is

$$w_4 = 3.1987, w_3 = 6.3265, w_2 = 9.9025, w_1 = 12.1958 \qquad \textbf{Eq.3.21}$$

As stated in the beginning, the weights are symmetric. Normalizing weights to their maximum value, the weights applied for the eight element array from left to right are

$$w_{-4} = 0.2662, w_{-3} = 0.5187, w_{-2} = 0.812, w_{-1} = 1 \qquad \textbf{Eq.3.22}$$
$$w_1 = 1, w_2 = 0.812, w_3 = 0.5187, w_4 = 0.2662$$

For a conventional antenna array, a low noise amplifier can be used to apply the weights to each of the elements. The calculated weights in **Eq.3.22** is applied in the array factor,

$$F(\theta) = \sum_{i}^{N} exp\left(-j\frac{2\pi}{\lambda_c}(i-1)d\cos\theta\right) w_i \qquad \textbf{Eq.3.23}$$

where λ_c is the wavelength of operating frequency and *d* is the inter-element distance,

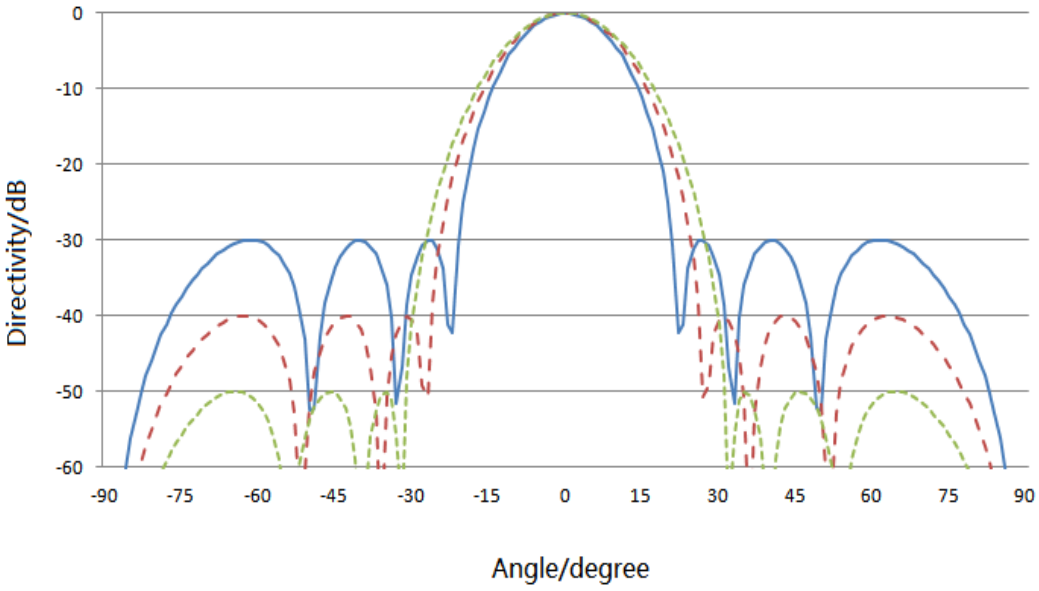

Fig.3.10 Beam patterns of 8 element array with sidelobes at -30, -40, -50 dB calculated using Chebychev weighting

which is half wavelength $\lambda_c/2$. The calculated beam pattern is shown in **Fig.3.10** along with other two sidelobe suppress patterns with sidelobes level suppressed at -40 dB and -50 dB respectively. We now see that the sidelobes are suppressed at the desired power levels.

3.4.2 Sidelobe control applied to the TMRA

To apply the Chebyshev weighting function to the TMRA, a connection between the time sequence and the Chebyshev weights should be created. Unlike the beam steering example shown in **Section 3.3**, sidelobe suppression can be operated at the fundamental frequency of the TMRA. The far-field scattering pattern of the TMRA at the fundamental frequency is given by

$$F(\theta) = \sum_{i}^{N} E_i(\theta)\, exp\left(-j\frac{2\pi}{\lambda_c} d_i sin\theta\right)\left(t_{ioff} - t_{ion}\right) \qquad \textbf{Eq.3.24}$$

Now apply the Chebyshev weighting function, w_i as a function of the element switch-ON/OFF times

$$w_i = t_{ioff} - t_{ion} \qquad \textbf{Eq.3.25}$$

Assuming that all the elements are switched-ON at the same instance (the beginning of each cycle), the elements switch-ON and switch-OFF time are as

$$t_{ion} = 0 \qquad t_{ioff} = w_i \qquad \textbf{Eq.3.26}$$

Now consider the example of an eight-element TMRA. The array elements are energised according to the time-switching sequence shown in **Fig.3.11**. The weights are pre-calculated using -30 dB Chebyshev weighing function, which is identical to **Eq.3.22**. We assume that all the TMRA elements scatter an identical isotropical pattern ($E_i(\theta) = 1$) and the inter-element distance is half wavelength at the fundamental frequency. The obtained sidelobe-suppressed scattered power pattern at the fundamental frequency from the TMRA is shown in **Fig.3.12.** along with a reference non-suppressed scattered power pattern from a uniform array. The figure shows that -30 dB sidelobe suppression is

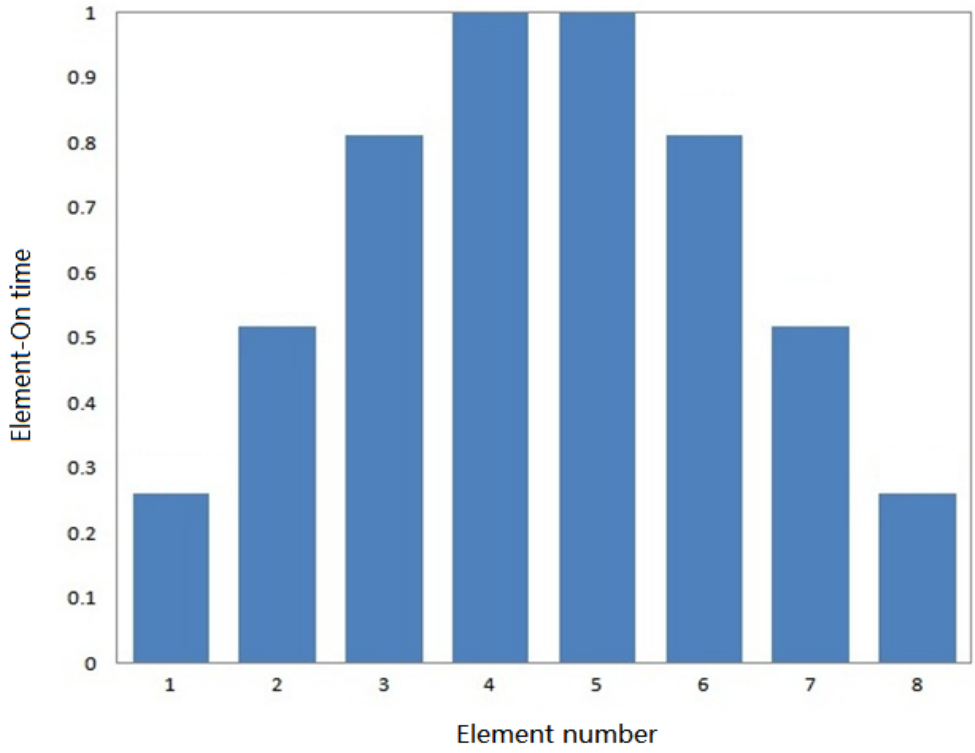

Fig.3.11 TMRA elements' switching sequence: elements are energised at the beginning of each cycle.

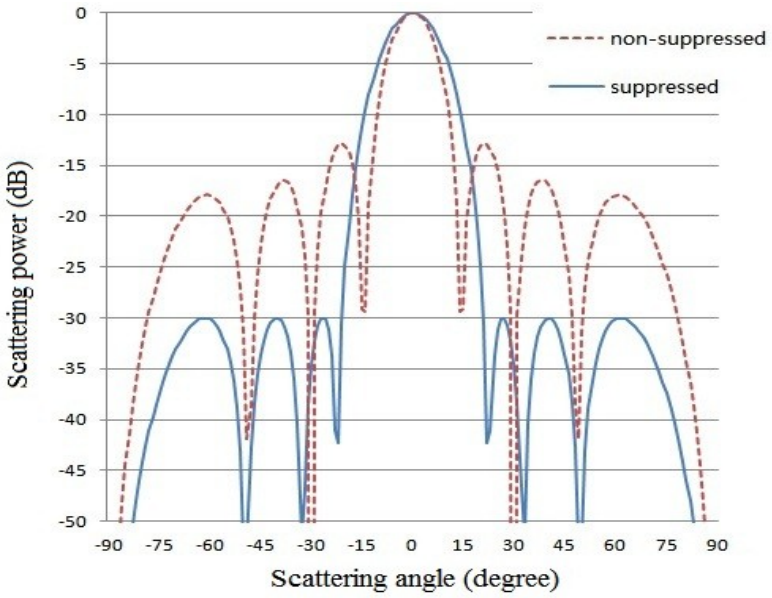

Fig.3.12 Sidelobe suppression scattering patterns for the TMRA, calculated using isotropic element patterns and without mutual coupling

achieved and the power pattern is identical to that obtained from a conventional antenna array shown in **Fig.3.6**. The TMRA now successfully reproduces the sidelobe suppression on the fundamental frequency using the element switching times.

3.5 Conclusion

This chapter introduces the fundamentals of time-modulated reflector array. Unlike the conventional TMAs, which are based on array systems with complex feeding networks, the TMRAs take the form of reflector arrays in which element time-switching is used instead of element phasing to control the array radiation characteristics. A simple model of a TMRA system is provided to explain the operating mechanism along with a detailed numerical analysis. Using pre-calculated time sequences, the TMRA can produce functions such as beam steering and sidelobe control.

An 8 element TMRA has been configured to produce a beam steering function. Formed beams at the fundamental and harmonic frequencies are steered to desired

directions. This is due to the progressive phase change at harmonic frequency determined by the harmonic number *m* in **Eq.3.11**. In addition, the number of elements of a TMRA determines harmonic number in a given frequency range as well as the beam density in the formed scattering patterns. For instance, the eight element TMRA can generate 7 directive beams from -90 to 90 degrees including fundamental and first three positive and negative harmonic patterns. A 16 element array can generate 15 directive beams including fundamental and first 7 positive and negative harmonic patterns [**8**]. There is no particular reason to choose the number of TMRA to be 8. However, as same as phased arrays, more elements in an array can increase ability to form desired beam patterns such as multi-nulling.

In addition, the 8 element TMRA has generated low sidelobe level radiation pattern at the fundamental frequency. The pre-calculated Chebyshev weights are applied to a time sequence, which generates a -30 dB sidelobe level radiation pattern. Results have been presented to compare the performance of a system analysed using isotropic elements and array-factor theory to that of a conventional TMA system and phased array system conducting similar functions.

The number of element in a TMRA affect the system freedom

Chapter 4 REALISTIC TMRA BASED ON BOWTIE DIPOLE ELEMENTS

4.1 Introduction

Chapter 3 have introduced the time-modulated reflector array based on the ideal isotropic elements. However, assumptions such as isotropic elements are non-realistic and inter-element coupling has also not been taken into account. This chapter introduces a more practical TMRA system based on the PIN-diode loaded bowtie dipole elements. An experimental implementation of the bowtie dipole TMRA is introduced along with a full wave electromagnetic simulation. In addition, a prototype of the TMRA is made and measured in a NRL arch reflectivity system. Both the simulation and measurement results show that the bowtie dipole TMRA can conduct a beam-steering function without the need of complex feeding network and phase shift units.

4.2 Experimental TMRA system

The experimental TMRA system, shown in **Fig.4.1**, consists of a reflector array (TMRA) and its control circuit. The reflector array consists of 8 rows of 8 series connected bowtie elements. The bowtie dipole element design was chosen because it was successfully used in previous work on a phase modulating RF tag [**79**]. Each row of the TMRA has 8 elements, which are connected in series in a form of a sub-array. The sub-arrays can provide the TMRA system with increased gain compared to a linear array of single dipole elements. Each sub-array is connected to one of the eight parallel control signals generated by the control circuit. The control circuit consists of Arduino UNO

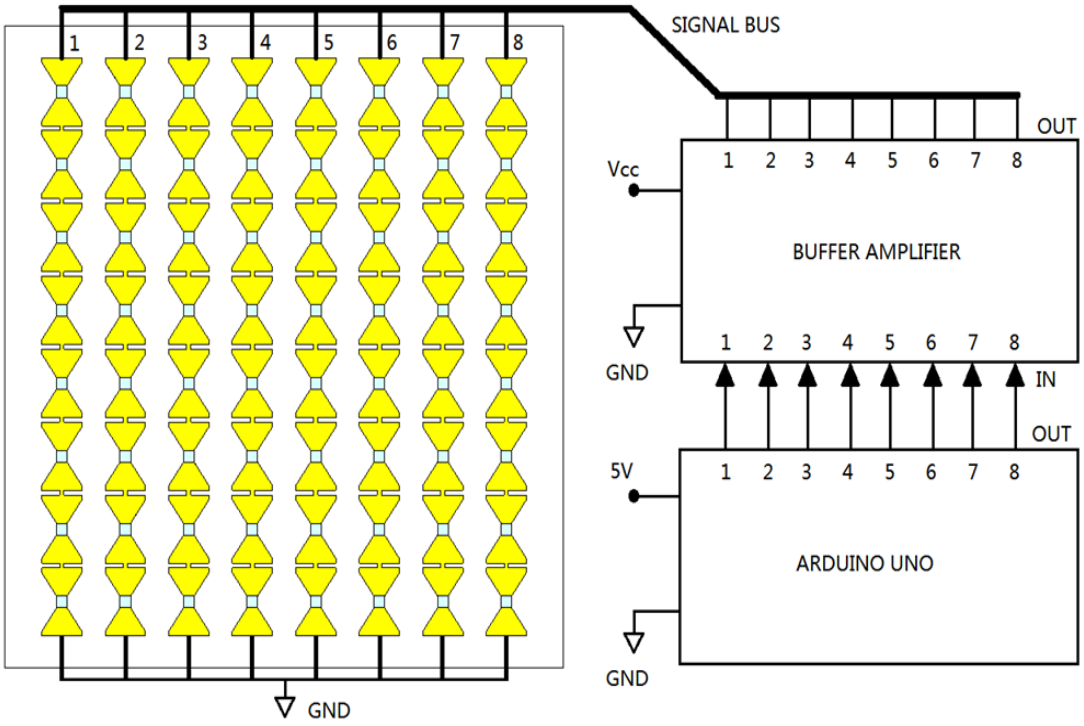

Fig.4.1 Model of experienment TMRA: consists of a reflector array (left) and control circuit (right).

processor [**80**] and a buffer amplifier. A program is loaded to the Arduino UNO processor to generate 8 parallel pulses in the predefined sequence. The pulses are then amplified in the buffer amplifier before it applied to the TMRA elements. By controlling the time sequence loaded to the ARDUINO UNO processor, the scattering characteristics of the TMRA can be controlled. The following content will look into the reflector array and the control circuit.

4.2.1 Reflector array based on bowtie-dipole design

Shown in **Fig.4.2**, the size of the prototype TMRA is 139 mm by 147 mm and consists of 8 rows of 8 series connected bowtie dipole elements. The element spacing is 15 mm, which corresponds to approximately a half wavelength of the illuminating frequency (9.5 GHz). The array elements were printed on a FR4 PCB board with a relative permittivity $\varepsilon_r = 4.4$ and thickness $d = 1.6\,mm$. PIN-diodes (Siemens BA585)

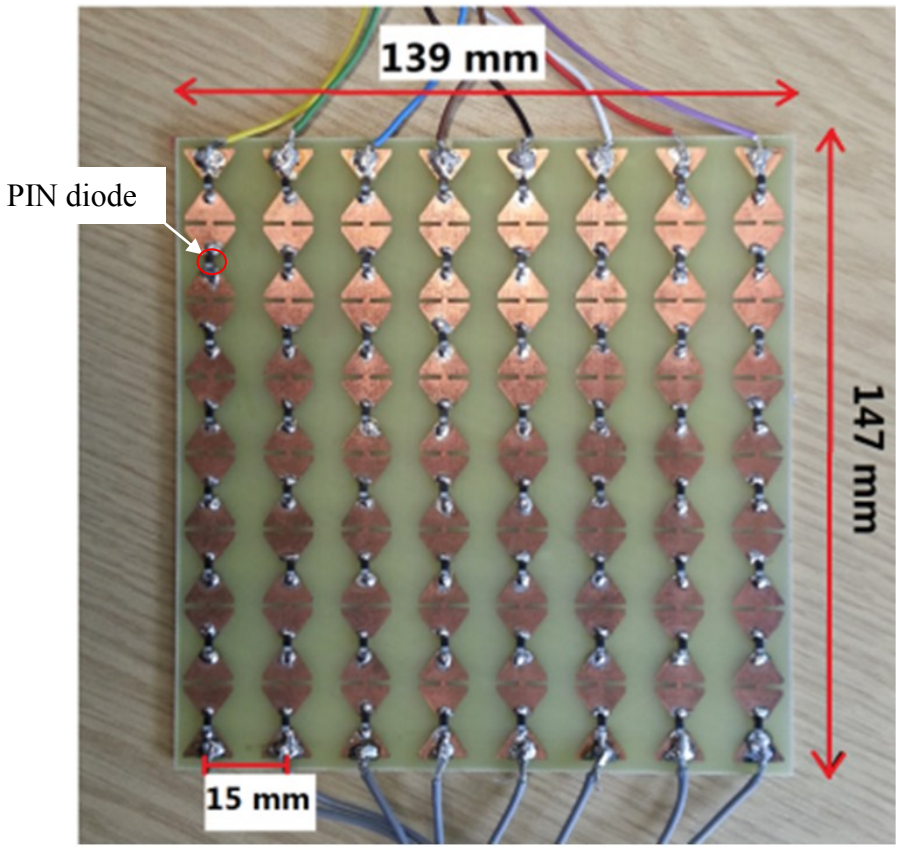

Fig.4.2 A photograph of the bowtie dipole TMRA prototype: size 139mm x 147 mm; PIN diodes are hand soldered at the midpoint of the bowtie elements.

[**81**] were hand soldered at the mid points of the bowtie elements. The PIN diode can easily be implemented into the scatterers without additional bias comparing to FET and MEMS switches as FETs need a third terminal and MEMS require two additional bias circuits. When the PIN diodes are forward biased (low diode impedance), the bowtie elements are effectively short circuited and become strongly scattering, but they reflect weakly when un-biased (high diode impedance state). Eight elements in a row were connected using short joins. Although the joins will affect the isolation of individual elements, this is the simplest way to bias the PIN diodes without adding any additional component. In the future design, using inductors between elements can help to isolate the bowtie elements.

The single bowtie dipole element consists of two trapezoid copper arms connected with PIN diode at the middle point. Shown in **Fig.4.3**, the total length of a bowtie single element is L = 14.5 mm, which corresponds to approximately half wavelength of the working frequency 9.5 GHz. The width of the bowtie is W = 9.5 mm and rest of the geometries can be found in Table I. PIN diodes are usually modelled as short/open circuit

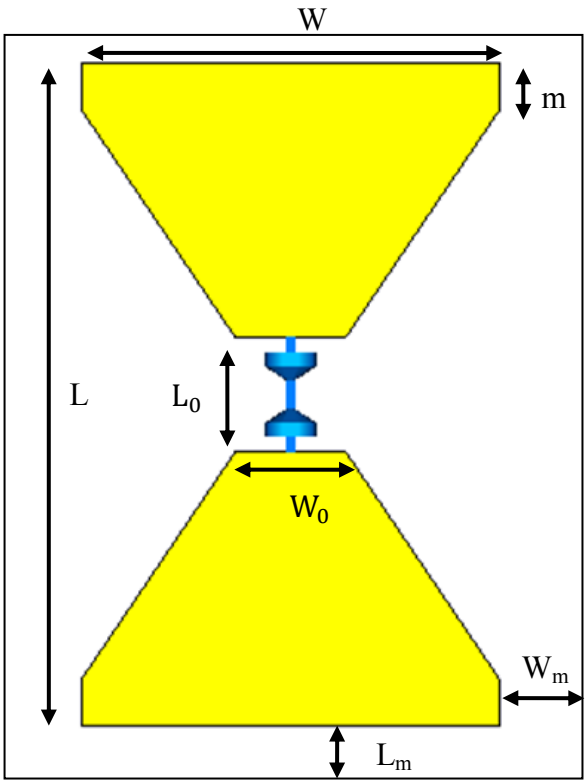

Fig.4.3 Dimension of a single electromagnetic scatterer

Table I DIMENSIONS OF A SINGLE BOWTIE DIPOLE ELEMENT

Name	***W***	***L***	L_0	W_0
Value (mm)	9.5	14.5	2.5	2.5
Name	W_m	L_m	***m***	
Value (mm)	2.75	0.5	1	

when they are forward-biased/zero-biased in a full wave simulator. However, from previous experience using phase modulated RF tag [**79**], it is better to use equivalent circuits shown in **Fig.4.4**. For both bias states, the circuits have the same electrical characteristics of series resistance R_s, inductance L and capacitance C. However, the parallel resistance R_p is controlled by the voltage applied to PIN diodes. When the PIN

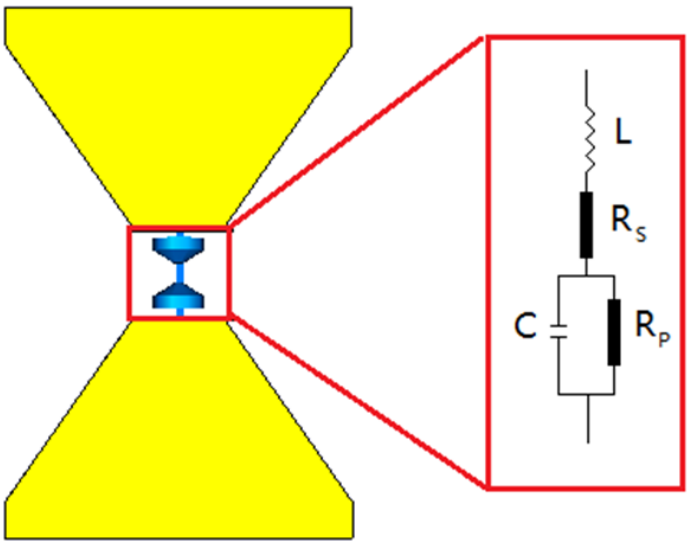

L	R_S	C
0.45 nH	2 Ohms	85 fF
R_P (Forward Biased)	R_P (zero-biased)	
5 Ohms	5k Ohms	

Fig.4.4 Equivalent circuit of ON/OFF status of BA585 PIN diode [**82**], listed values are from previous research experience on phased modulated RF tags tags **[72]**.

diode is zero-biased, R_p is very large (5k Ohms) and PIN diode operates as an open circuit. When the PIN diode is forward biased, R_p is very small, which shunts the parallel capacitor and the PIN diode acts as a small impedance circuit. These values listed in **Fig.4.4** are obtained from my previous research experience on phase modulated RF tags [**79**] and have been verified in both simulations and measurements. The driving point impedance of the bowtie scatterer is 26 Ω, which was obtained from CST Microwave

Studio using T-solver. The impedance of BA585 at 9.5 GHz are 28 Ω (when ON) and 170 Ω (when OFF) according to the equivalent circuit.

The performance of single element bow-tie scatterer was evaluated in CST Microwave studio. Boundary conditions in CST were set as *open (add space).* The scatterer was illuminated by a plane wave in broadside (theta = 0°). The scatterer's dimensions and PIN diode equivalent circuit parameters were configured according to the **Fig.4.3** and **Fig.4.4**. Farfield monitors were setup at 9.5 GHz to record the performance of the bowtie dipole scattering element. **Fig.4.5** plots the farfield power patterns of the single bow-tie dipole when its PIN diode is forward biased and zero-biased. When the PIN diode is forward biased (shown in solid line), the scatterer radiates isotropically -75 dBW/m^2 scattering power. On the contrary, the power is 20 dB less when the PIN diode is zero-biased (shown in dash line). The scattering pattern is no longer isotropic.

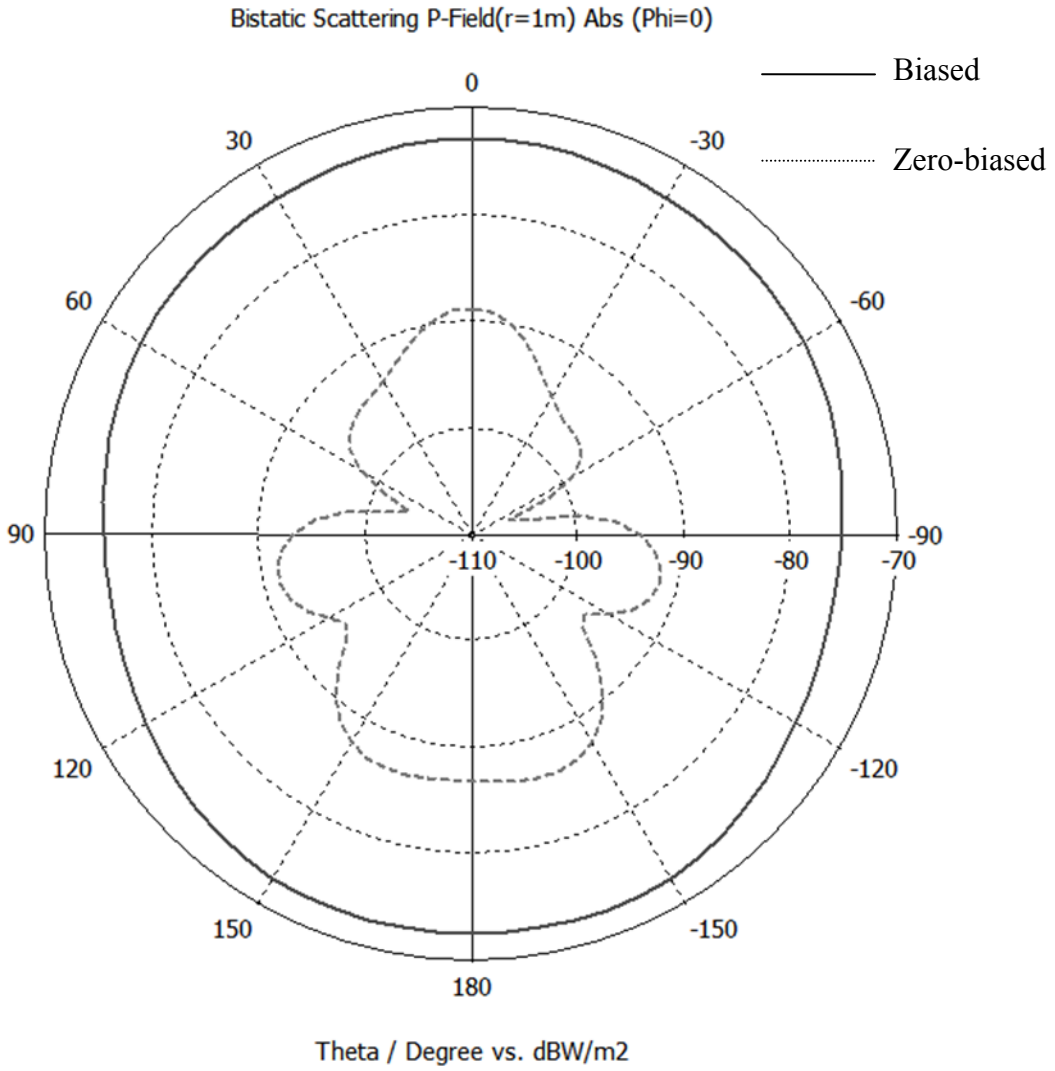

Fig.4.5 Farfield scattering power patterns of the single bow-tie dipole at 9.5 GHz when the loaded PIN diode is forward biased and zero-biased.

4.2.2 TMRA control circuit

The control circuit, shown in **Fig.4.6**, is based around the Arduino UNO R3 programmable platform [**80**] combined with a signal conditioning amplifier circuit. The Arduino UNO is a low cost, simple single-board microprocessor (SBM) with clock speed of 16 MHz . A program was preloaded in to the Arduino UNO to generate 8 parallel pulses modulating signals according to a pre-defined time sequence. The shortest switching period is 8 μs, which gives the largest switching frequency of 125 kHz. The

buffer amplifiers are used to amplify the pulses and to drive the PIN diodes of the TMRA. As shown in **Fig.4.7**, the buffer amplifier adopts a common-emitter design of an NPN bipolar-junction-transistor 2N2369 [**83**], which will invert the input signal. Both R_1 and R_2 are set to be 820 Ω to provide the PIN diode 18 *mA* current when $V_{in} = 0\ V$. When V_{in} = 5 V, the transistor become saturated, the current can flow from transistor's collector to base which results PIN diodes of TMRAs be shunt.

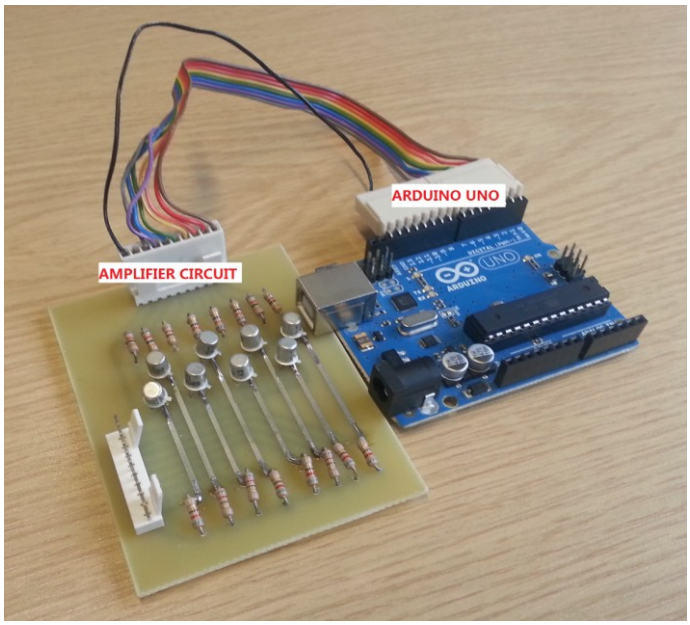

Fig.4.6 A picture of TMRA control circuit which consists of a Arduino UNO SBM and a grid of buffer amplifiers.

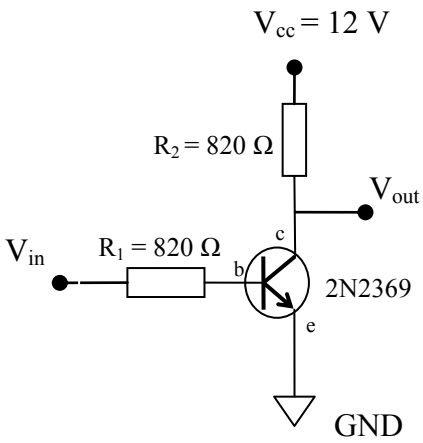

When V_{in} is zero, the buffer amplifier can provide a 18 *mA* current to TMRA.

When V_{in} is 5 V, TMRA is shunt. V_{out} is zero.

Fig.4.7 The circuit of a buffer amplifier used to amplify the control pulses generated by the Arduino UNO SBM.

4.3 Full-wave simulations of the TMRA to conduct beam steering function

The analysis of the TMRA given in Chapter 3 is based on Array-Factor, i.e. the assumption that the scattering pattern of each individual array element is isotropic and of unit magnitude. However, such assumption is not realistic as it does not take into account the type of array element nor the effects of inter-element (or mutual) coupling. Hence in this section the analysis is extended to include the effects of mutual coupling between realizable elements by using an approach based on the array embedded element patterns.

To perform the new simulations, a two-step process has been proposed. Firstly, the un-modified electromagnetic scattering characteristics of the elements of the array were obtained using CST Microwave Studio [**84**], a full wave electromagnetic simulator. Next, the CST Microwave Studio generated element scattering patterns were used in a modified formulation of **Eq.3.3** to calculate the harmonic patterns generated when the array is time-switched.

4.3.1 Simulations of TMRA in CST and Matlab

Referring to the element switching sequence shown in **Fig.3.3**, only one of the 8 elements of the array is energised at any instant. Hence, during a given switching period, the array can only be in one of eight possible states (1 element scattering and 7 elements non-scattering). Each of these 8 states will produce an individual scattering power pattern, which corresponds to the embedded, or immersed, element pattern. CST Microwave Studio was used to calculate the embedded element scattering patterns.

In the CST model shown in **Fig.4.8**, a plane wave is illuminating at the broadside of the TMRA. The TMRA consists of bowtie dipole scattering elements with PIN diode equivalent circuits loaded at the centre of each scatterer. The PIN diode equivalent

circuits are set to low impedance and high impedance to represent biased and zero-biased states respectively. As a result of such procedure, 8 embedded element scattering patterns were generated. These patterns, Et_i, not only include the effects of mutual coupling, but also contain both amplitude and phase information relating to their spatial position.

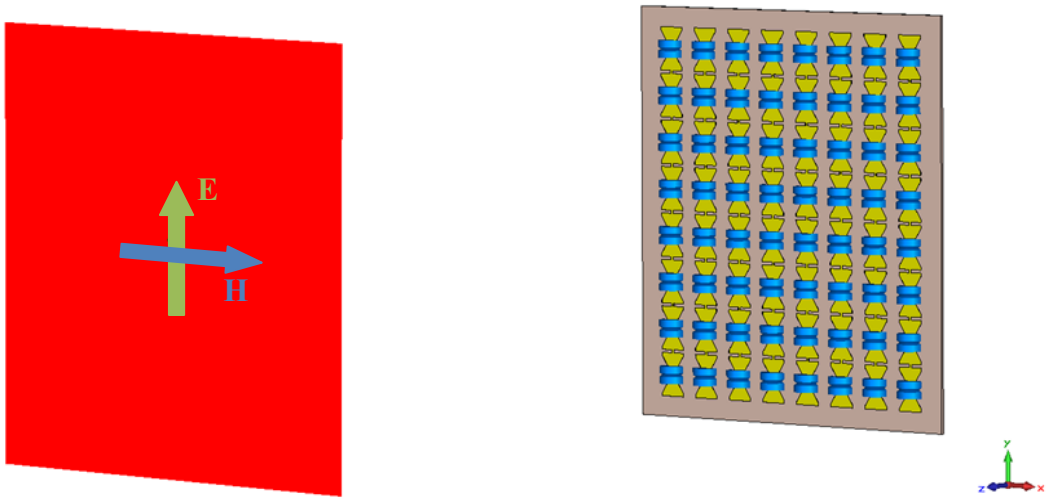

Fig.4.8 TMRA simulated in CST Microwave studio. A plane wave is illuminating the TMRA in the broadside direction.

$$E_{t_i}(\theta) = E_i(\theta)\, exp\left(j\frac{2\pi}{\lambda_c}d_i sin\theta\right) + mutual\ coupling \qquad \textbf{Eq.4.1}$$

Hence, under such conditions, a modified version of **Eq.3.8** can give the far-field scattering pattern of the bowtie dipole TMRA at any harmonic *m*

$$F_m(\theta) = \sum_i^N E_{t_i}(\theta) s_{im} \qquad \textbf{Eq.4.2}$$

where s_{im} is solved using **Eq.3.10**. Using **Eq.4.2**, the obtained embedded scattering patterns were then calculated in Matlab. Shown in **Fig. 4.9**, the results were based on the CST predicted scattering pattern from the TMRA with PIN diode-controlled bowtie elements. Only the first three positive harmonic frequencies are shown in the figure. The scattering patterns are normalised to the maximum scattering power of a TMRA size (139mm x147mm) copper plate simulated using CST under the same conditions. In its present configuration the TMRA is very inefficient in terms of gain. Most of the energy

radiated from the feed antenna would passes through the array as only one of the eight sub-arrays is scattering at any one time (this gives a theoretical, first order, reduction in gain of approximately 9dB compared to that of fully energized array). Chapter 7 provide

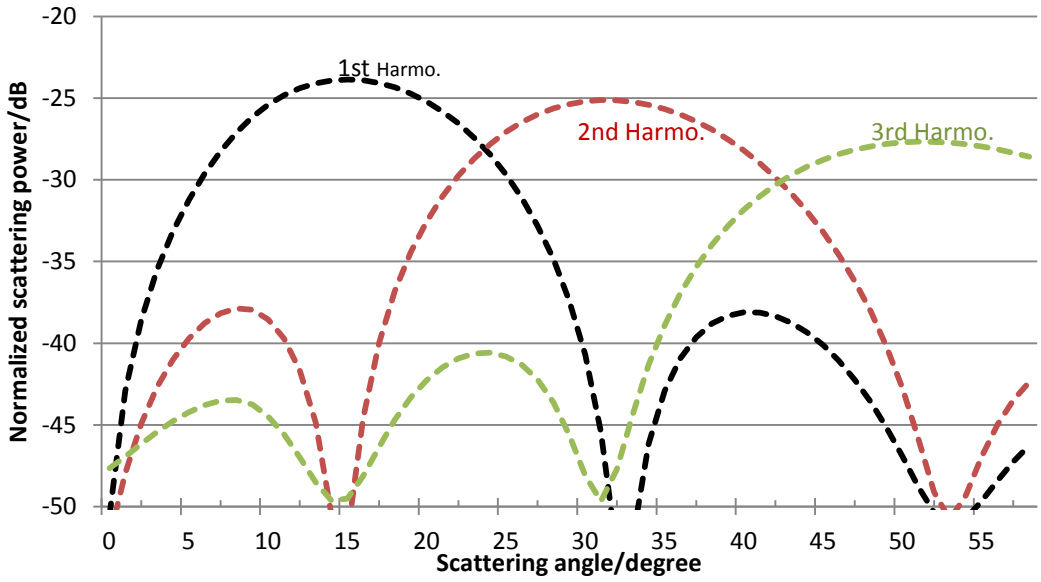

Fig.4.9 Simulated harmonic scattering patterns for the TMRA based on ideal switching time waveform.

a detailed solution to increase the TMRA efficiency. However, this part of thesis aims to demonstrate the first hardware implementation of a TMRA and to verify the operation experimentally. The results in **Fig.4.9** shows that the bowtie dipole TMRA steered the beams of the first three positive harmonic frequency to the angles of 16°, 30° and 50° respectively, which agrees with the theoretical results obtained from array factor and Fourier series shown in **Fig.3.4**.

4.3.2 Measurement

The experimental TMRA was measured in modified Naval Research Laboratory (NRL) arch, as shown in **Fig.4.10** and **Fig.4.11.** The NRL arch is standard reflectivity measurement system, which uses a pair of transmitting (Tx) and receiving (Rx) X-band horn antennas to measure the scattered field from an object. The horn antennas

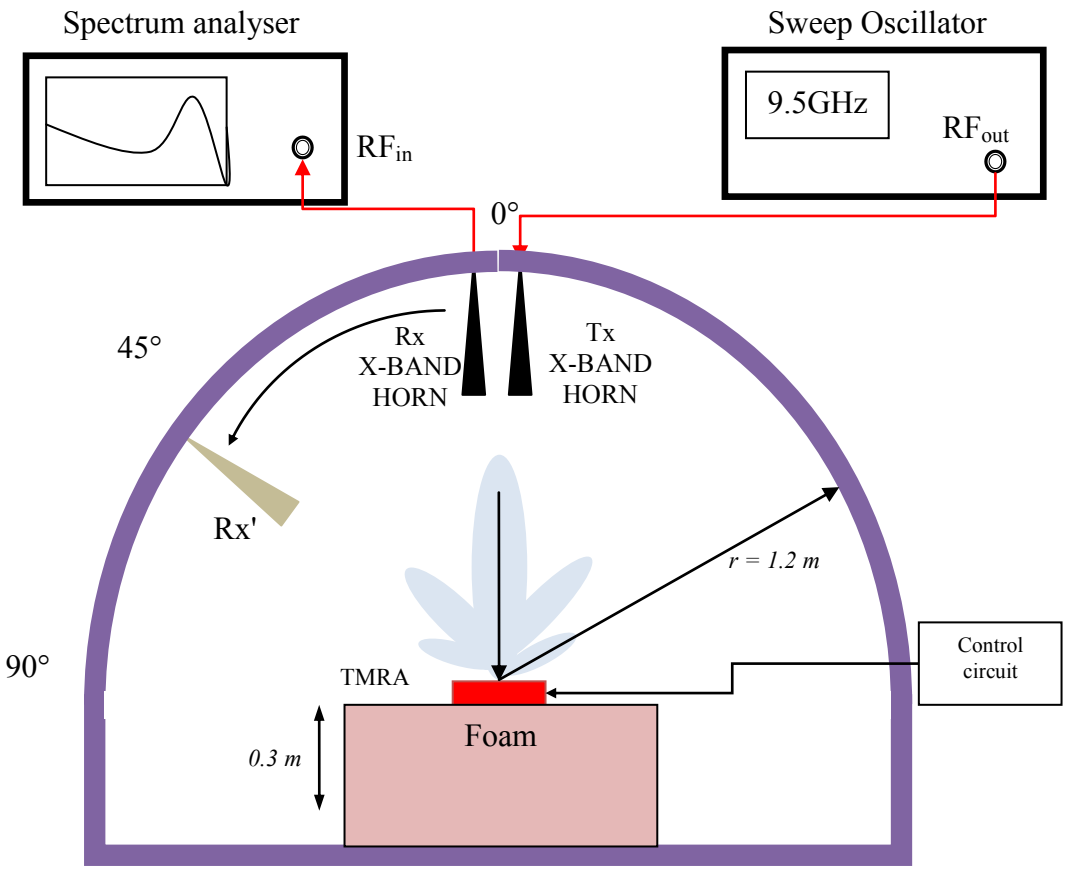

Fig.4.10 Measurement system: NRL reflectivity measurement system

have a XR-90 waveguide port with a 10 cm square aperture and 18 cm cone-to-apex length. In the modified set-up, the Tx horn antenna is used as a fixed feed antenna to illuminate the TMRA. A Hewlett-Packard 8350B was used to provide the illuminating signal at a fixed, CW, frequency of a 9.5 GHz. To record the field scattered by the TMRA, the Rx antenna was connected to spectrum analyser. The Rx antenna was manually moved from the 0° (broadside of TMRA) to 60° in steps of 1° and the magnitudes of first three harmonic frequencies were recorded when the TMRA was modulated by the control system with the sequence shown in **Fig.3.3**.

The measured radiation patterns produced by the TMRA at the first three positive harmonic frequencies are shown as solid lines in **Fig.4.12**. All traces are normalized to the scattering power of a TMRA size copper plate simulated/measured in the same

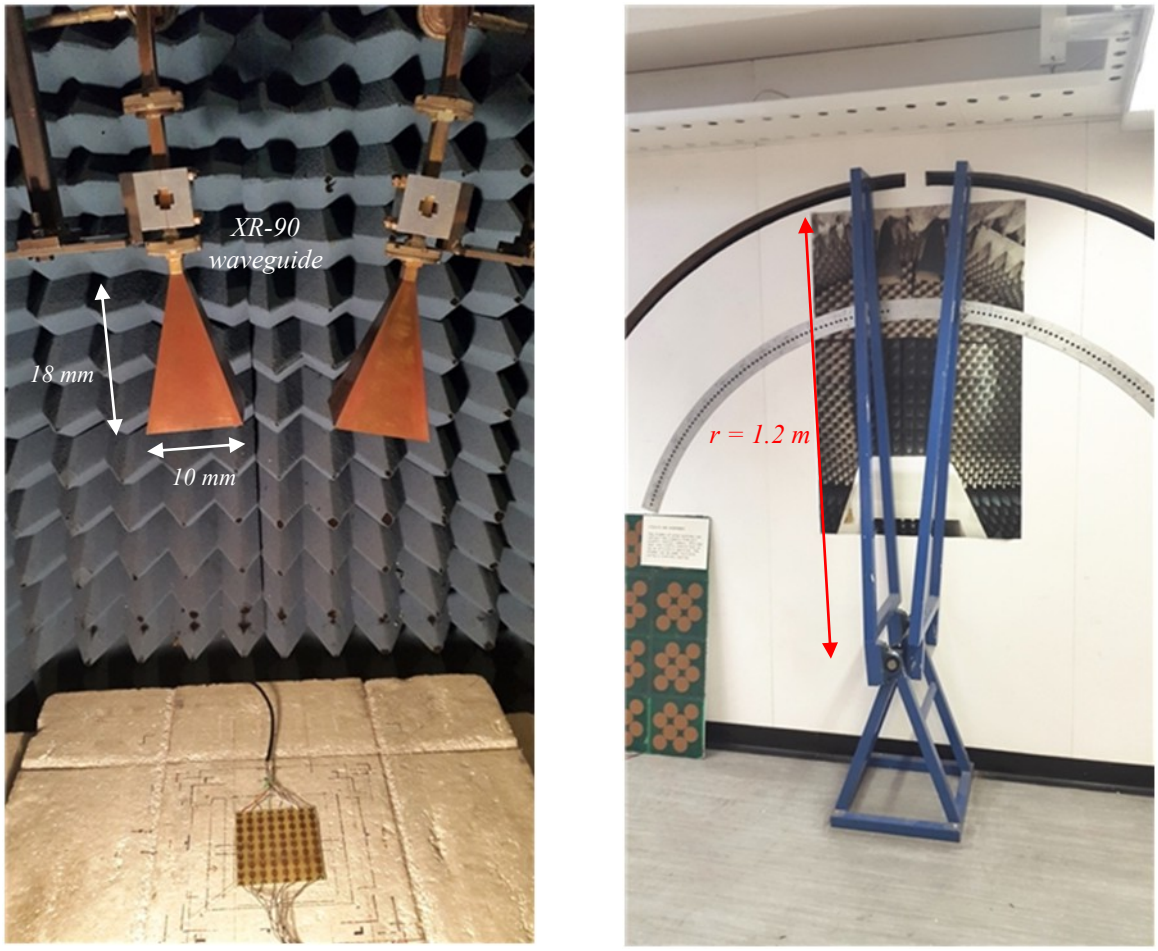

Fig.4.11 Photos of the experiemental system (ARCH): inside and outside of the anechoic chamber

conditions. Compared with the simulated results, the measured results exhibit the general characteristics of beam steering as predicted by the full-wave simulations. The most significant difference between the measured and simulated harmonic patterns is the increase in the magnitude of the first harmonic pattern. The two primary causes of the differences between the simulated and measured patterns were thought to be: a) the non-ideal pulse modulation of the diodes in the experimental system and b) the approximate PIN diode model used in the CST predictions. Based on previous experience with PIN diode models [**79**], the dominant factor causing the discrepancies between the theoretical and measured harmonic levels is thought to be the non-ideal modulation of the array elements. Although the predictions shown in **Fig.4.12** were based on the array embedded

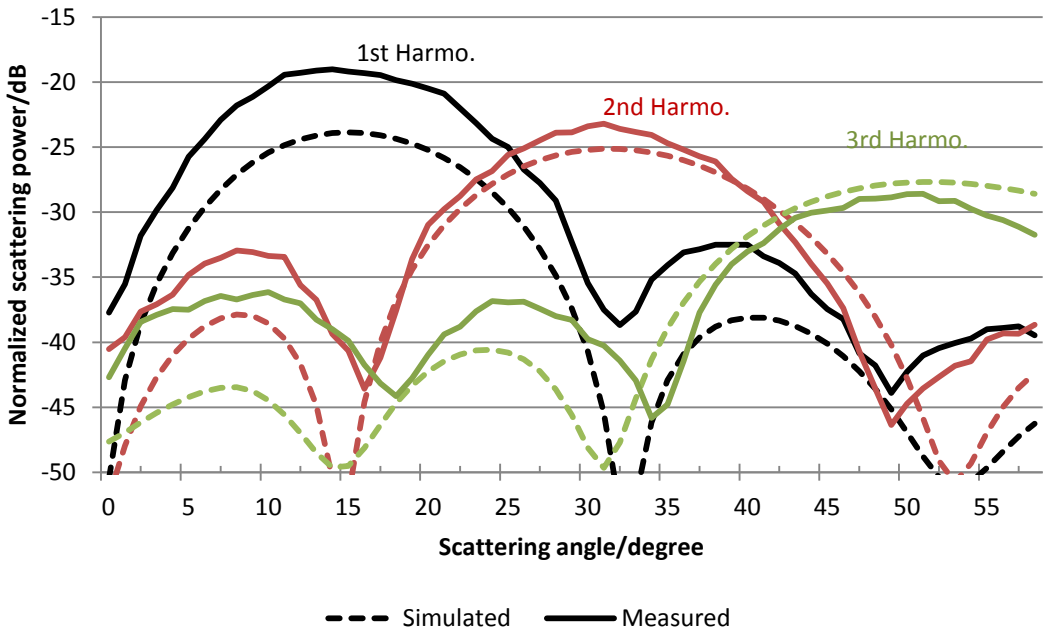

Fig.4.12 Measured and simulated harmonic scattering patterns of the bowtie dipole TMRAs based on ideal square wave modulation.

element patterns calculated using CST, the actual harmonic patterns were calculated using **Eq.4.2** in which an ideal, rectangular switching waveform is assumed. In practice this is not the case as the PIN-diodes present a reactive and non-linear load impedance to the amplifiers of the driving circuitry. As a consequence the pulse shape controlling the PIN diodes is no longer rectangular, but is distorted into a pulse with significant rise and fall times. It is easily shown using a Fourier series expansion that a non-rectangular switching waveform will produce a spectrum of harmonic components with smaller magnitudes than that of a rectangular switching waveform.

An oscilloscope was used to measure the time waveform applied to TMRA and shown in **Fig.4.13**. The rise time is $t_a = 0.32$ μs but the PIN diode takes 3.6 μs to stabilize in OFF mode, which is significantly large compared to a full duty cycle of 8 μs. This was caused by the process of charges diffusing in the I-layer [**82**].

The scattering pattern of the TMRA based on the measured time waveform was simulated using Matlab and a Fourier series expansion of the measured modulating

waveform. The simulated and measured scattering patterns are shown in **Fig.4.14**. All traces are normalized to the scattering power of a TMRA size copper plate simulated/ measured under the same conditions. The modified simulations show close agreement with the measured patterns in terms of magnitude. The beam directions of each harmonic are located at angles of 16°, 32° and 48° respectively.

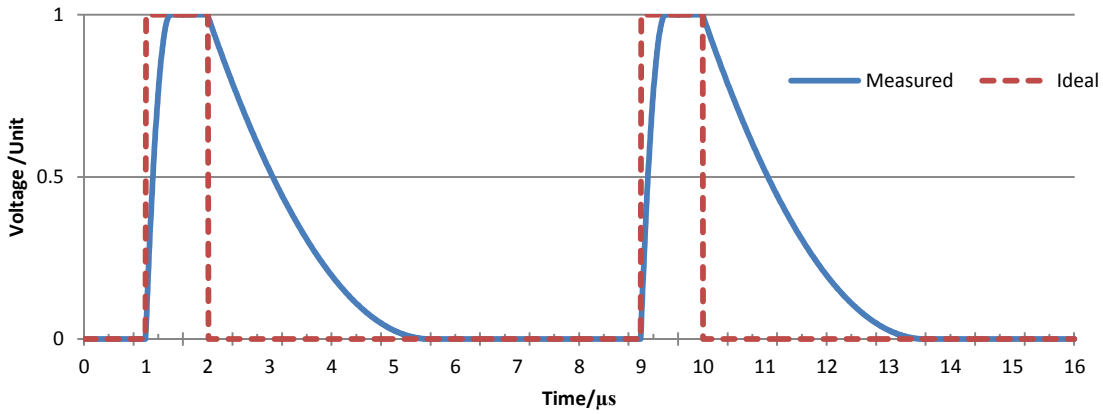

Fig.4.13 The ideal and realistic time wave forms applied to the TMRA. Measured wave forms have a rise time of 0.32 μs and fall/recover time of 3.6 μs.

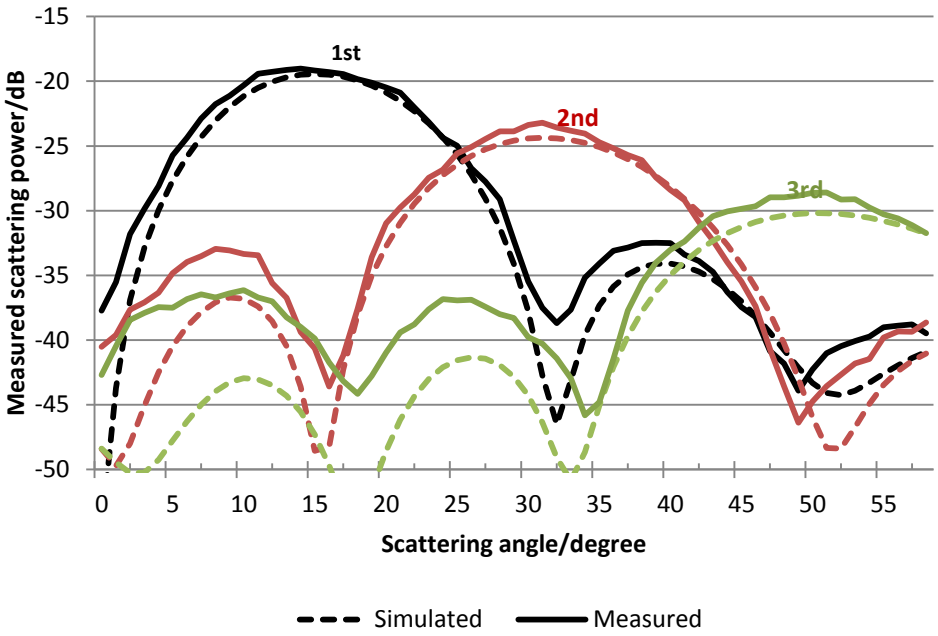

Fig.4.14 Measured and simulated harmonic scattering patterns of the bowtie dipole TMRA based on a measured time waveform.

4.4 Conclusion

A time-modulated reflector array (TMRA) has been described, analyzed and demonstrated experimentally. The experimental TMRA was based on an array of PIN diode controlled bowtie dipole elements. The TMRA system was designed, constructed and simulated in a commercial full-wave electromagnetic simulator. Moreover, the bowtie dipole TMRA prototype was made to measure in a modified version of a NRL reflectivity measurement system. Measured data from the experimental TMRA confirms the operation of the system. The prototype can conduct a harmonic beam steering and locate the first three harmonic beams at the directions of 16°, 32° and 48° respectively.

The bowtie dipole TMRA is inefficient in power, which is due to its special ON/OFF scattering configuration. A good solution is to add a back plane to 'pick up' the wasted energy when an element is OFF. A full description of the efficiency-improved TMRA is discussed in Chapter 7. More importantly, the purpose of this chapter is to introduce the first experimental TMRA based on bowtie dipole elements. The required beam steering function was successively realized in the simple low cost TMRA prototype. TMRA can potentially lower the price of the applications, which require antenna beam management.

Chapter 5 BEAMFORMING APPLIED TO TMRA

5.1 Introduction

Beamforming is a signal processing algorithm, which aims to generate a desired beam focused on the target direction and minimized at interferences directions. Beamforming can be categorized into two groups: static beamforming and adaptive beamforming. Static beamforming are used when the target locations and the wave directions are known. The static beamformers are pre-calculated and normally fixed or only switchable between limited sets. In contrast, adaptive beamforming is a dynamic process, which combines the information of all the signal received by the array to filter out the interferences and maximize the wanted signal. As the name suggests, an adaptive beamformer can adapt the formed beam to different situations. This chapter introduces two adaptive beamforming schemes to the TMRA: minimum variance distortionless response (MVDR) beamformer and linearly constrained minimum variance (LCMV) beamformer. These two beamformers have gained the researchers' interests as the beamforming techniques for the next generation wireless mobile communications [**85**] [**86**]. They are able to adapt the formed pattern to track or predicate the change of incoming wave directions using optimization algorithms [**87**] [**88**].

This chapter applies MVDR and LCMV beamforming to a TMRA. Part of the results have been reported in my research contributions [**89**] [**90**]. The concepts of MVDR and LCMV beamforming are introduced with an example of their application in a conventional phased array. A simple example of an 8-element linear TMRA conducting MVDR/LCMV beamforming is analysed using Fourier series and array-factor theory. The switching sequence applied to the TMRA is derived from a MVDR/LCMV algorithm

to produce a prescribed scattering pattern at harmonic frequencies. The beamforming performance of a theoretical TMRA model consisting of switchable elements is compared to that of a conventional phased array with phase shifters. An example of TMRA based on bowtie dipole design has been constructed and simulated using full-wave simulator to show adaptive nulling at harmonic frequencies. Compared to the conventional phased array system, TMRA aims to perform MVDR and LCMV beamforming with less cost and simpler system implementation.

5.2 MVDR beamforming

5.2.1 Description of MVDR beamforming

Minimum Variance Distortionless Response (MVDR) approach is popular in array signal processing, particular in beamforming [**91**]. It was first proposed by Capon in 1969 [**92**]. The idea of MVDR beamforming is to combine elements in an array to retain the power levels on desired signals while minimize the total output power [**62**]. In the other word, MVDR calculates a vector weights matrix **w** to determine a good estimation on the desired signal or direction but minimize the total output power level $\boldsymbol{Y}(\boldsymbol{\omega})$. Assuming the number of planewave signals received at the array is P and the number of array elements is M, the received signals $\boldsymbol{X}(\boldsymbol{\omega})$ at the antenna array in frequency-domain consists of signals and noise is [**62**]

$$\boldsymbol{X}(\boldsymbol{\omega}) = \boldsymbol{F}(\boldsymbol{\omega})\boldsymbol{d} + \boldsymbol{N}(\boldsymbol{\omega}) \qquad \textbf{Eq.5.1}$$

where $\boldsymbol{N}(\boldsymbol{\omega})$ is zero-mean Gaussian noise, $F(\omega)$ is the frequency-domain snapshot of received signals and $\boldsymbol{d}$ is an $M \times P$ array manifold matrix,

$$\boldsymbol{F}(\boldsymbol{\omega}) = \begin{bmatrix} F_1(\omega_1) & F_2(\omega_2) & \dots & F_P(\omega_p) \end{bmatrix}^T \qquad \textbf{Eq.5.2}$$

and

$$\boldsymbol{d} = \begin{bmatrix} a_1(\omega_1)e^{-jk_1d_1sin\theta} & \dots & a_1(\omega_p)e^{-jk_pd_1sin\theta} \\ \vdots & \ddots & \vdots \\ a_M(\omega_1)e^{-jk_1d_Msin\theta} & \dots & a_M(\omega_p)e^{-jk_pd_{M1}sin\theta} \end{bmatrix} \quad \textbf{Eq.5.3}$$

or

$$\boldsymbol{d} = [\boldsymbol{d}(\boldsymbol{\omega}: \boldsymbol{k_1}) \;\; \boldsymbol{d}(\boldsymbol{\omega_2}: \boldsymbol{k_2}) \;\dots\; \boldsymbol{d}(\boldsymbol{\omega_p}: \boldsymbol{k_P})]$$

Assume that $F_1(\omega)$ is the signal of desired dircetion, ω_p is the angular frequency of the p-th signal and $\boldsymbol{d}(\omega_1: k_1)$ is the manifold matrix of signal $F_1(\omega)$,

$$\boldsymbol{d}(\omega_1: k_1) = [a_1(\omega_1)e^{-jk_1d_1sin\theta}, \dots, a_M(\omega_1)e^{-jk_1d_Msin\theta}]^T \quad \textbf{Eq.5.4}$$

where $a_M(\omega_p)$ is scattering pattern of M-th element at frequency of ω_p and d_M is the position of *M-th* element, while θ is the direction of received signal/jammer and k_i is the wavenumber,

$$k_i = \frac{2\pi}{\lambda_i} \quad \textbf{Eq.5.5}$$

where λ_i is wavelength of *i-th* signal operating frequency.

Let the weights factor be $\boldsymbol{w}$, which is the solution to minize output signal $\boldsymbol{Y}(\boldsymbol{\omega}) = \boldsymbol{w^H X}(\boldsymbol{\omega})$ and retain the no-distortion desired signal power $F_1(\omega)$. The numerical model of such optimisation problem is [**62**]

$$min_w \, \boldsymbol{w^H S w} \quad s.t. \; \boldsymbol{w^H d}(\omega_1: k_1) = \boldsymbol{1} \quad \textbf{Eq.5.6}$$

where **S** is covariance matrix of received signal

$$\boldsymbol{S} = \boldsymbol{E}[\boldsymbol{X}(\boldsymbol{\omega})\boldsymbol{X^H}(\boldsymbol{\omega})] \quad \textbf{Eq.5.7}$$

The optimum distortionless beamformer for **Eq.5.6** is

$$\boldsymbol{w} = \frac{\boldsymbol{S^{-1}d}(\omega_1: k_1)}{\boldsymbol{d}(\omega_1: k_1)^{\boldsymbol{H}}\boldsymbol{S^{-1}d}(\omega_1: k_1)} \quad \textbf{Eq.5.8}$$

An example of MVDR beamforming operating on a phased array is given. **Fig.5.1** shows a picture of a phased array system, which is configured to identify a desired signal from jammers and noise in free space. We assume an 8 element linear phased array is expecting 1 signal and 3 jammers shown in **Table II**. All four signals are assumed to operate at the phased array frequency where their wave numbers k_i are identical. The

Table II DESIRED SIGNAL AND JAMMERS IN FREE SPACE

	S (Desired)	J_1 (Jammer)	J_2 (Jammer)	J_3 (Jammer)
Direction (Degree)	15	25	0	-15
SNR/JNR (dB)	0	30	30	30

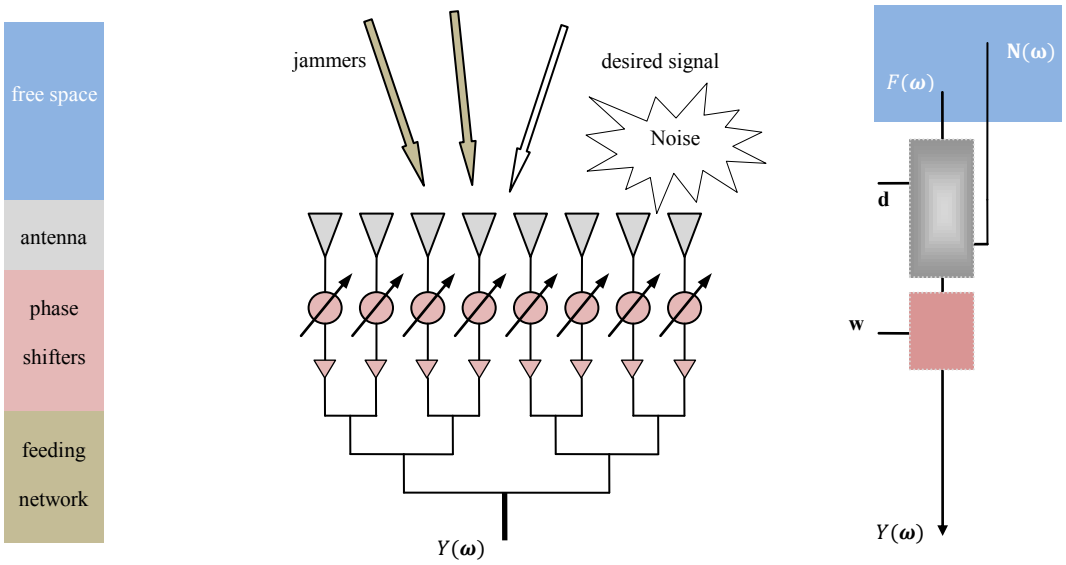

Fig.5.1 Model of phased array, which consists of antennas, phase shifter amplifiers, and feeding network.

distance between elements is half-wavelength of operating frequency. Antenna elements are identical to each other and have isotropic radiation patterns. MVDR beamforming can form a radiation pattern with the main beam points to the direction of source but nulls locate at the directions of jammers. Using **Eq.5.8**, the calculated weighting $\boldsymbol{w}$ was applied to the array using phase shifters and low noise amplifiers (LNA). **Fig.5.2** shows the calculated directive radiation pattern of the 8-element phased array based on MVDR beamforming. The formed pattern meets the prescribed specifications in **Table II**. The main beam is located at 15° and nulls are pointed to the interferences directions at -15°, 0° and 25°.

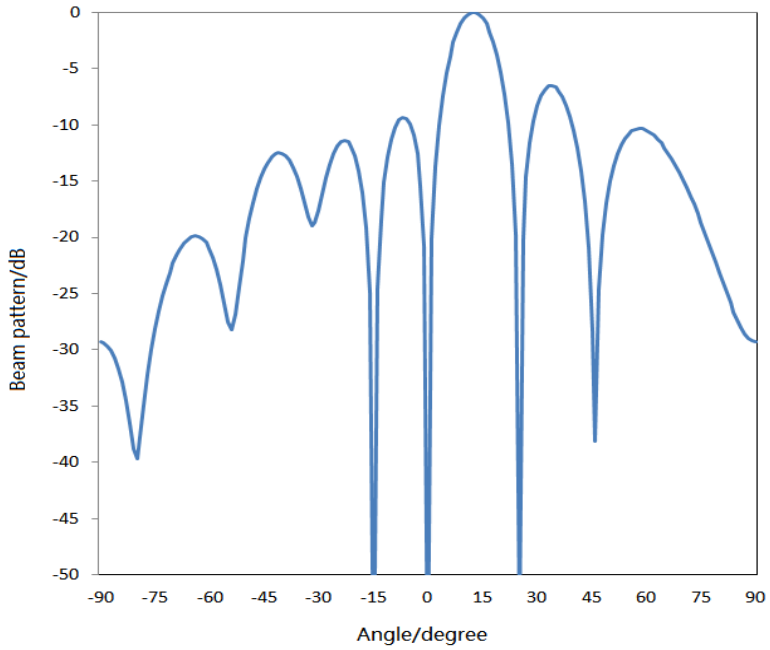

Fig.5.2 Scattering pattern of conventional phased array based on MVDR algorithm and isotropic element patterns.

5.2.2 MVDR beamforming applied to an ideal TMRA

Now consider a simple example of an 8 element time modulated reflector array shown in **Fig.5.3**. The elements are assumed to be able to switch between fully scattering and non-scattering states. The scattering pattern of the TMRA elements were assumed to be an identical isotropic pattern. Neither realistic element scattering pattern nor the mutual coupling between elements were considered in this estimation. The receiving antenna was placed in the farfield of the reflector array so that reflector elements have the same distance to the feeding antenna. The distances between elements are half wavelength of the illuminating frequency. The elements are assumed to scatter isotropically. The TMRA is expecting one desired signal at 15° and three jammers at -15°, 0° and 25° respectively in **Table II**, identical to the scenario in previous phased array. Instead of expensive phase shifters used in conventional phased array, the pre-calculated MVDR weights are applying using switchable elements. **Eq.5.8** is used to determine the

MVDR weights, which aim to form a directive beam pattern at 1st harmonic frequency of the TMRA. The time sequence is calculated using a modified version of **Eq.3.6** given as

$$\tau_{ion} = \frac{1}{2}\left[\frac{1}{\pi m} phase(w_i) - \frac{1}{\pi m}\text{asin}(\pi m|w_i|)\right]$$

$$\tau_{ioff} = \frac{1}{2}\left[\frac{1}{\pi m} phase(w_i) + \frac{1}{\pi m}\text{asin}(\pi m|w_i|)\right] \qquad \textbf{Eq.5.9}$$

where m the harmonic number. Assuming the desired beam pattern form at the first positive harmonic frequency (m = 1), **Eq.5.9** can covert the weight matrix **w** obtained **Fig.5.4**. The array elements were energised periodically according to that time-switching sequence. Using **Eq.3.3**, the obtained beam pattern at the first positive harmonic from **Eq.5.8** to time sequence τ_{ion} and τ_{ioff}. The obtained time sequence is shown in frequency is shown in **Fig.5.5**, which is identical to that of example of phased array. The result shows that the desired beamforming is achieved and the power pattern is identical to that obtained from a conventional phased array controlled by phase shifters.

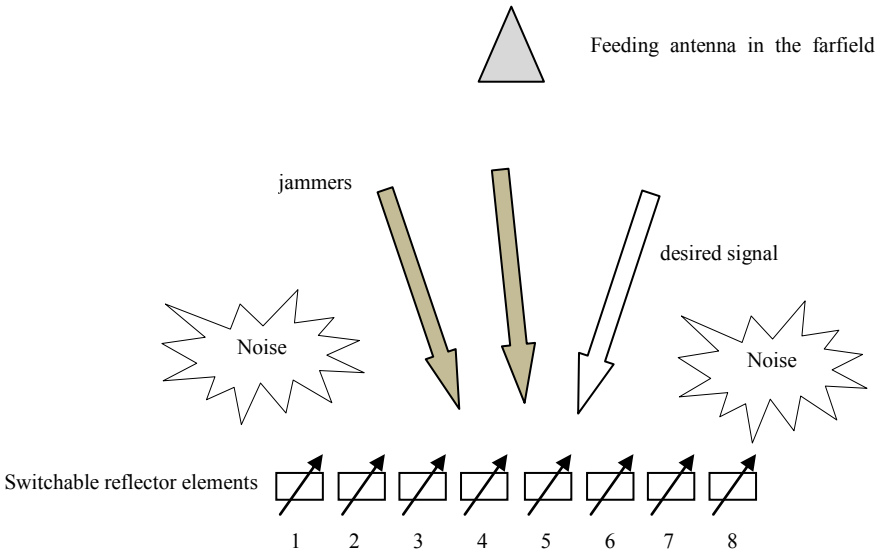

Fig.5.3 Model of an 8 element TMRA, which is fed in the centre of the array by a farfield source.

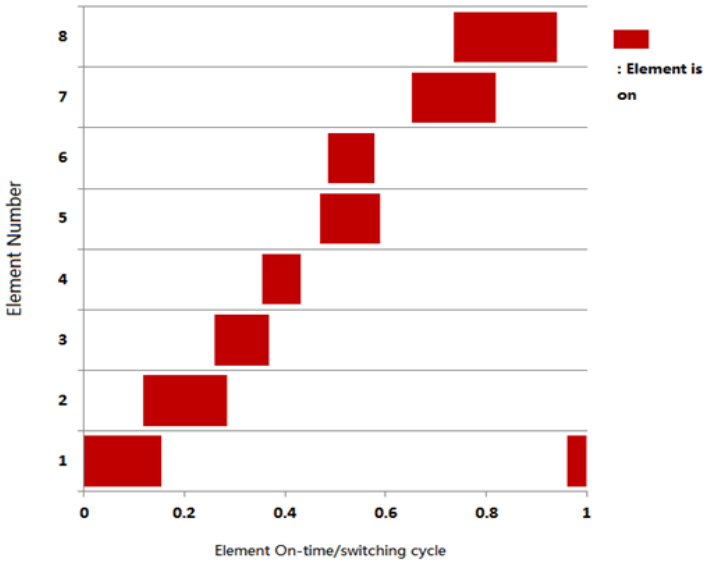

Fig.5.4 TMRA element switching sequence based on MVDR beamforming.

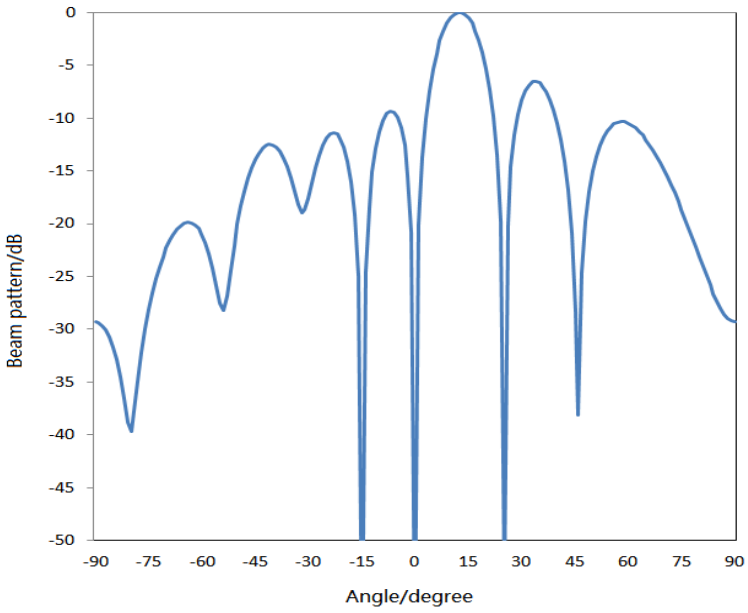

Fig.5.5 Scattering pattern of TMRA at 1st harmonic frequency based on MVDR algorithm and isotropic element patterns.

5.2.3 MVDR beamforming applied to the bowtie dipole TMRA

The part of thesis demonstrates the MVDR beamforming applying to a more realistic TMRA based on bowtie dipole elements. The bowtie dipole TMRA system is

identical to the one practicing the beam steering function shown in **Fig.4.8**. The physical configuration of the TMRA can be found in Chapter 4.

To analyse the performance of the dipole array in a TMRA system, a two-step procedure was performed. Firstly the scattering properties of the array were modelled using the full wave electromagnetic simulation tool, CST Microwave Studio. Secondly, the scattering patterns generated from CST were used in a Fourier series expansion to calculate the harmonic patterns due to time-switching the array.

The eight sub-arrays are controlled by 8 individual switching signals. Similar to the process in Chapter 4, CST Microwave Studio are employed to calculated the realistic embedded element patterns. That means CST will generate 8 embedded pattern to represent the individual scattering patterns of the 8 sub-arrays. Each of the individual pattern is recorded when one of sub-array is ON and rest of them are OFF. In the CST model, the PIN diodes were modelled by lumped equivalent circuits to represent the biased (ON) and zero-biased (OFF) element states. The results of this procedure are 8 individual embedded element scattering patterns, $E_{t1}(\theta)$ to $E_{t8}(\theta)$ which include effects of the scattering pattern and array factor. In the ideal model, presume the elements are presumed to be isotropic and have identical unit magnitude scattering patterns. However, such assumptions do not apply neither in the bowtie TMRA because of existing of non-isotropic element and inter-element coupling. CST simulations will tells us the realistic scattering pattern with inter-element coupling.

Consider the obtained embedded patterns as prior knowledge, which can improve estimating the incoming signals' power in **Eq.5.1**. As the patterns $Et_i(\theta)$ inherently contain both amplitude and phase information relating to their spatial position, **Eq.5.1** is modified accordingly to give the following expression,

$$\boldsymbol{X(\omega)} = F_1(\omega)\boldsymbol{E_t}(\theta_1) + \boldsymbol{J(\omega)}\boldsymbol{E_t}(\boldsymbol{\theta}) + \boldsymbol{N(\omega)} \qquad \textbf{Eq.5.10}$$

where the manifold matrix $\mathbf{d}(\boldsymbol{\theta})$ are replaced by the pattern matrix $\boldsymbol{E_t}(\theta)$. θ_1 and matrix $\boldsymbol{\theta}$ are the directions of the desired signal and jammers respectively. $F_1(\omega)$ is the frequency domain snapshot of the desired signals and $\boldsymbol{J(\omega)}$ is the frequency domain snapshot matrix of the jammers. Given the prior information, the weight **w** of new estimation of **X(ω)** is calculated in a modified version of **Eq.4.8** .

$$\boldsymbol{w} = \frac{\boldsymbol{S^{-1}E_t}(\theta_s)}{\boldsymbol{E_t}(\theta_s)^{\boldsymbol{H}}\boldsymbol{S^{-1}E_t}(\theta_s)} \qquad \textbf{Eq.5.11}$$

where **S** is the covariance matrix of the new received signals **X(ω)** in **Eq.5.10.**

The desired beam pattern is designed to be formed at the 1st positive harmonic frequency (m = 1). Given the weight matrix **w**, the time switching sequence was re-calculated using **Eq.5.9** and shown in **Fig.5.6**. The time sequence is then used to calculate the time-switched performance of the array in the Fourier expansion **Eq.3.3**. As the patterns inherently contain both amplitude and phase information relating to their spatial position, **Eq.3.3** is modified accordingly to give the following expression

$$F_m(\theta) = \sum_{i}^{N} E_{t_i}(\theta) s_{im} \qquad \textbf{Eq.5.12}$$

where s_{im} (see **Eq.3.4**) is the Fourier series coefficients of the periodical modulating signal $I_i(t)$.

Fig.5.7 shows the normalized scattering pattern of the TMRA at the 1st positive harmonic frequency based on CST predicated embedded element patterns. Comparing these data to those obtained from of the ideal isotropic model in **Fig.5.5**, shows that the bowtie dipole design produces a similar response to that predicted from array-factor theory and exhibits the desired adaptive beamforming characteristics.

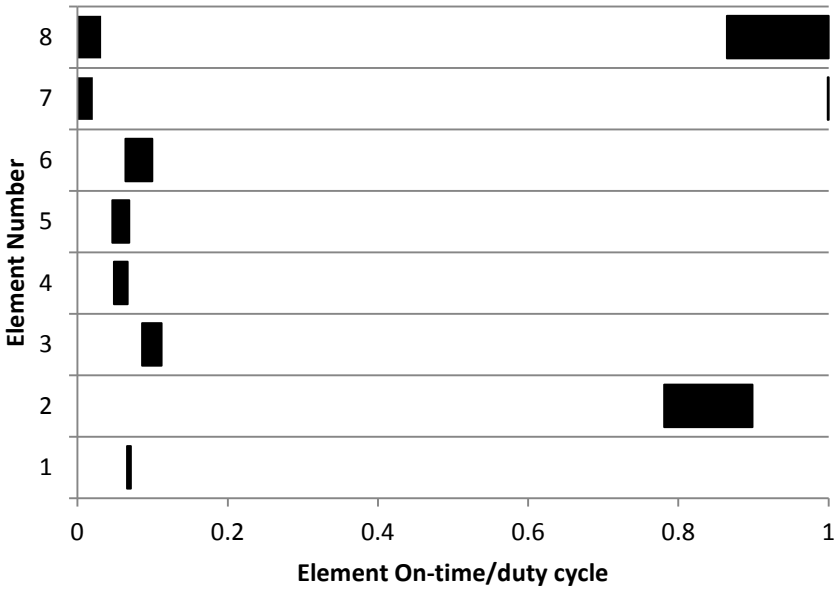

Fig.5.6 TMRA element switching sequence based on MVDR beamforming and simulated embedded patterns.

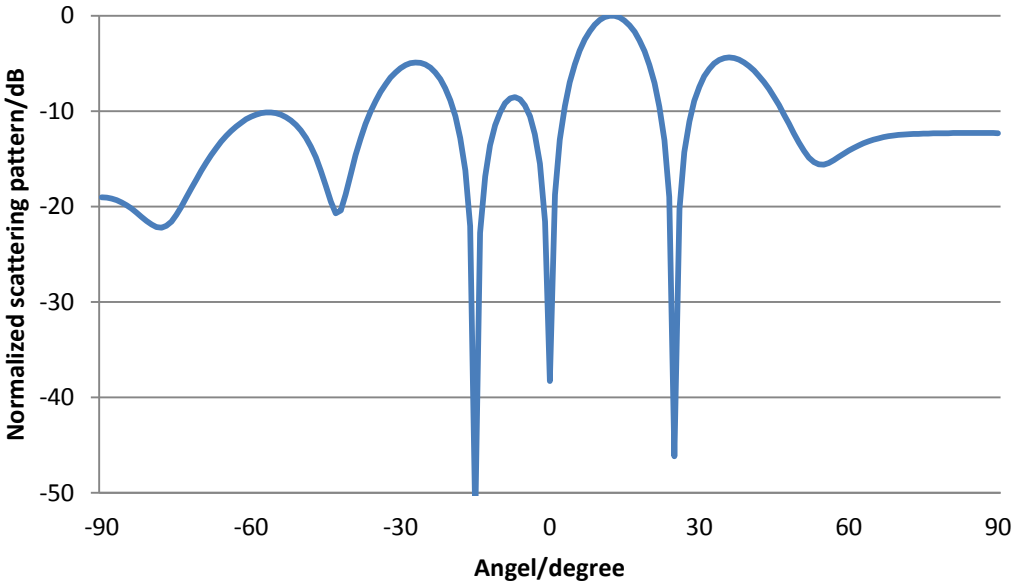

Fig.5.7 Simulated beam patterns for the TMRA at the 1st positive harmonic frequency based on the simulated embedded element pattern and MVDR beamforming

5.3 LCMV beamforming

5.3.1 Concept of LCMV beamforming

LCMV beamforming and MVDR beamforming shares a common approach to minimize the array total output power. The difference is the number of constrains of the two algorithms. MVDR calculates a vector weights matrix $\boldsymbol{w}$ to determine a fixed estimation on a single signal. However, LCMV beamforming is able to retain a desired response for the multiple signals (can be one or more constrains). Assuming the number of array elements is *M*, the received signals $\boldsymbol{X(\omega)}$ at the antenna array in the frequency-domain is same as the model of MVDR beamforming [**93**],

$$\boldsymbol{X(\omega) = F(\omega)d + N(\omega)} \qquad \textbf{Eq.5.13}$$

where $\boldsymbol{X(\omega)}$ consists of signals and noise. Instead of one objective, the vector weights matrix $\boldsymbol{w}$ can retain a fixed response in multiple objectives while minizing mean square of output signal $= \boldsymbol{w^H X}$. The numerical model is [**93**],

$$\min_{w} \boldsymbol{w^H R_X w} \quad s.t.\ \boldsymbol{w^H C = f} \qquad \textbf{Eq.5.14}$$

where $\boldsymbol{R_X}$ is covariance matrix of received signal

$$\boldsymbol{R_X = E[X(\omega)X^H(\omega)]} \qquad \textbf{Eq.5.15}$$

and $\boldsymbol{C}$ is the matrix of constraints and $\boldsymbol{f}$ is the response vector. The corresponding weight vector $\boldsymbol{w}$ for **Eq.5.14** is

$$\boldsymbol{w = \frac{R_X{}^{-1}C}{C^H R_X{}^{-1}C} f} \qquad \textbf{Eq.5.16}$$

Next, and for puposes of comparison, a conventional phased array conducting an LCMV beamforming is introduced. The phased array consists of 8 linear isotropic radiattors. The inter-element spacing is a half-wavelength at the operating frequency. The phased array is configured to identify a desired signal from in an environment, which contains both jammers and noise in. The LCMV beamforming algorithm can form a

radiation pattern in which the main beam points to the direction of the desired signal, but in which nulls are formed in the directions of the jammers. A typical approach is to consider the null constraints in the direction of jammers and a unit magnetitude constraint in the desired signal. The constraint matrix $\boldsymbol{C}$ and vector $\boldsymbol{f}$ can be constructed by combining the unit constraint and *(N-1)* null constraints and given by

$$\boldsymbol{C} = [\boldsymbol{d_s}(\theta_s), \boldsymbol{d}(\theta_1), \dots, \boldsymbol{d}(\theta_2), \boldsymbol{d}(\theta_{N-1})]$$

$$\boldsymbol{f} = \left[1, \underbrace{0, \cdots, 0,0}_{\mathrm{N-1}}\right]^{\boldsymbol{T}} \qquad \textbf{Eq.5.17}$$

Assume the phased array is expecting one desired signal and three jammers, as

Table III DESIRED SIGNAL AND JAMMERS IN FREE SPACE

	S (Desired)	J_1 (Jammer)	J_2 (Jammer)	J_3 (Jammer)
Direction (Degree)	$\theta_s = -15$	$\theta_0 = -25$	$\theta_1 = 0$	$\theta_2 = 35$
SNR/JNR (dB)	0	30	30	30

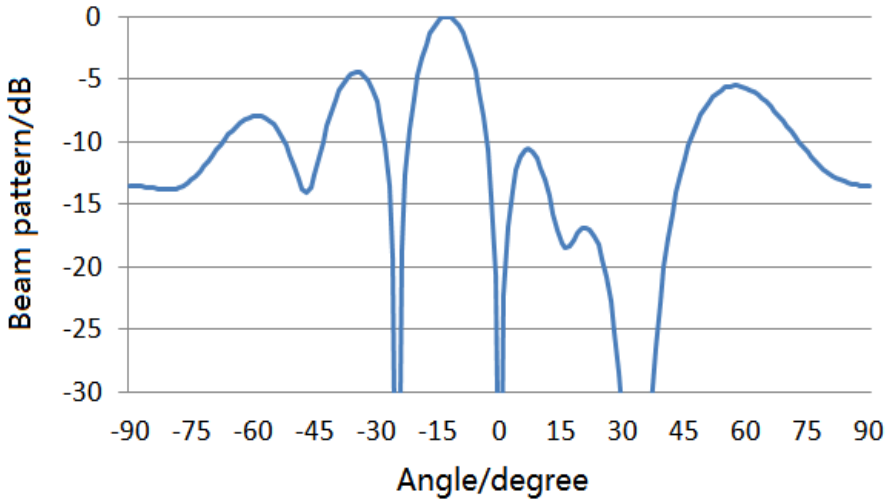

Fig.5.8 Beam pattern of conventional phased array based on LCMV algorithm and ideal isotropic element patterns.

detailed in **Table III**. Using **Eq.4.20**, the weighting $\boldsymbol{w}$ was applied to calculate the array array response and **Fig.5.8** shows the corresponding radiation pattern of which formed main beam located at -15°. At the directions of interferences (-25°, 0° and 35°), the array has a very low response (less than -30 dB compared to the desired direction). The formed pattern fulfills the specifications in **Table III**.

5.3.2 LCMV beamforming applied to ideal TMRA

Now examine a specific example of an 8 element time modulated reflector array. The signal specifications was identical to that of the conventional phased reflector array in **Table III**. Instead of phase shifters used in conventional array, pre-calculated LCMV weights are applying using switching ON/OFF time of elements. The array elements are energised according to the time-switching sequence shown in **Fig.5.9**. The time sequence in **Fig.5.9** are pre-calculated using the given LCMV weights in **Eq.4.20** and weight-time conversion formula **Eq.4.9**. The resulting formed beam pattern at the first positive harmonic frequency is shown in **Fig.5.10**. The result shows that desired beamforming is

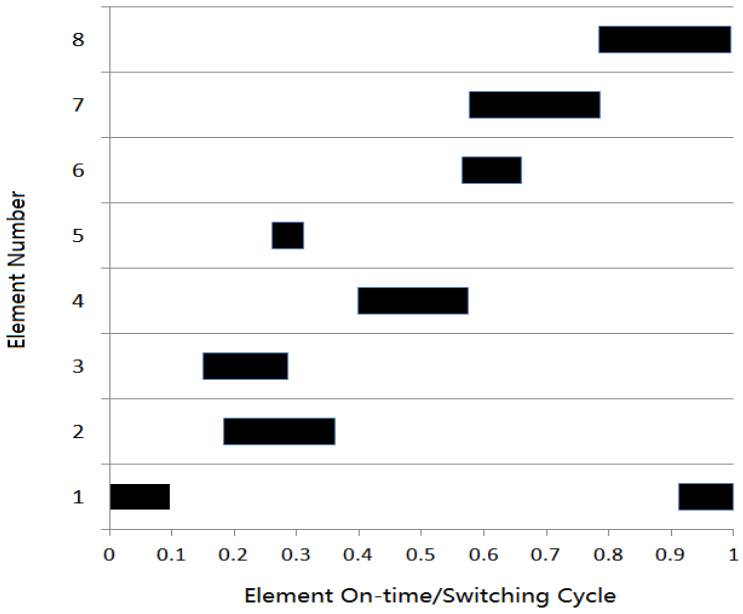

Fig.5.9 TMRA element switching sequence based on LCMV beamforming and isotropic element patterns.

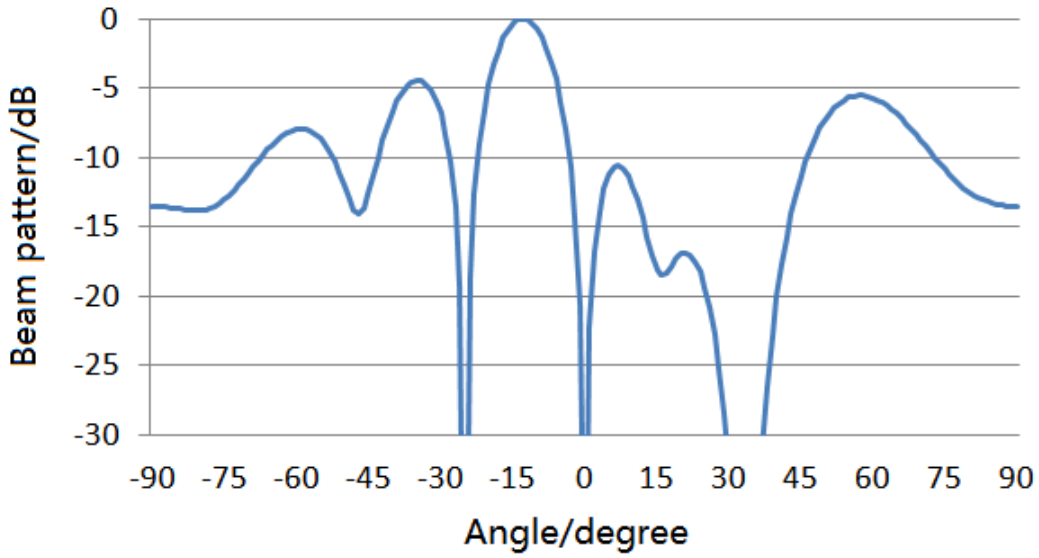

Fig.5.10 Ideal beam pattern for the TMRA at the 1st positive harmonic frequency based on isotropic element patterns, array factor and LCMV beamforming.

achieved and the power pattern is identical to that obtained from a conventional phased array controlled by phase shifters.

5.3.3 LCMV beamforming applied to realistic TMRA

Now consider an implementation of the TMRA concept using realistic elements. The process to apply LCMV beamforming to a realistic TMRA is identical to that of applying MVDR beamforming. The only difference is the way to calculate the weighting matrix. The whole process involves two steps. Firstly the scattering properties of the array were modelled using the full wave electromagnetic simulation tool, CST Microwave Studio. Secondly, the scattering patterns generated from CST MICROWAVE STUDIO were used in Fourier series analysis to calculate the harmonic patterns due to time-switching the array.

The physical specification of the TMRA array is shown in Fig.4.8, which is identical to the hardware implement of the beam steering and MVDR beamforming. Comparing to the isotropic scattering patterns assumed in ideal case, CST Microwave Studio can calculated a realistic embedded element pattern, which contains both the

effects of array factor and inter-element coupling. The eight sub-arrays are controlled by 8 individual switching signals. CST MICROWAVE STUDIO will generate 8 embedded pattern to represent the individual scattering patterns of the 8 sub-arrays. Each of the individual pattern is recorded when one of sub-array is ON and rest of them are OFF. In the CST model, the PIN diodes were modelled by lumped equivalent circuits to represent the biased (ON) and zero-biased (OFF) element states. The results of this procedure are 8 individual embedded element scattering patterns, $E_{t1}(\theta)$ to $E_{t8}(\theta)$ which include effects of the scattering pattern and array factor. We consider the obtained embedded patterns as prior knowledge, which can improve estimating the incoming signals' power in **Eq.4.10**. As the patterns $Et_i(\theta)$ inherently contain both amplitude and phase information relating to their spatial position, **Eq.4.10** is modified accordingly to give the following expression,

$$\boldsymbol{X(\omega) = F(\omega)E_t(\theta) + N(\omega)} \qquad \textbf{Eq.5.18}$$

where the manifold matrix $\mathbf{d}(\boldsymbol{\theta})$ are replaced by the pattern matrix $\boldsymbol{E_t(\theta)}$. $\boldsymbol{\theta}$ is the direction matrix of received signals. The modified $\boldsymbol{X(\omega)}$ is then used in **Eq.4.20** to calculate the weighting matrix using the specifications in **Table 4.2**. The desired beam pattern is designed to be formed at the 1st positive harmonic frequency (m = 1). Given the weight matrix **w**, the time switching sequence was re-calculated using **Eq.4.9** and shown in **Fig.5.11**. As the patterns $\boldsymbol{E_t(\theta)}$ inherently contain both amplitude and phase information relating to their spatial position, equation (10) is modified accordingly to give the following expression

$$F(\theta) = \sum_{i}^{N} E_{t_i}(\theta) s_{im} \qquad \textbf{Eq.5.19}$$

Fig.5.12 shows the CST predicted scattering pattern from the TMRA with PIN diode controlled dipole elements. Comparing these data to those obtained from of the ideal model in **Fig.5.10**, shows that the dipole design produces a similar response to that

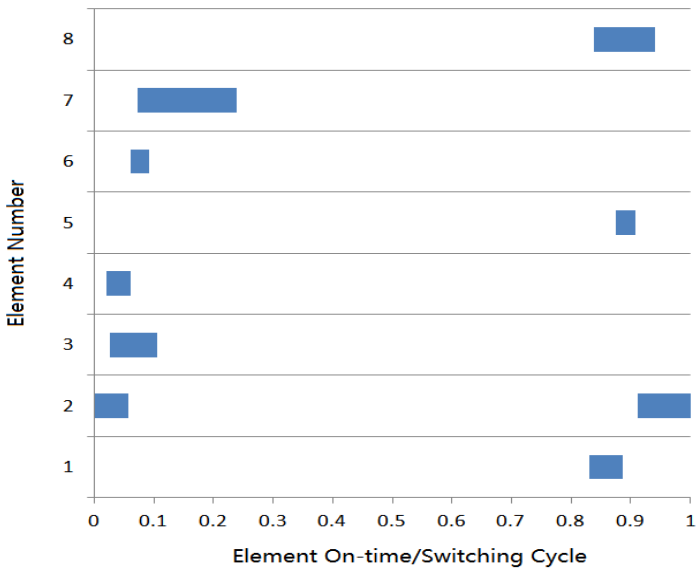

Fig.5.11 TMRA element switching sequence based on LCMV beamforming and simulated embedded patterns.

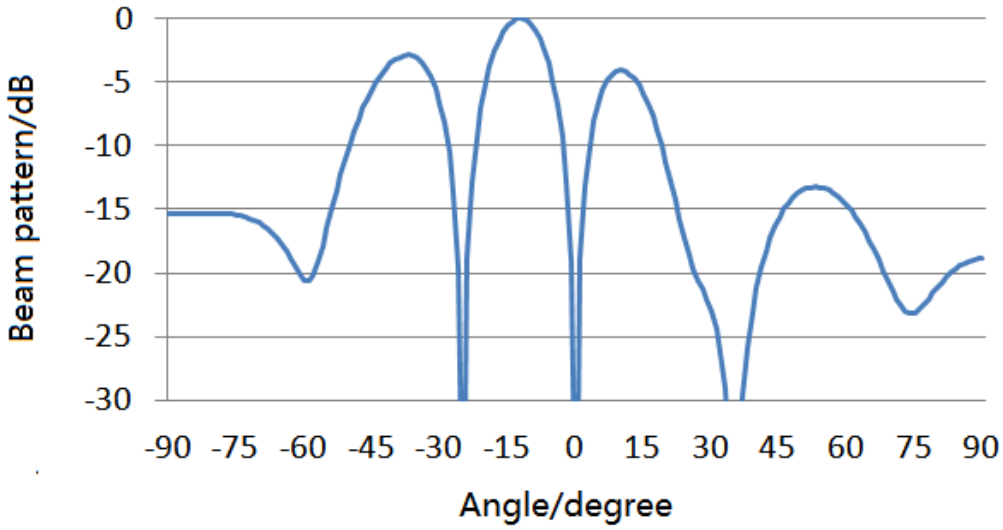

Fig.5.12 Simulated beam patterns for the TMRA at the 1st positive frequency, calculated using the simulated embedded element pattern and LCMV beamformer

predicted from array-factor theory and exhibits the desired adaptive beamforming characteristics.

5.4 Conclusion

The first part of this chapter reviewed and applied Minimum Variance Distortionless Response (MVDR) beamforming and Linearly Constrained Minimum

Variance (LCMV) beamforming to TMRA. Subsequently, an example of an 8 element TMRA has been configured to form a directive scattering pattern based on MVDR and LCMV algorithm. Results have been presented to compare the performance of a linear TMRA system to that of a conventional phased array. It is proved that TMRAs can provide a similar beamforming function comparing to the phased array. In conclusion, the TMRA system is a good alternative and a supplement of conventional phased array and TMA systems with lower cost and less complexity in hardware.

Chapter 6 PARABOLIC TMRA

6.1 Introduction

This chapter applies a new geometrical configuration, parabola, to TMRAs. Previous chapters discuss the linear planar TMRA. The feeding antenna was assumed to illuminate the scatterers in a long distance in front to the TMRA so that electromagnetic waves arrive at each scatterers with the same magnitude and phase. Such distance were ideally assumed to be in a farfield range. For a geometry of bowtie dipole TMRA shown in **Fig.4.2**, the farfield is 1.44 meters, which is relatively very large compared to the size of the TMRA. To minimize the overall size of the planar TMRA, the parabolic TMRA is proposed to duplicate the TMRA functions in a compact size.

Section 6.2 introduces the concept of parabolic TMRA and give a simple model to analyse the performance.

Section 6.3 simulates a realistic parabolic TMRA based on bowtie elements.

6.2 Parabolic TMRA concept and modelling

Section 2.6 have reviewed the reflector antennas and especially the parabolic reflector. A very important characteristic of a parabola is that points on the parabola are equidistant from a point (focus) and a line (directrix). In a Cartesian coordinates, assuming the focus is on the y axis (0, a) and directrix (y = b) is vertical to the y axis. The points on the parabola (x,y) can be described as

$$x^2 + (y-a)^2 = (y-b)^2$$
$$y = \frac{x^2 + a^2 - b^2}{2(a-b)} \qquad \textbf{Eq.6.1}$$

Assuming a parabolic time modulated reflector array consists of 8 isotropic scatterers shown in **Fig.6.1**. The scatterers are allocated on the parabola with identical spacing in x-axis. A feeding source is placed at the focus point of the parabola and illuminates the scatterers of equal power magnitude. To simplify the model, let a = b, the vertex of the parabola located at the origin. **Eq.6.1** can be modified as

$$y = \frac{x^2}{4a} \qquad \textbf{Eq.6.2}$$

The inter-element distance is set as half of the operating wavelength. The coordinates of the scattering elements are described as

$$x_i = (i-1) * 0.5 * \lambda_c$$
$$y_i = \frac{x_i^2}{4a} \qquad \textbf{Eq.6.3}$$

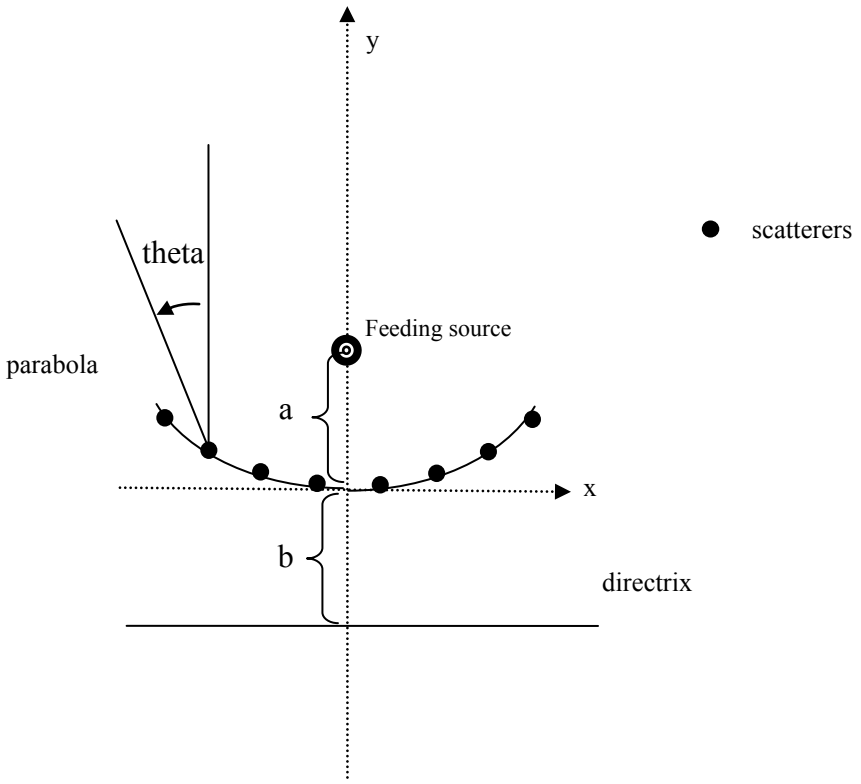

Fig.6.1 Ideal eight element parabolic TMRA: the elements equal spaced in x-axis and inter-element be half of the operating wavelength.

In addition, the direct path from the feeding antenna (focus point) to the scatterers is

$$z_i = \sqrt{x_i^2 + (y_i - a)^2} \qquad \textbf{Eq.6.4}$$

The array factor of such parabolic TMRA can be easily summarized as

$$AF = \sum_i^N exp\left(-j\frac{2\pi}{\lambda_c}(x_i sin\theta + y_i cos\theta - z_i)\right) \qquad \textbf{Eq.6.5}$$

Where $E_i(\theta)$is the radiation power of the i-th element in the direction of θ. The periodic time-domain waveform generated by the TMRA may be described as

$$f(t,\theta) = e^{j2\pi ft} * \sum_i^N E_i(\theta)\, exp\left(-j\frac{2\pi}{\lambda_c}(x_i sin\theta + y_i cos\theta - z_i)\right) * I_i(t) \qquad \textbf{Eq.6.6}$$

where $I_i(t)$ is the periodic element switching time sequence. **Eq.6.6** is very similar to the periodic time-domain waveform of the planar TMRA summarized in **Eq.3.6**. The only difference is the array factor of the parabolic TMRA contains additional phase components from y-axis and feeding paths. We can still use the Fourier series analysis. The Fourier expansion of **Eq.6.6** provides the far-field scattering pattern of the parabolic TMRA at any harmonic m ($m \neq 0$), as

$$F_m(\theta) = \sum_i^N E_i(\theta)\, exp\left(-j\frac{2\pi}{\lambda_c}(x_i sin\theta + y_i cos\theta - z_i)\right) s_{im} \qquad \textbf{Eq.6.7}$$

where the Fourier series coefficients s_{im} of the parabolic TMRA is as same as that of the planar TMRA listed in **Eq.3.9** and **Eq.3.10**.

6.2.1 Beam steering applied to an ideal isotropic parabolic TMRA

If the element switch time waveform is a progressive increasing sequence in **Fig.6.2**, identical to the ideal linear example in Section **3.3**, the parabolic TMRA can operate a beam steering functionality. Applying the same time sequence to the parabolic TMRA with $a = 10\ \lambda$, the obtained scattering pattern is shown in **Fig.6.3**. The beam steering function is duplicated.

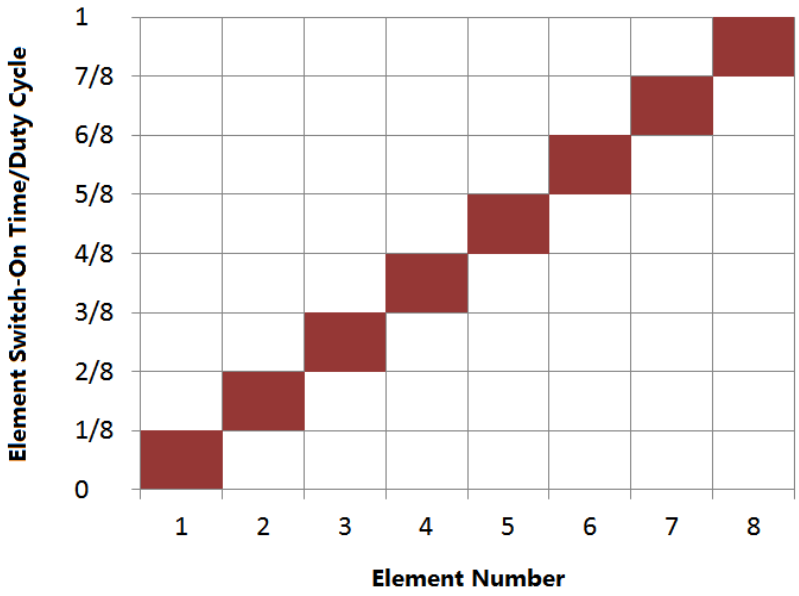

Fig.6.2 Element switching sequence to generate a beam steering function: elements are switched sequentially and progressively

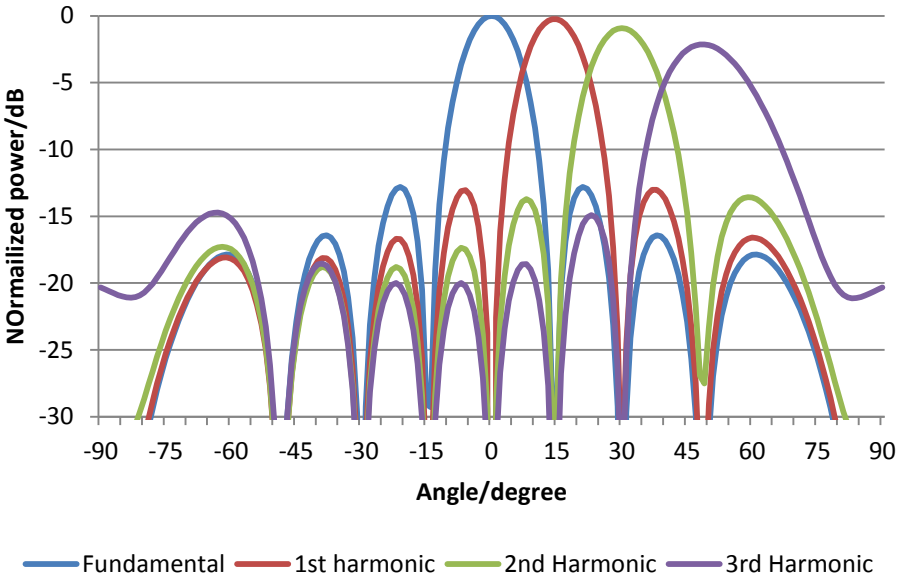

Fig.6.3 Scattering power patterns of parabolic TMRA conductiong beam steering function: distance of the focus(feed) to the TMRA apex is 10 λ.

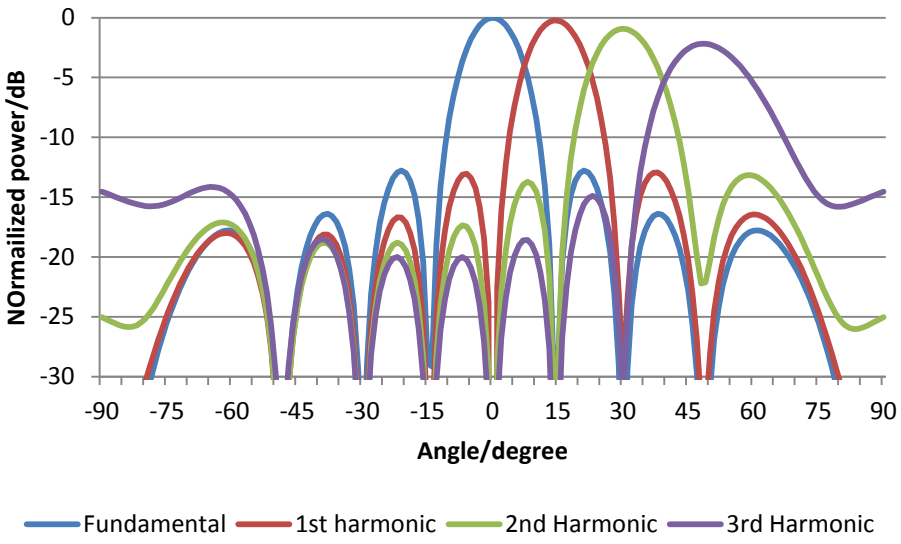

Fig.6.4 Scattering power patterns of parabolic TMRA conductiong beam steering function: distance of the focus(feed) to the TMRA apex is 5λ.

If the focus to apex distance is set as 5λ, the obtained scattering pattern for beam steering is shown in **Fig.6.4**. Comparing the results of 5 λ focus-to-apex TMRA, 10 λ focus-to-apex TMRA and planar TMRA, there are few differences in shapes and positions of beams. It can be concluded that the beam steering function have been reproduced in parabolic TMRAs. However, there is a slight difference in the when the trace move to the fire end direction (±90°). This may be explained by the phase components generated by the y axis (y_i) become dominate in fire-end direction. Overall, the differences are very small to be notice.

6.2.2 MVDR Beamforming applied to an ideal isotropic parabolic TMRA

A parabolic TMRA is conducting the MVDR beamforming. In Chapter 5 TMRA beamforming can adapt the single element scattering patterns as prior knowledge to optimize the final formed scattering pattern. When MVDR or LCMV beamforming applying to the parabolic TMRA, the method is similar and to consider the phase components in y axis and the feeding path as prior knowledge. Now give an example to

apply MVDR beamforming to an eight element parabolic TMRA. Assume the parabolic TMRA shares the same configurations as in **Fig.6.1**. Inter-element coupling are not considered in this model. Scattering pattern of the parabolic TMRA at any harmonic *m* ($m \neq 0$) is given in **Eq.6.7**. Assuming the TMRA are expecting a desired signal and a jammer, the received signals $\mathbf{X}(\boldsymbol{\omega})$ at the antenna array in frequency-domain consists of signals and noise is

$$\boldsymbol{X}(\boldsymbol{\omega}) = F(\omega)\boldsymbol{d} + \boldsymbol{N}(\boldsymbol{\omega}) \qquad \textbf{Eq.6.8}$$

where $\mathbf{N}(\boldsymbol{\omega})$ is zero-mean Gaussian noise, $F(\omega)$ is the frequency-domain snapshot of received signals and $\mathbf{d}$ is an 8×2 array manifold matrix,

$$\boldsymbol{F}(\boldsymbol{\omega}) = [F_1(\omega) \quad F_2(\omega)]^T \qquad \textbf{Eq.6.9}$$

and

$$\boldsymbol{d} = [\, \boldsymbol{d}(\boldsymbol{\omega}: \boldsymbol{k_1}) \quad \boldsymbol{d}(\boldsymbol{\omega}: \boldsymbol{k_2})] \qquad \textbf{Eq.6.10}$$

Assume that $F_1(\omega)$ is the signal of desired dircetion, and $F_2(\omega)$ is the jammers.$\mathbf{d}(\omega: k_1)$ is the manifold matrix of signal $F_1(\omega)$,

$$\begin{aligned} \boldsymbol{d}(\omega: k_1) &= [AF_1(k_1), \dots, AF_8(k_1)]^T \\ \boldsymbol{d}(\omega: k_2) &= [AF_1(k_2), \dots, AF_8(k_2)]^T \end{aligned} \qquad \textbf{Eq.6.11}$$

where $AF_i(k_n)$ the array factor and k_n is the wavenumber.

$$AF_i = E_i(\theta)\, exp\big(-j\, k_n\, (x_i \sin\theta + y_i \cos\theta + z_i)\big) \qquad \textbf{Eq.6.12}$$

In TMRA, k_n is $\frac{2\pi}{\lambda_c}$ and λ_c is one wavelength of the TMRA operating frequency. The following steps is similar to MVDR beamforming applying the linear TMRA. We need to calculate weights factor $\mathbf{w}$ to minize output signal $\mathbf{Y}(\boldsymbol{\omega}) = \mathbf{w}^{\mathbf{H}}\mathbf{X}(\boldsymbol{\omega})$, and retain the no-distortion desired signal power $F_1(\omega)$. The numerical model of such optimisation problem is,

$$min_w\, \boldsymbol{w}^{\boldsymbol{H}}\boldsymbol{S}\boldsymbol{w} \quad s.t.\ \boldsymbol{w}^{\boldsymbol{H}}\boldsymbol{d}(\omega_1: k_1) = \mathbf{1} \qquad \textbf{Eq.6.13}$$

where $\mathbf{S}$ is covariance matrix of received signal

$$\boldsymbol{S} = \boldsymbol{E}[\boldsymbol{X}(\boldsymbol{\omega})\boldsymbol{X}^{\boldsymbol{H}}(\boldsymbol{\omega})] \qquad \textbf{Eq.6.14}$$

The optimum distortionless beamformer for Eq.6.13 is

$$\boldsymbol{w}_{\boldsymbol{mvdr}} = \frac{\boldsymbol{S}^{-1}\boldsymbol{d}(\omega_1 : k_1)}{\boldsymbol{d}(\omega_1 : k_1)^{\boldsymbol{H}}\boldsymbol{S}^{-1}\boldsymbol{d}(\omega_1 : k_1)} \qquad \textbf{Eq.6.15}$$

Assume the desired signal and jammer come from the angle of -15 degree and -25 degree respectively. The feeding antenna is located at the focus 10 wavelengths from the parabola apex. We use **Eq.6.15** to calculate a weight matrix to retain the no-distortion desired signal power $F_1(\omega)$ and minimize the total output power $\mathbf{w^H X(\omega)}$. The obtained weight matrix is

$$\boldsymbol{w}_{\boldsymbol{mvdr}} = \begin{bmatrix} 0.123 \\ 0.072 + 0.107i \\ 0.144 + 0.141i \\ -0.107 - 0.123i \\ -0.075 - 0.01i \\ 0.144 - 0.084i \\ 0.116 - 0.149i \\ 0.174 + 0.074i \end{bmatrix} \qquad \textbf{Eq.6.16}$$

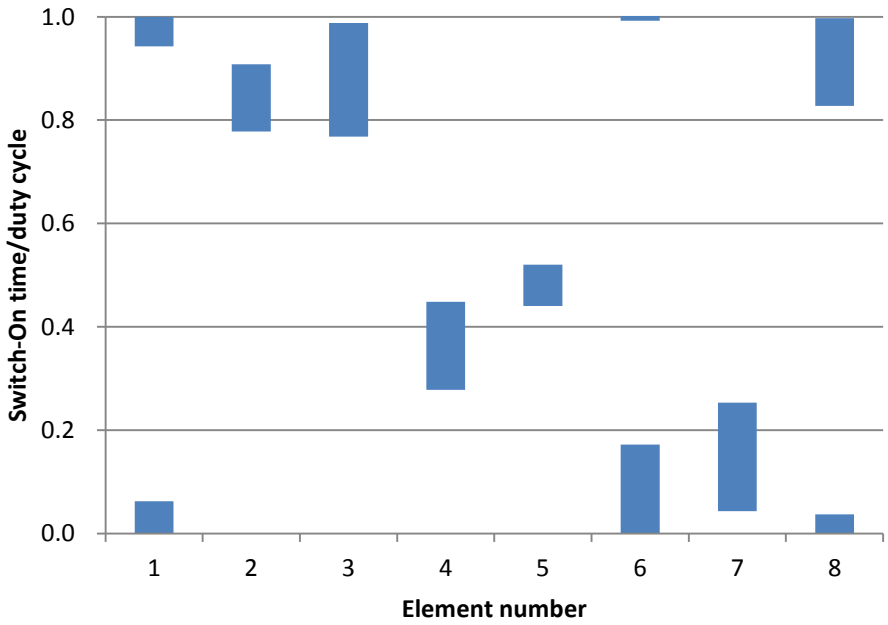

Fig.6.5 Time switching sequence generated by MVDR beamforming for ideal parabolic TMRA without inter-element coupling.

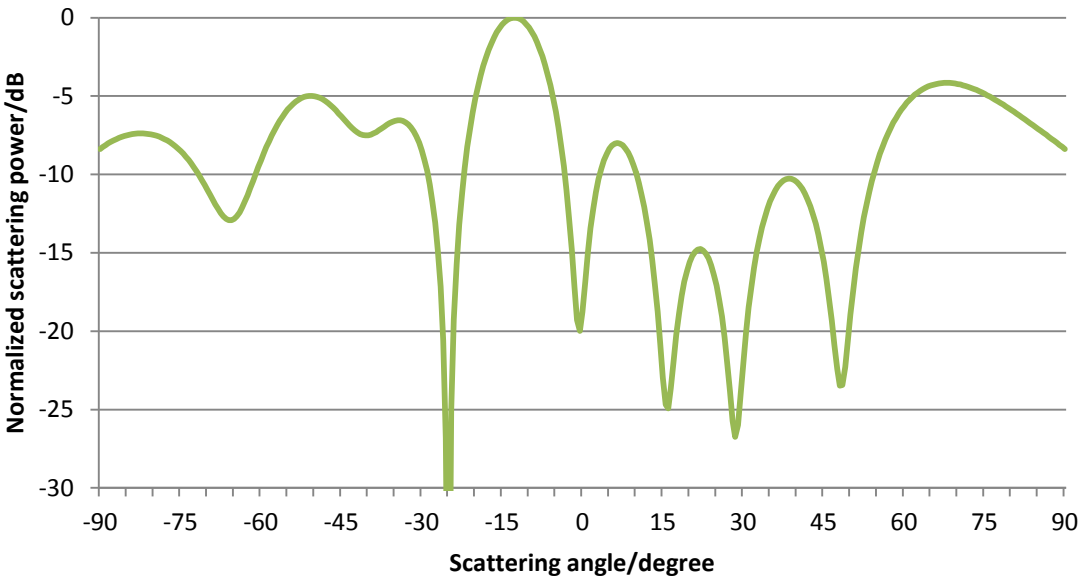

Fig.6.6 MVDR beamfomring Scattering power pattern of ideal parabolic TMRA: distance between the focus to the apex is 10 λ.

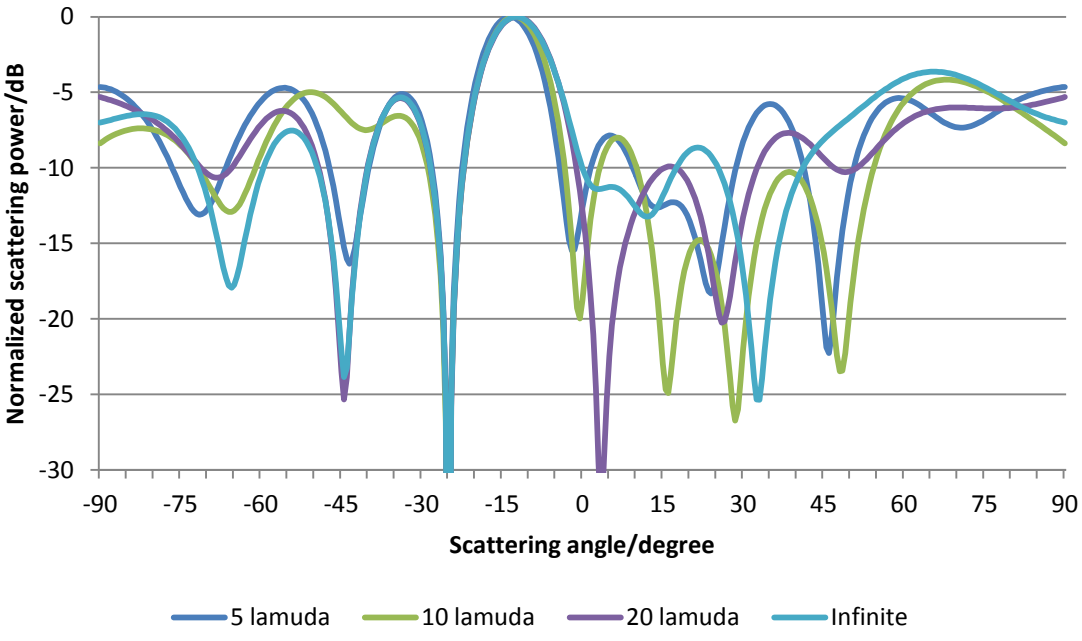

Fig.6.7 Scattering power patterns of parabolic TMRA under different focus to TMRA apex distancs. Formed main beam points at -15° and null locates at -25°.

Assuming the signals operates at the negative 1st harmonic frequency of the parabolic TMRA ($m = -1, f = f_0 - 1/T$, f_0 is TMRA operating frequency and T is switching

time period), the weight matrix in **Eq.6.16** was applied in **Eq.5.9** to calculate the scattering element switching sequence. The obtained time sequence is shown in **Fig.6.5**.

Using the obtained time sequence to calculate the scattering patterns of the parabolic TMRA, **Fig.6.6** shows the normalized fundamental and first positive/negative scattering patterns of the parabolic TMRA using MVDR beamforming. Beamforming has been successfully reproduced using the parabolic TMRA. The formed pattern peaks at -15°, which is the presumed direction of the desired signal while nulls at -25° (the direction of jammer). A further examination of beamforming function under various focus/feeding position (5λ, 10λ, 20λ infinite from the scattering elements) was carried out and results are shown in **Fig.6.7**. For all focus/feeding positions, Parabolic TMRAs are able to form desired scattering pattern with desired peaks and nulls. The influence of phase components in y-axis and feed path are eliminated by considering them as prior knowledge. As same as predicated in the beginning, the parabolic TMRA is well able to conduct the MVDR beamforming function.

6.3 Parabolic TMRA based on bow-tie dipole element

Exam a more practical parabolic TMRA based on bow-tie dipole element. Linear bowtie dipole TMRA has been simulated and test in Chapter IV and V. It has been proved to be able to conduct beam steering and beamforming. For parabolic TMRAs, examples are going to be given to show how beam steering and beamforming works along with the parabola configuration.

An example of a bowtie dipole parabolic TMRA consists of 8 x 8 scattering elements. Shown in **Fig.6.8**, the 8 element in a row connected to form a sub-array and each of the sub-array can be switched on and off individually. The substrate is set to be FR4 with relative permittivity at $\varepsilon = 4.4$and thickness of 1.6 mm. Assume the TMRA

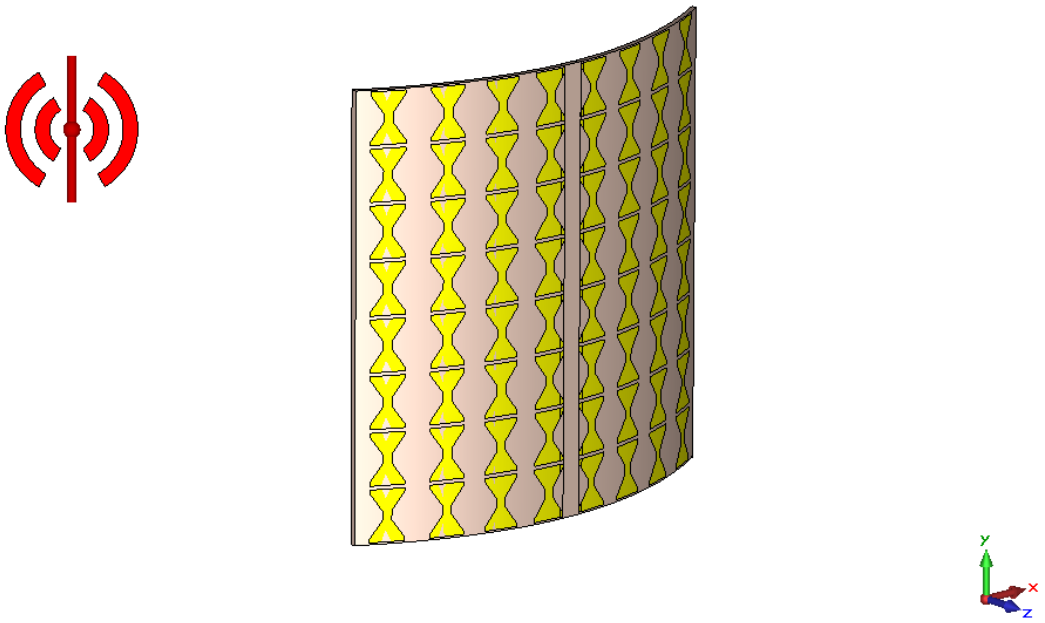

Fig.6.8 Screenshot of an 8 x 8 parabolic TMRA illuminated by a feed antenna in CST Microwave studio. The TMRA is bent to a parabolic substrate.

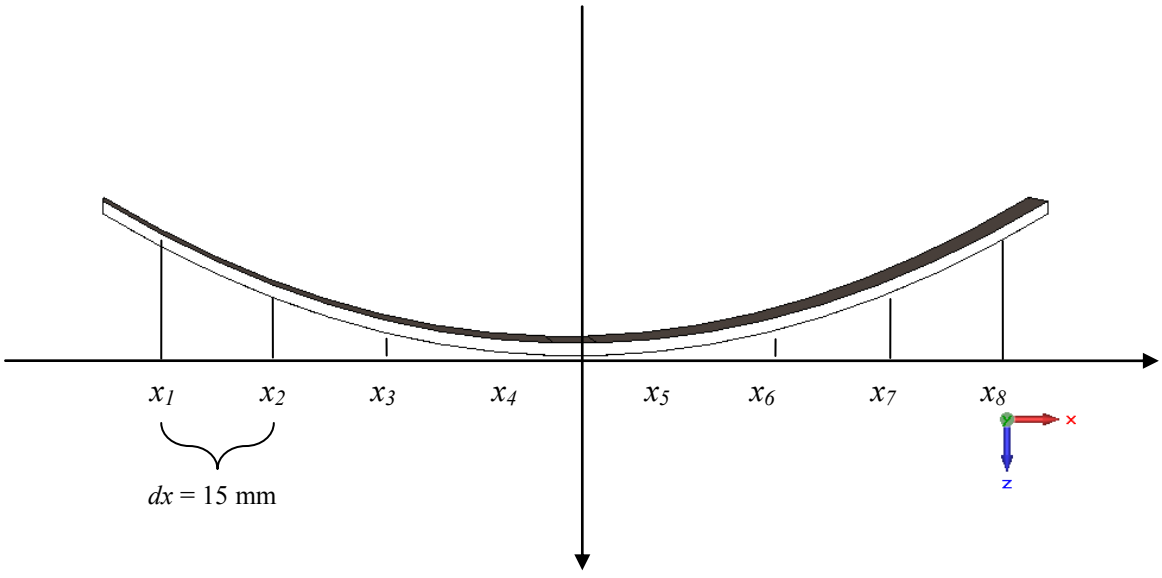

Fig.6.9 Top view of the parabolic TMRA. Inter-element distance in x axis is 15 mm

operating centre frequency is 9.5 GHz. Shown in the top view of the parabolic TMRA (**Fig.6.9**), the inter-element distance in x-axis is *dx = 15 mm* approximately half wavelength of 9.5 GHz. The focus of parabola (0 mm, 0 mm, -315 mm) locates at 10 wavelength away from the apex, which is at the origin (0 mm, 0 mm, 0 mm). The physical configuration of a single bowtie dipole scattering element is the same as that of the planar TMRA in **Chapter IV**. However, the parabolic element is designed to be bent along the parabola instead of flat element configuration in planar TMRA.

6.3.1 Modelling a parabolic TMRA in CST Microwave studio

The following steps shows how to construct such parabolic TMRA in CST Microwave Studio. Shown in **Fig.6.10**, first step is to draw a flat bowtie dipole reflector array. The bowtie elements were as same as these used in conventional TMRA and the inter-element distance was 15 mm. Secondly, a parabolic substrate is generated. The material of the substrate is 1.6 mm thickness FR-4 ($\varepsilon_r = 4.4$). The substrate overall size 124 mm by 120 mm. CST can use predefined formulas to generate two analytical faces, which corresponded to the top and bottom side of the parabolic substrate. The substrate was formed by filling up the space between these two analytical faces using material FR-4. Subsequently, a special bending function can attach the flat reflector array onto the parabolic substrate. The planar reflector elements were placed to gently contact the substrate but not insert into it. CST Microwave Studio can bent a flat surface to a curled surface if they are contacted. Finally, SHORT and OPEN circuits are used to represent diode ON/OFF states. It might be notable that equivalent RCL circuits of PIN diodes were replaced by simple SHORT/OPEN circuits. This is because the changing of feeding source and CST Microwave Studio solver. The feeding source is no long plane wave but a fixed radiating antenna (horn antenna in this example). In practice, simulating a parabolic TMRA fed by a horn antenna using Time-domain Solver in CST

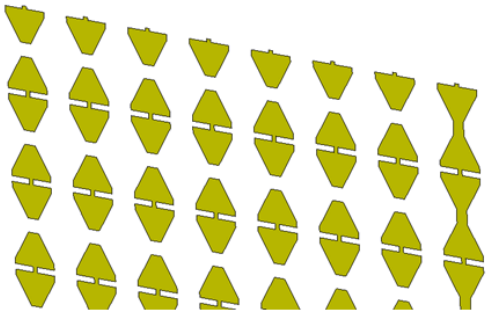

a). Draw flat TMRA

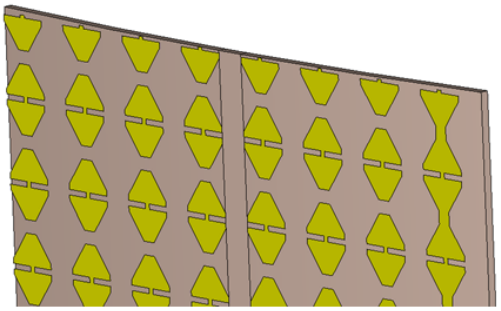

b). Draw a parabolic FR-4 substrate

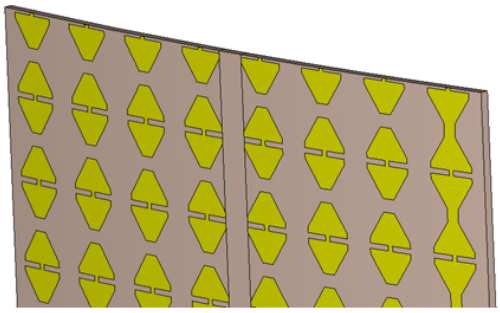

c). Bent the reflector array onto the substrate

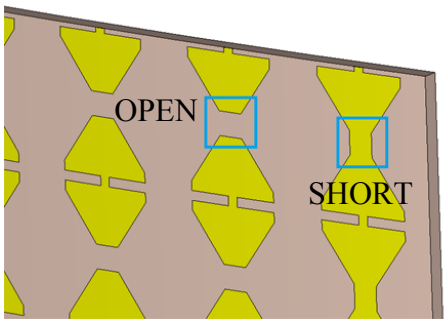

d). Use short/open circuit to represent diode ON/OFF

Fig.6.10 Steps to construct a parabolic TMRA in CST Microwave studio.

Microwave Studio is very difficult for an average computer of today (ultra-long calculation time and high risk of modelling breakdown). Time-domain Solver in CST stimulates the structure at a previously defined port using a broadband signal. This enables the S-parameters for the entire desired frequency range as well as the electromagnetic field patterns at various desired frequencies, to be obtained from a single calculation run. However, the calculation effort will increase exponentially against the size of models. In Time-domain Solver, 20 Million mesh cells are needed to model a parabolic TMRA, which is 10 times larger than that of a planar TMRA (2 Million). It is recommended by the CST handbook to use an Integral Equation Solver to simulate large models. The discretization of the calculation area is reduced to the object boundaries and

thus leads to a linear equation system with less unknowns than volume methods, which is used in Time-domain solver. Due to the different meshing method for Integral Equation Solver, PIN diodes' equivalent RCL circuits cannot be applied in the parabolic TMRA simulation as lumped elements are not supported by Integral Equation Solver. A configuration of short and open circuits is used to represent PIN diode ON and OFF states is shown in **Fig.6.10.d**,. There is an alternative approach to reduce the CST calculation effort based on introducing the periodic boundary conditions with a single row of scattering elements. Such approach will significantly reduce the computational time for large models. However, there is some limitations as finite number of elements has been used in the proposed parabolic TMRA.

Next, a feeding antenna was placed at the focus, 10 wavelengths of 9.5 GHz (315 mm) away from the TMRA apex. The feeding antenna was a horn antenna, which has directive radiation pattern in z direction (**Fig.6.11)**. The radiation pattern of the horn antenna was pre-calculated and imported into the TMRA project as a farfield source. This could save calculation time by decreasing the overall project mesh-cells. Farfield monitors were set up to record the scattering power pattern of the parabolic TMRA.

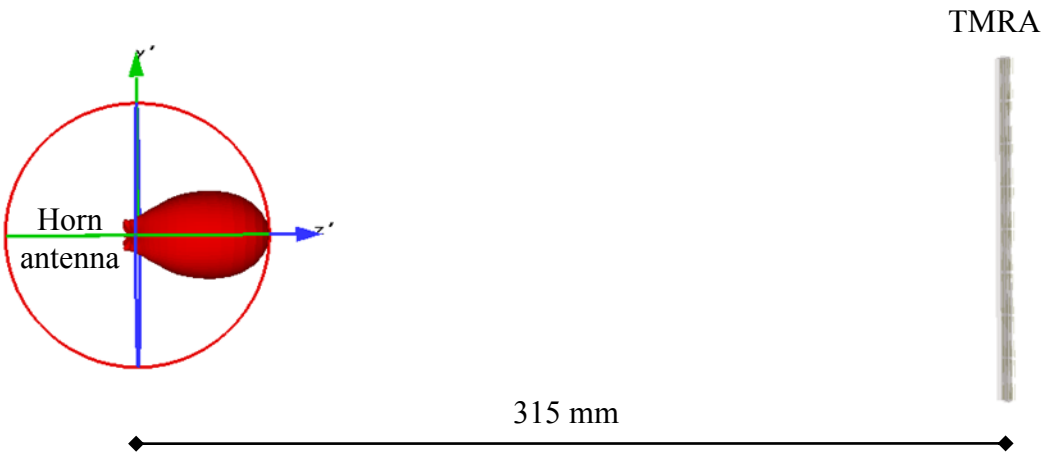

Fig.6.11 Parabolic TMRA fed by an horn antenna

As the parabolic TMRA consists of 8 serial-connected sub-array, CST Microwave Studio was used to calculate 8 scattering power patterns. Each embedded pattern was recorded when only one sub-array ON and rest of them OFF. These patterns, Et_i, not only include the effects of mutual coupling, but also contain both amplitude and phase information relating to their spatial position,

$$Et_i(\theta) = E_i(\theta)\, exp\left(-j\frac{2\pi}{\lambda_c} d_i sin\theta\right) + mutual\ coupling \qquad \textbf{Eq.6.17}$$

This is very similar process to record the farfield scattering patterns of planar bowtie dipole TMRAs. In the next step, **Eq.4.2** is used to calculated parabolic TMRA harmonic scattering patterns with different time sequences.

6.3.2 Beam steering applied to parabolic bowtie dipole TMRA

For the beam steering function, the parabolic bowtie dipole TMRA can use the progressive time sequence in **Fig.6.2**. The simulation process is same as the planar bowtie TMRA simulation in **Section 4.3**. The only differences is embedded scattering patterns of the planar TMRAs simulated using CST Microwave Studio T-Solver are replaced by the embedded patterns of parabolic TMRAs obtained using CST Microwave Studio I-Solver. The scattering patterns were put into **Eq.4.2** to calculated time-modulated performance of the parabolic TMRA. Shown in **Fig.6.12**, the results were based on the CST predicted scattering patterns from the TMRA with switch-controlled bowtie elements. Only the first three positive harmonic frequencies are shown in the figure. Fundamental beam pattern was not included due to suffering from inter-element coupling. The beam directions of each harmonics are located at angles of 15°, 30° and 45° respectively.

Fig.6.13 shows the first positive scattering patterns of the ideal parabolic TMRA and bowtie dipole parabolic TMRA. Comparing the results of TMRAs based on ideal and bowtie elements, for lower order harmonics, nulls' levels have increased and traces have

some ripples in the angle beyond ±50°. This can be explained by considering the differences between the isotropic and the bowtie scatterers. Firstly, the assumption of isotropic elements ignores the differences in the scattering pattern of individual scatterers.

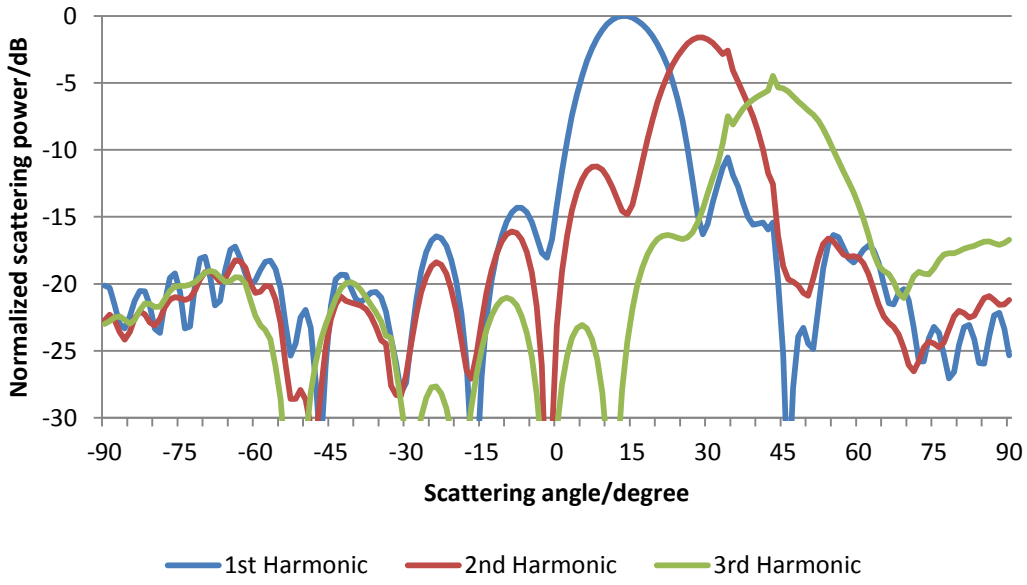

Fig.6.12 Scattering power patterns of parabolic bowtie dipole TMRA conducting beam steering function.

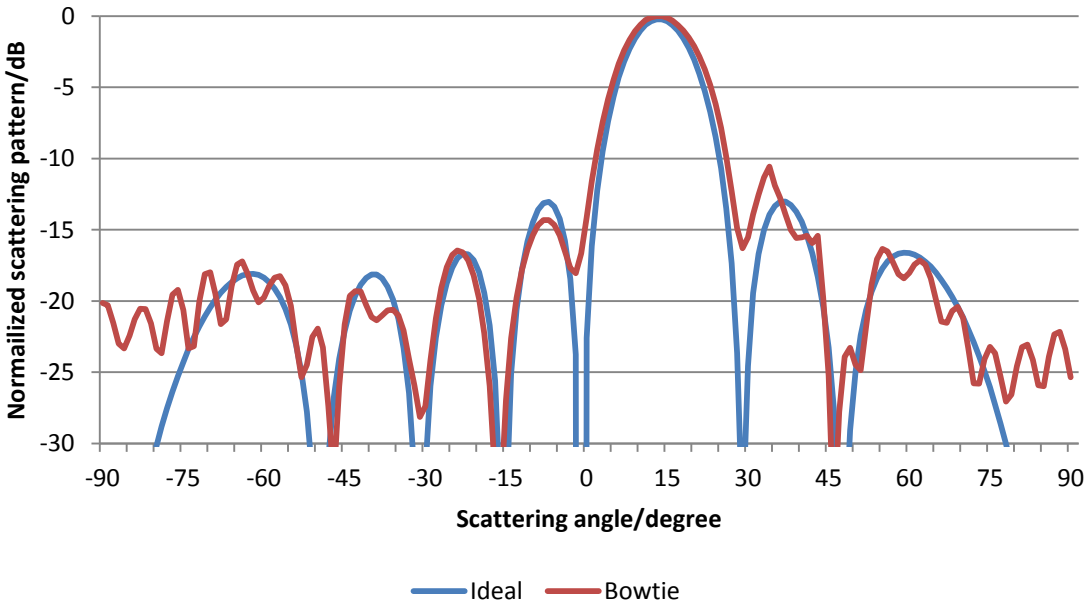

Fig.6.13 Comparison of the 1st positive harmonic scattering patterns of the ideal isotropic parabolic TMRA and the bowtie element parabolic TMRA

Secondly, the signals from the feeding antenna arrive at individual elements with different phases and amplitudes, which is due to the non-ideal radiating pattern of the feeding source. The inter-element coupling is also not considered in ideal case. However, beam directions and sidelobes of theoretical and simulated results agree with each other. The proposed parabolic bowtie dipole TMRA have demonstrated the ability to conduct beam steering functionality with acceptable rise in nulls.

6.3.3 MVDR Beamforming applied to parabolic bowtie dipole TMRA

A parabolic bowtie dipole TMRA is configured to perform the MVDR beamforming. For comparison purpose, signals' directions are assumed to be identical to those of the ideal case (desired signal @ -15° and jammer @ -25°) in Section **6.2**. As same as the planar bowtie dipole TMRA, the embedded scattering patterns calculated by CST Microwave Studio includes amplitude, phase and inter-element coupling as prior knowledge. The manifold matrix in **Eq.6.11** is then modified by replaced the array factors AF_i using TMRA scattering patterns $Et_i(\theta)$. Assume that $F_1(\omega)$ is the signal of desired dircetion, and $F_2(\omega)$ is the jammers.$\mathbf{d}(\omega: k_1)$ is the manifold matrix of signal $F_1(\omega)$,

$$\begin{aligned} \boldsymbol{d}(\omega: k_1) &= [Et_1(\theta_1), \dots, Et_8(\theta_1)]^T \\ \boldsymbol{d}(\omega: k_2) &= [Et_1(\theta_2), \dots, Et_8(\theta_2)]^T \end{aligned} \qquad \textbf{Eq.6.18}$$

where $\mathrm{Et_i}(\theta_\mathrm{n})$ is the embedded scattering pattern when the *i-th* sub-array ON and rest of them OFF. θ_n is the *n-th* signal direction of arrival. Put the updated version of manifold matrix into **Eq.6.15** to calculate a weight matrix **w**. Assuming the both of the signals operate at 1st negative harmonic frequency of the parabolic TMRA that harmonic number *h* is -1. The obtained weight matrix is

$$\boldsymbol{w_{mvdr}} = \begin{bmatrix} -0.02 - 0.05i \\ -0.09 - 0.09i \\ -0.32 \\ -0.06 + 0.083i \\ -0.04 - 0.029i \\ 0.19 - 0.05i \\ 0.12 - 0.09i \\ 0.21 - 0.14i \end{bmatrix} \qquad \textbf{Eq.6.19}$$

The weight matrix in **Eq.6.12** was deployed in **Eq.5.9** to calculate the element switching sequence shown in **Fig.6.14**. Under such conditions, obtained scattering patterns shown in **Fig.6.15** prove that the parabolic bowtie element time modulated

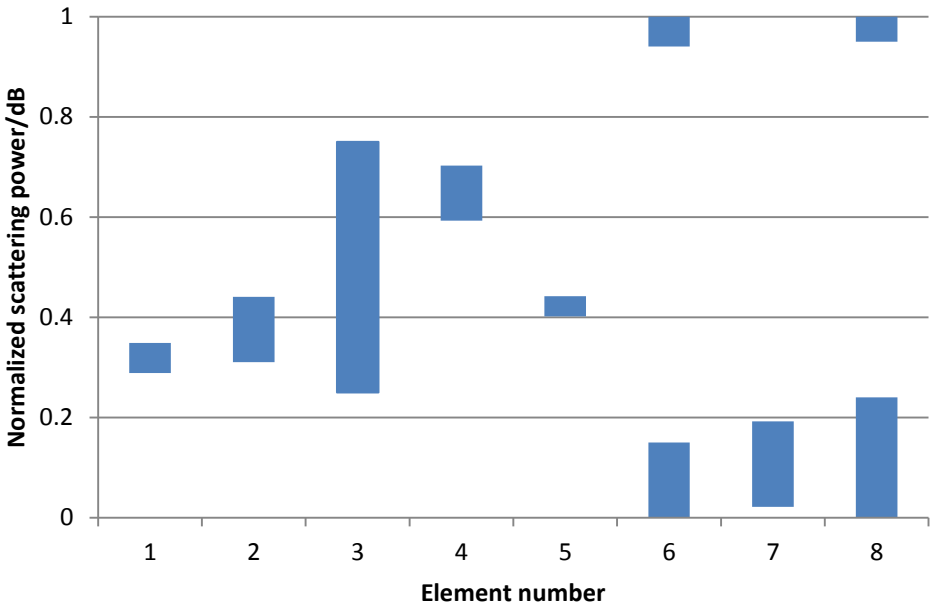

Fig.6.14 Time switching sequence generated of the parabolic bowtie dipole TMRA based on MVDR beamfomer peaks at -15° and nulls at -25°.

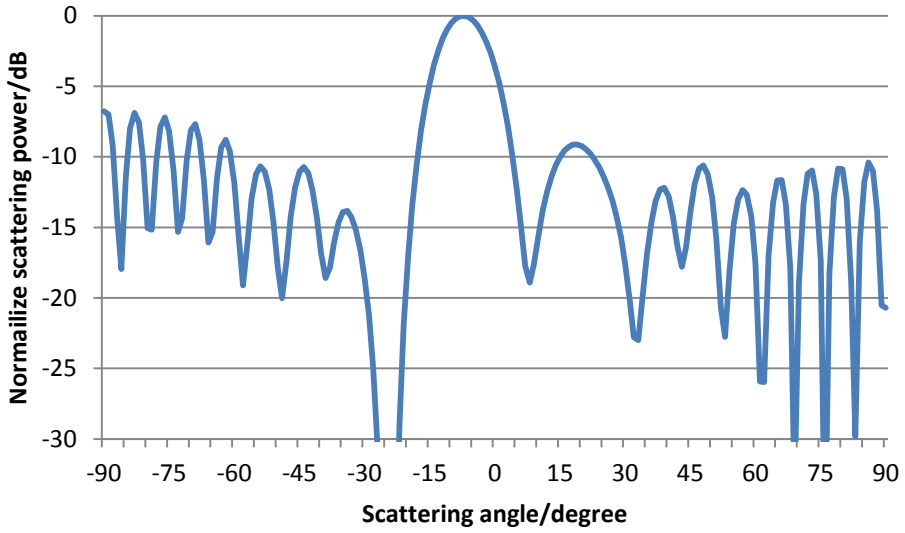

Fig.6.15 Scattering power patterns of parabolic bowtie dipole TMRA conducting beam forming function.

array is able to form a directive beam in the angle of -15° and nulls at the prescribed jammer's direction (-25°).

6.4 Conclusion

This chapter has introduced a special physical configuration of TMRA, parabolic time modulated reflector array. The concept of the parabolic TMRA has been verified by an ideal example based on isotropic scattering element and a realistic model based on bowtie dipole sub-arrays. Both of examples suggested that parabolic TMRA is able to conduct basic beam steering and beamforming functions. Parabolic TMRAs are good choice for closed-fed TMRAs.

Comparing to the conventional parabolic reflector antenna systems, the parabolic TMRA shares identical parabola design but using reconfigurable scattering elements. As the fast developing in 3D printing and semiconductor industry, the manufacture process is considerable feasible. The future of parabolic TMRA could be found in the area of electronic scanning, object/direction finding, directional telecommunications and space probing.

Chapter 7 ENERGY EFFICIENCY OF TMRAS

7.1 Introduction

Time modulated arrays suffer from power loss as the energy is transferred into sidebands (harmonic frequencies). In recent years, scientists adopted various approaches to reduce the amount of power radiated into the sideband frequencies and to increase the system power efficiency. A common approach is to use optimization algorithms to reduce the sideband radiation **[3-4]**. Directive antennas [**6**] and special sub-array layouts [**7**] are also suitable solutions. As part of time-modulated arrays' family, TMRAs suffer the same low efficiency due to side band loss. However, the focus of this chapter is not only side band loss but also the energy efficiency challenges when time-modulation concept applied on reflectarrays.

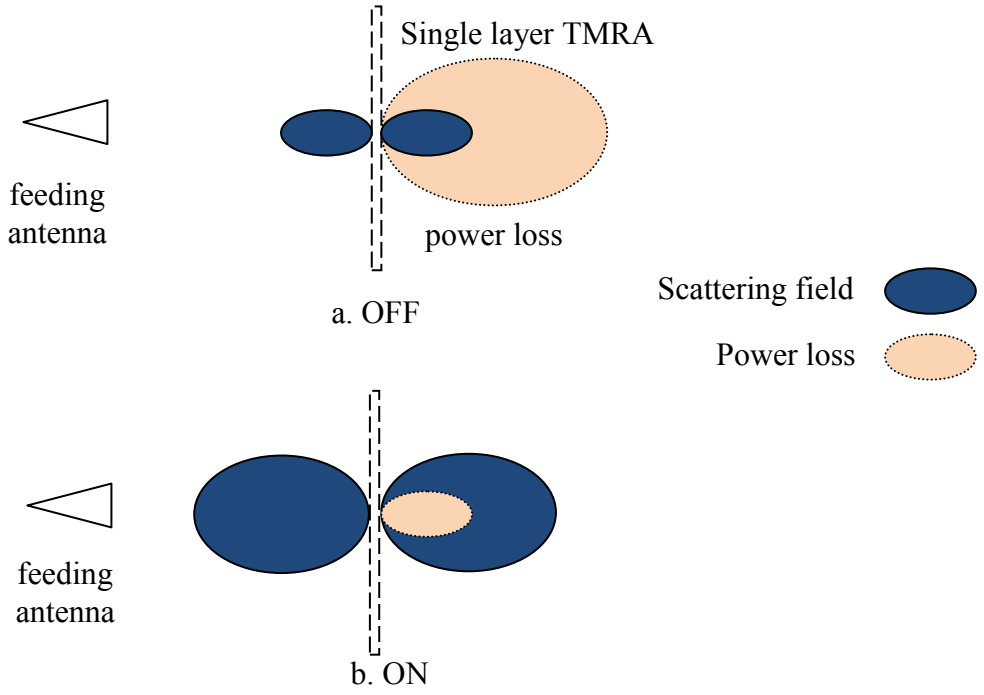

Fig.7.1 Simple model of conventional single layer TMRA when OFF and ON.

In a single-layer TMRA, elements are periodically switched between ON and OFF states. Ideally, it is assumed that the element is fully resonating when ON and not resonating when OFF. Shown in **Fig.7.1**, when the element is OFF, energy is 'wasted' by transmitting through TMRA. For an example of the eight-element TMRA [**94**] conducting beam steering function, the peak of fundamental frequency response (**SEE Fig.7.2**) is 18.06 dB lower in power compared to the response of the same TMRA when all element are reflecting (ON). As only one element is ON for any instant of time, this gives a theoretical, first order, reduction in gain of approximately 9dB compared to that of fully energized array. We hope the energy arriving at the scattering elements could fully reflect towards the desired directions. Such assumption is un-realistic in the physical reflectarrays. In a reflectarray, scientists have proposed methods to reduce the losses of reflectarrays using different materials [**95**], feeding methods [**67**] or resonator shapes [**68**]. Sometimes, the multi-layer layout can enhance both the functionalities and performances of a reflectarray. In [**96**], a stacked or multi-layer patch reflectarray was designed to provide a coverage of Australia and New Zealand for satellites broadcasting. Publication [**97**] proposed a three-layer microstrip reflectarray, which can generate a contoured beam for space applications.

This chapter explores different approaches to reduce the loss and improve the efficiency. Section **7.2** discusses the methods to relocate the power distributions at fundamental and harmonic frequency using specific time sequence. Section **7.3** adopts the multi-layer method used in conventional reflectarrays and introduces a double-layer time modulated reflector-array to improve the scattering efficiency. The combination of improved time sequence and double layer design aims to improve the energy efficient significantly.

7.2 Reduce losses by increasing element-ON time

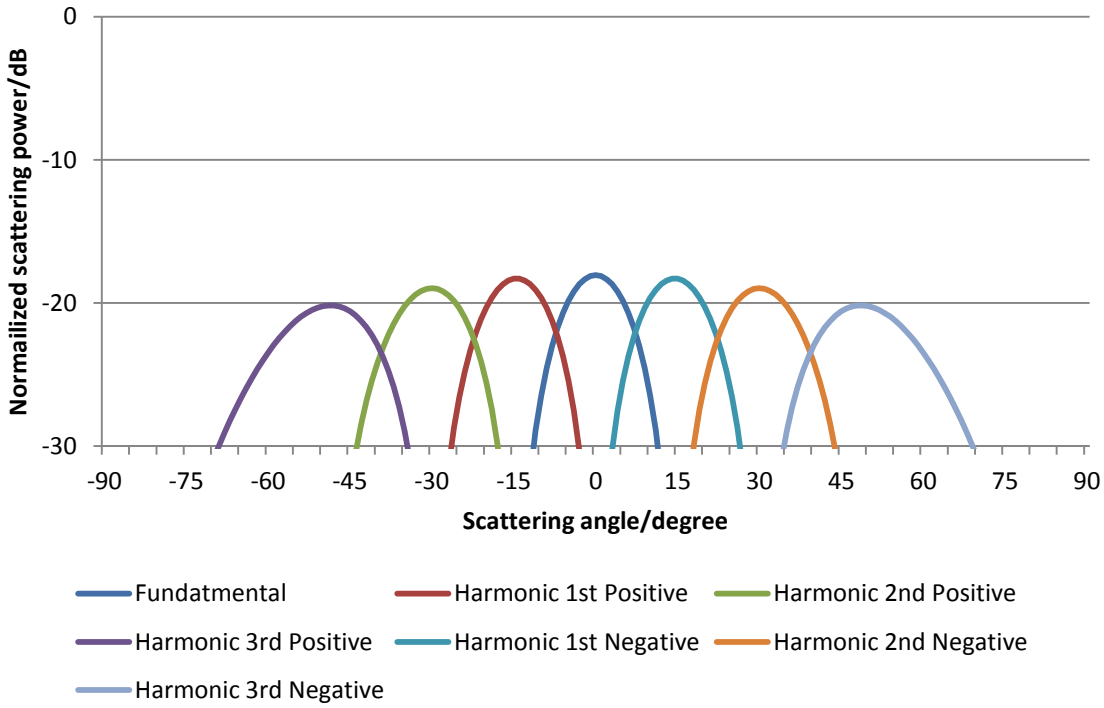

Fig.7.2 Scattering patterns of single layer TMRA conducting a beam steering function. The element-ON time is 12.5% duty cycle.

One way to lower the reduction in gain is to increase the element-ON time ($t_{ioff} - t_{ion}$). This is because the increased overall element-ON time of the time sequence emerges the energy towards fundamental and lower order harmonics [**8**]. According to the scattering-pattern formulas in **Eq.3.18** and **Eq.3.24**, the peak power of the beam in fundamental increases and that of the lower order harmonic fluctuates as increasing of element-ON time. As the harmonic responses are not increase linearly against element-ON time, there is a certain limit by just simply change the element-On time. An example of an eight element TMRA conducting beam steering can demonstrate how that works.

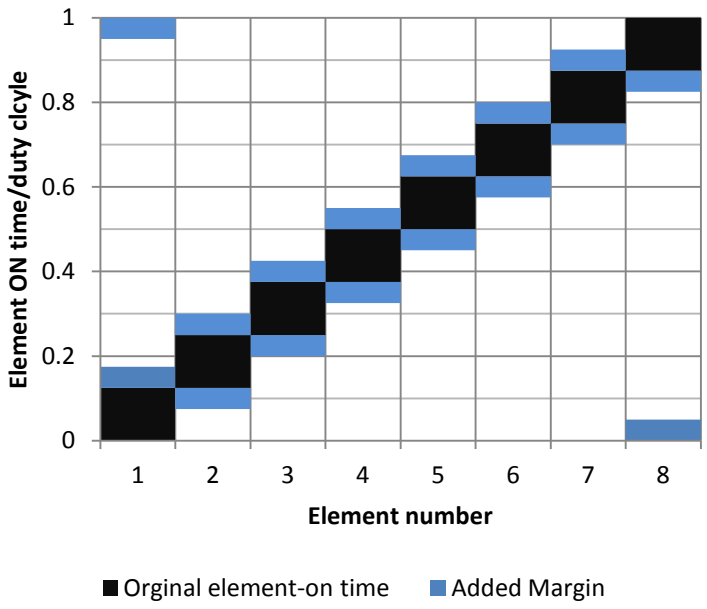

Fig.7.3 TMRA element switching sequence: elements are switched sequentially with additional ON-time.

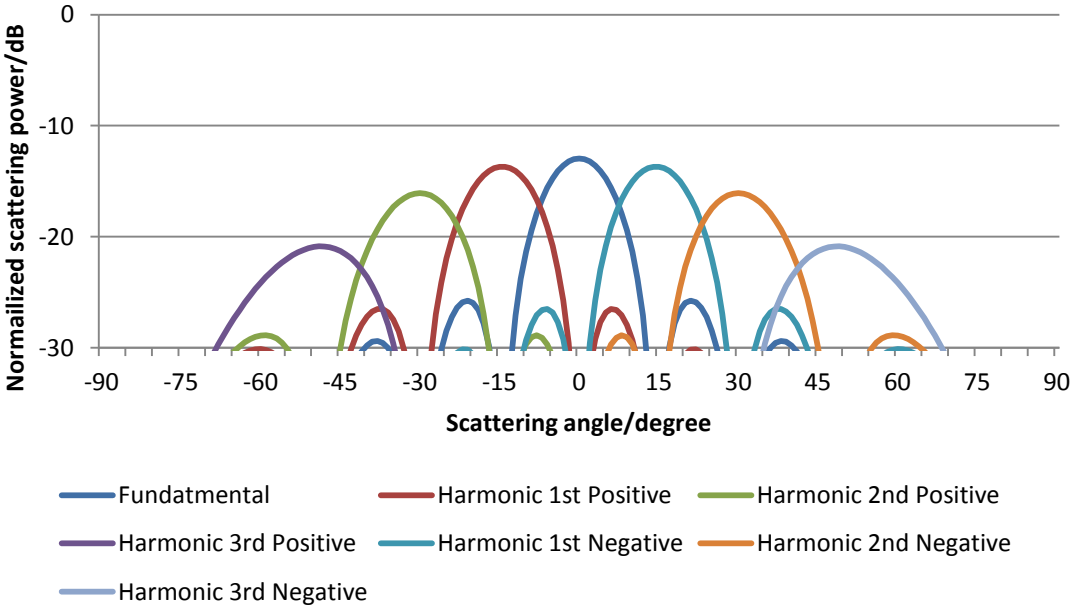

Fig.7.4 Scattering patterns of single layer TMRA conducting a beam steering function. The element-ON time is 0.225 duty cycle.

Assume an eight element planar TMRA with inter-element distance be half wavelength of the fundamental frequency. The radiation pattern of elements are assumed to be identical and isotropic. Inter-element coupling is not considered. Shown as black in

Fig.7.3, the original periodic time sequences energize the TMRA elements progressively to steer the fundamental and harmonic beams [**94**]. The single element-ON time is 12.5% (1/8) of one full duty cycle. The formed scattering patterns are shown in **Fig.7.2**. Time margins of 0.05 duty cycle are added to before and after the original element-ON time. The new time sequence of a 0.225 duty cycle increases the origin element-ON time while retains the progressive phase shifts, which are used to steer the beams. **Fig.7.4** shows the improved scattering patterns of the fundamental and harmonic frequency with increased element-ON time. The results shows increasing in the fundamental and first two harmonic beams. The peak of the fundamental frequency scattering pattern increases by 5.16 dB in power compared to result in **Fig.7.2**.

The magnitudes of the main beams of the fundamental and harmonic frequencies can be calculated using the TMRA scattering power equations in **Eq.3.10** and **Eq.3.14**. **Fig.7.5** shows the main beams' magnitudes of the fundamental and first 3 harmonics of the eight element beam-steering TMRA versus the of element-ON time ranged from zero to one full duty cycle. The fundamental response increases as the increasing of the element switch-ON time. However, the values of the harmonic frequencies fluctuate for the whole range from zero to one full duty cycle. From the results in **Fig.7.5**, a switch-ON time for the eight element TMRA can be chosen at of 1/6 (0.167) full duty cycle where the third harmonic response reaches its maximum while others' values are acceptable. Or when the switch-ON time is 0.811 duty cycle, the sum of powers at fundamental and first three harmonics reach the maximum.

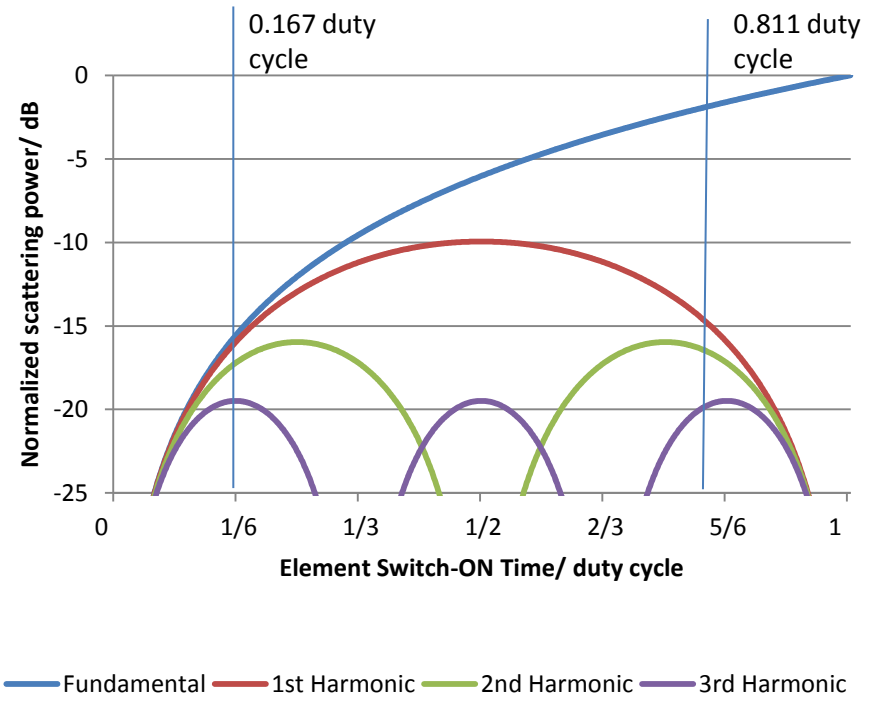

Fig.7.5 The main beam magnetudes of fundamental and harmonic scattering patterns of a single layer TMRA conduting beam steering vs. the element-On time.

7.3 Reducing losses using a double-layer TMRA

In single layer TMRA, energy is 'wasted' by transmitting through TMRA. A simple solution would be to add a ground plane behind the reconfigurable scattering element layer. The ground plane reflect the energy when the front active element is OFF. At any instant, either one element from the front active layer (see **Fig.7.6.b**) or the back ground plane (see **Fig.7.6.a**) scatterers the illuminating wave. This can increase scattering in the front hemisphere.

Initially consider a single element of the double-layer TMRA. Referring to **Fig.7.6.c** let a single unit element of the TMRA be modelled as a pair of isotropic scattering elements - the top element representing scattering from the active scattering element and the bottom element representing scattering from the back-plane a distance of *d* behind the active surface. Now assume an ideal scenario in which scattering element

can be used to switch between resonant (ON) and non-resonant (OFF) states. When the element is ON, it is assumed that scattering is solely due to the front element. On the contrary, when it is OFF, scattering is from the back element. The TMRA is also assumed to be illuminated at

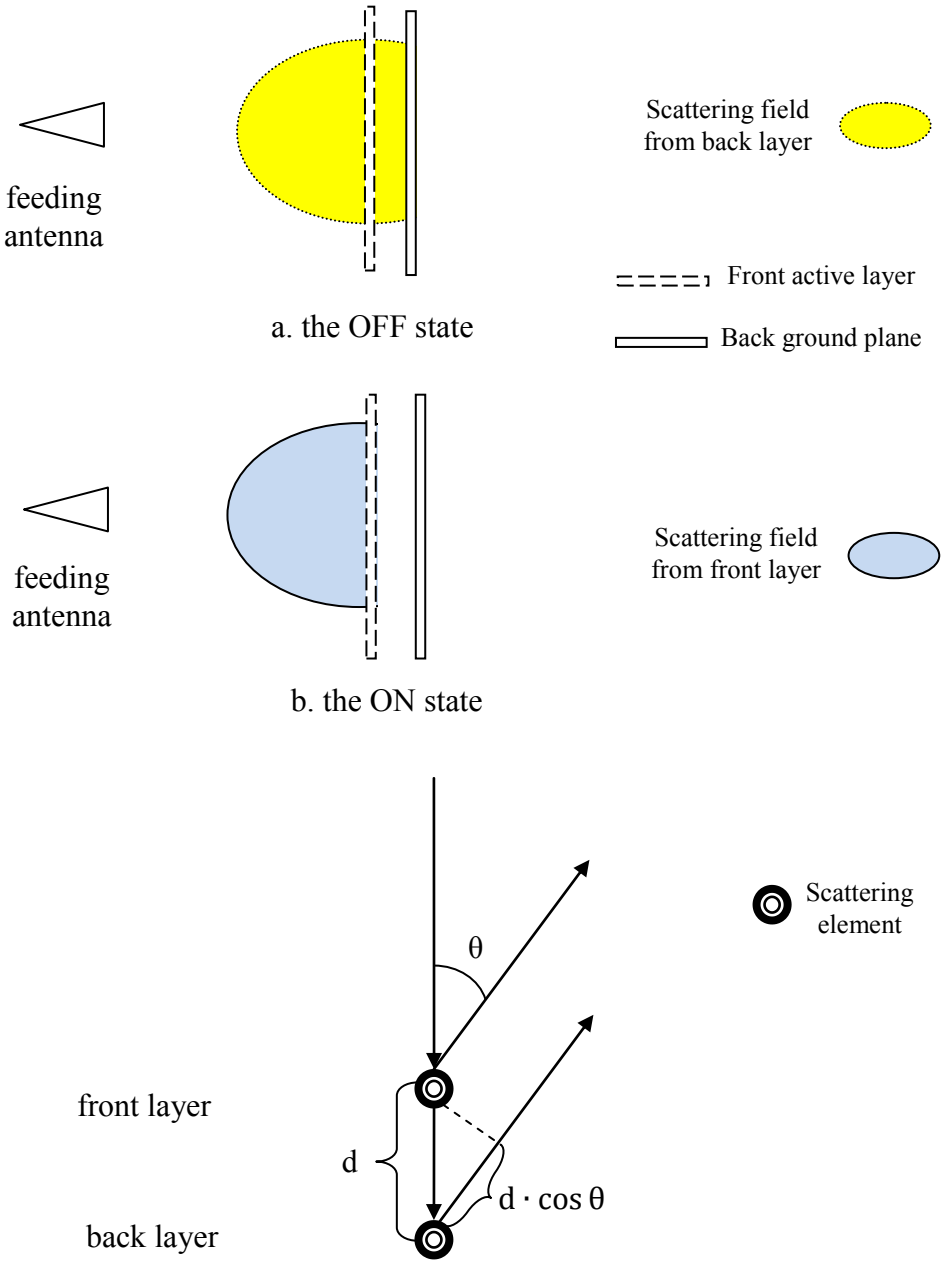

Fig.7.6 Simplified description of a double-layer TMRA element: at any instance, the scattering is either from front layer element or back layer element

normal incidence by a continuous wave radiated from a feeding source at the farfield distance and that the wave arrived at every element with same magnitude and phase. We assume that the magnitude of the scattered field from both the front and back elements are $Eu_i(\theta)$ and $El_i(\theta)$. There exists a phase difference between the two scattering states given by $e^{-j\beta d}$ where $k = \frac{2\pi}{\lambda}$ is the propagation phase constant at the frequency of illumination. For an *N*-element double-layer TMRA, the scattering pattern $E(\theta, t)$ is combination of the scattering from upper elements $Eu(\theta, t)$ and lower elements $El(\theta, t)$,

$$\begin{aligned} E(\theta,t) &= Eu(\theta,t) + El(\theta,t) \\ Eu(\theta,t) &= \sum_{i}^{N} Eu_i(\theta)\, exp(ja_i) * Iu_i(t) \\ El(\theta,t) &= \sum_{i}^{N} El_i(\theta)\, exp(jb_i) * Il_i(t) \end{aligned} \qquad \textbf{Eq.7.1}$$

where $Iu_i(t)$ and $Il_i(t)$ are the time modulation signal of front layer and back layer respectively, and

$$\begin{aligned} a_i &= k * p_i * sin(\theta) \\ b_i &= k * (p_i * sin(\theta) + d + d * cos(\theta)) \end{aligned} \qquad \textbf{Eq.7.2}$$

and p_i is the position of the *i-th* element. As stated in the beginning, for double-layer TMRA, at any single time, the scattering is either from front layer element or back layer element. Assume time modulation signals are periodic, the time modulation signal for lower layer elements $Il_i(t)$ can be interpreted as *1-*$Iu_i(t)$,

$$\begin{aligned} Iu_i(t) &= \begin{cases} 1, & nT_0 + t_{ion} \le t < nT_0 + t_{ioff} \\ 0, & others \end{cases} \\ Il_i(t) &= \begin{cases} 0, & nT_0 + t_{ion} \le t < nT_0 + t_{ioff} \\ 1, & others \end{cases} \end{aligned} \qquad \textbf{Eq.7.3}$$

where T_0 is the periodical full duty cycle and n is a integer. The Fourier series of $Iu_i(t)$ and $Il_i(t)$ is

$$\begin{aligned} Su_{im} &= \frac{1}{T_0}\int_0^{T_0} Iu_i(t)\, e^{-jm\frac{2\pi}{T_0}t}\, dt \\ Sl_{im} &= \frac{1}{T_0}\int_0^{T_0} Il_i(t)\, e^{-jm\frac{2\pi}{T_0}t}\, dt \end{aligned} \qquad \textbf{Eq.7.4}$$

and their exponentiation forms,

$$Su_{mi} = \frac{\sin\{\pi m(\tau_{ioff} - \tau_{ion})\}}{\pi m} e^{-j\pi m(\tau_{ioff}+\tau_{ion})}$$
$$Sl_{mi} = \frac{-\sin\{\pi m(\tau_{ioff} - \tau_{ion})\}}{\pi m} e^{-j\pi m(\tau_{ioff}+\tau_{ion})} \quad \textbf{Eq.7.5}$$

where $\tau_{ioff} = \frac{\mathrm{t_{ioff}}}{T_0}$ and $\tau_{ion} = \frac{\mathrm{t_{ion}}}{T_0}$. The derivation of **Eq.7.5** is similar to that of **Eq.3.10**, which is given in Appendix II. Sl_{mi} is negative of Su_{mi}. A Fourier series expansion of **Eq.7.1** provides the far-field scattering pattern of the time modulated reflector array at any harmonic m ($m \neq 0$), as

$$F_m(\theta) = \sum_i^N [Eu_i(\theta)\, exp(ja_i) - El_i(\theta)\, exp(jb_i)] * Su_{mi} \quad \textbf{Eq.7.6}$$

Assume scattering patterns from lower and upper elements are identical and isotropic, $Eu_i(\theta) = El_i(\theta)$=1. **Eq.7.6** can be simplified as

$$F_m(\theta) = \sum_i^N \left[exp(ja_i) * \left(1 - \exp\left(jkd(1 + cos\,\theta)\right)\right)\right] * Su_{mi} \quad \textbf{Eq.7.7}$$

For the scattering pattern at the fundamental frequency,

$$F_0(\theta) = \sum_i^N exp(ja_i)\left(\tau_{ioff} - \tau_{ion}\right) + \exp(jb_i)\left(1 - \tau_{ioff} + \tau_{ion}\right)$$
$$= \sum_i^N (exp(ja_i) - \exp(jb_i))\left(\tau_{ioff} - \tau_{ion}\right) + \exp(jb_i) \quad \textbf{Eq.7.8}$$

7.3.1 Beam steering characteristics of double-layer TMRA

Apply the beam steering function to the double-layer TMRA. Assume the double-layer TMRA consists of 8 identical scattering elements. The distance between the front

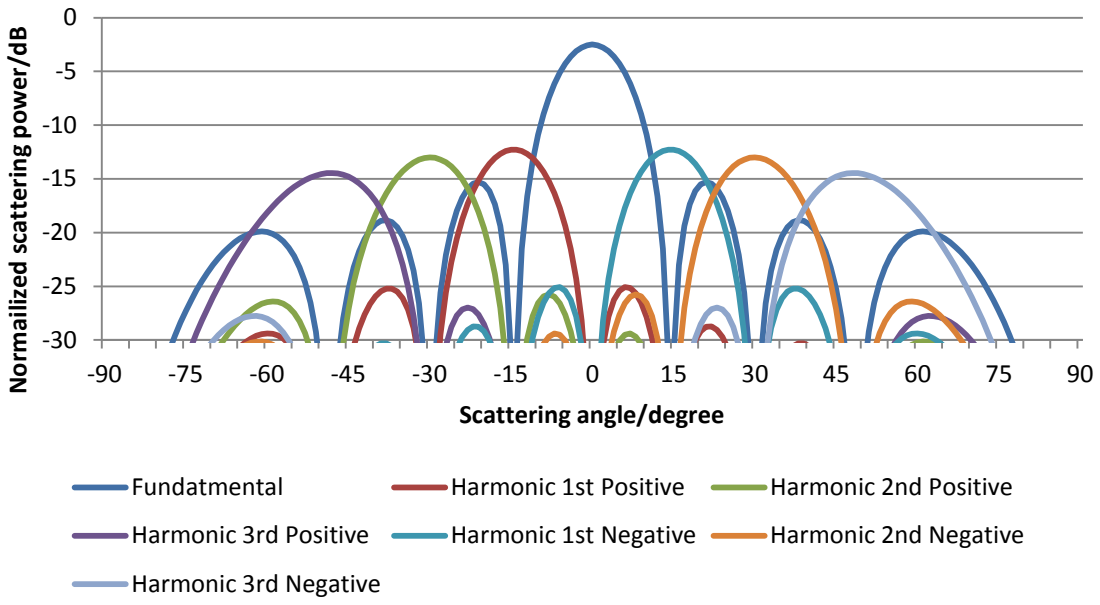

Fig.7.7 Scattering patterns of double layer TMRA conducting a beam steering function. The element-ON time is 0.125 duty cycle.

and back layers are half of the wavelength of fundamental/operating frequency. The inter-element coupling is not considered and elements are assumed to scatter isotropically.

Applying the original time sequence whose element-On time is 1/8 duty cycle to the double-layer TMRA, the beam steering functionality is re-produced. The formed patterns at fundamental and first three harmonics are calculated using **Eq.7.7** and **Eq.7.8** and shown in **Fig.7.7**. In **Fig.7.7**, the overall power level increase significantly comparing to the single layer using the same time sequence shown in **Fig.7.2**. However, the fundamental response is much higher than the harmonics.

To improve the power distribution, the simplest way is to change overall element-On time to re-locate the energy. We can use the same method in the single layer TMRA to draw the main beams' magnitudes of the fundamental and harmonic frequencies of the double-layer TMRA versus element-On time. The trends of main beam magnitudes are shown in **Fig.7.8**. Comparing to the trends of the single layer TMRA, double layer

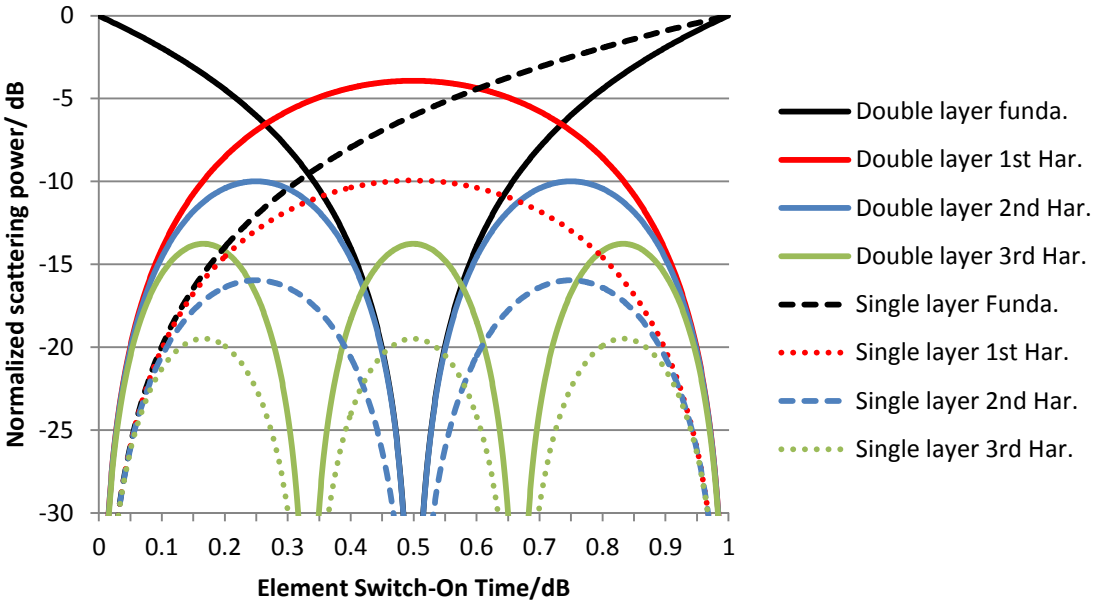

Fig.7.8 The main beam magnetudes of fundamental and harmonic scattering patterns of a double layer TMRA conducting beam steering vs. the element-On time.

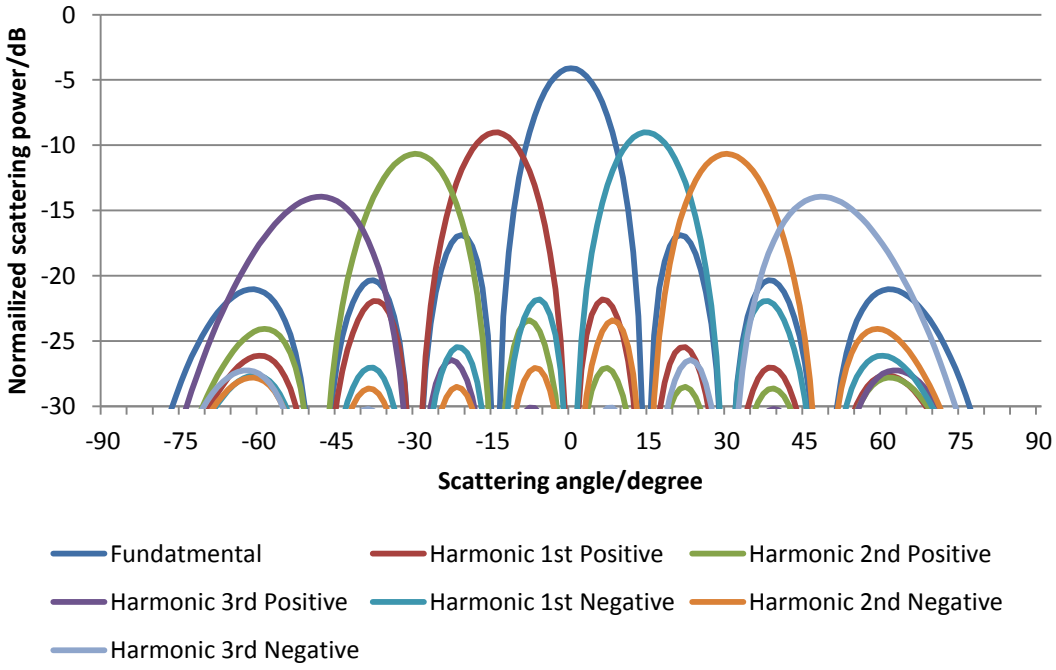

Fig.7.9 Scattering patterns of double layer TMRA conducting a beam steering function. The element-ON time is 18.8% duty cycle.

TMRA provide a significant increase in power. However, the trace of fundamental frequency changes its shape. This is due to the special two layer design. When the front

and the back layer scatter for the same amount of time, they cancel each other as the phase of the back layer is 180 degree opposite to the front layer (a round trip of quarter-wavelength layer distance). For the double layer TMRA, the switch-On time can be chosen as 0.188 or 0.812 duty cycle, where the overall output of the fundamental and harmonic peaks reaches their maximum value. Scattering patterns of double layer TMRA using such time sequence is shown in Fig. **7.9**.

7.3.2 Double-layer TMRA based on bow-tie dipole element

Let us examine a more realistic double-layer TMRA based on bow-tie dipole elements. Shown in **Fig.7.10**, the double-layer TMRA consists of a set of 8x2 linear bow-tie dipole reflector elements and a ground plane made of aluminium. Between the dipole

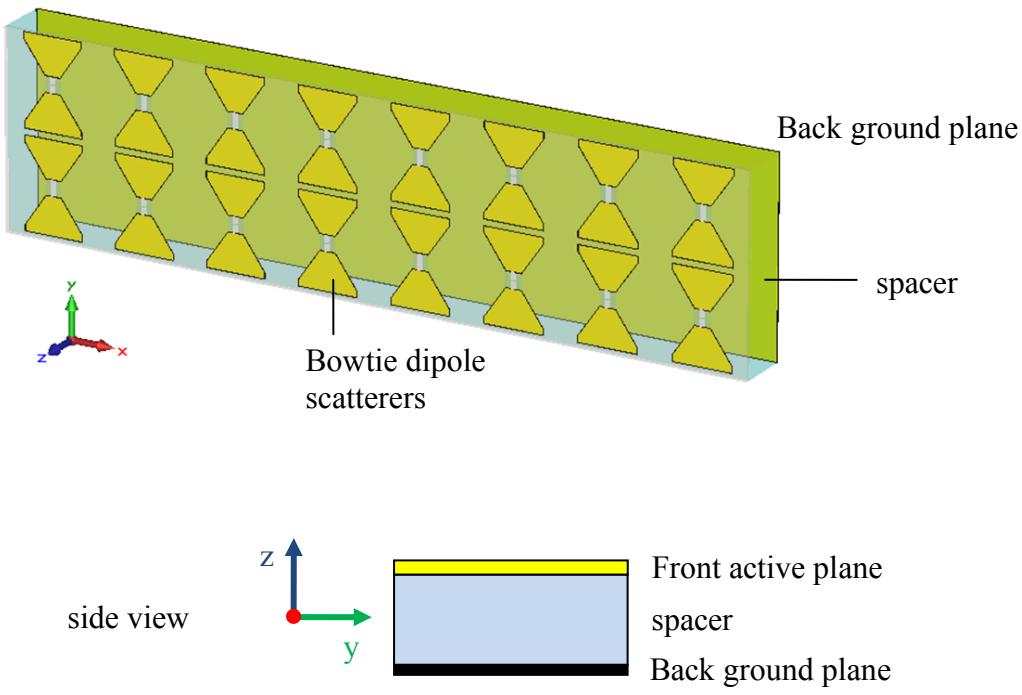

Fig.7.10 Model of a double-layer TMRA based on bowtie dipole elements. The TMRA consists of bowtie dipole scattering elements, a ground plane and a spacer.

reflectors and the ground plane, the material is Rhocell 51 (ε_r = 1.08, thickness = 7.5 mm), which is used as the spacer. The geometry of a single bowtie dipole is identical to the one used in single layer bowtie dipole TMRAs shown in **Fig.4.3**. PIN diodes ON/OFF states were represented by equivalent circuits with HIGH/LOW impedance. Two dipoles in a column formed a sub-array. Sub-arrays were controlled by external signals where the time modulating sequence applied.

However, for comparison purpose, an example of a single layer 8x2 TMRA is given. The single layer 8x2 TMRA was simulated by CST MICROWAVE STUDIO and Matlab using the approach in Section **4.3. Fig.7.11** shows the scattering patterns of the fundamental and harmonic responses of the single layer TMRA conducting beam forming using a progressive time sequence of a 12.5% duty cycle element-On time. The results are normalized to the peak scattering power of a ground-plane size copper plate simulated in

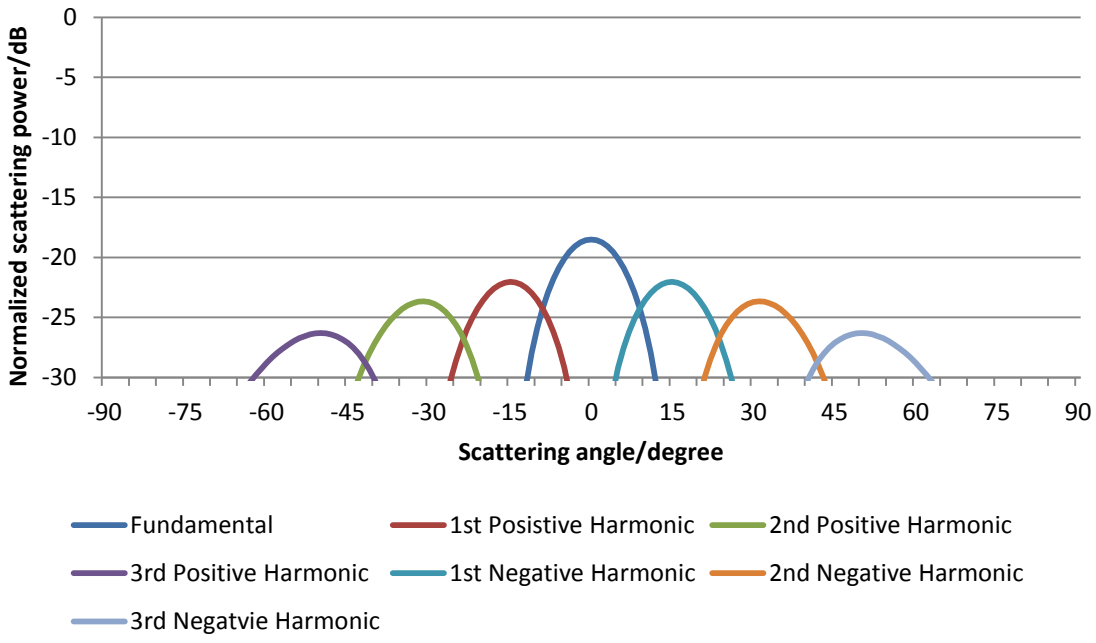

Fig.7.11 Scattering power patterns of an 8x2 single layer TMRA based on bowtie dipole element. The element-On time for the time sequence is 12.5% duty cycle.

CST MICROWAVE STUDIO under the same conditions. The magnitudes and position of fundamental and harmonic beams agree with the theoretic predictions in **Fig.7.2**.

The double-layer TMRA was simulated in the full-wave simulator CST Microwave studio. The excitation was a planewave, which illuminates from the broadside of the TMRA (z-axis). Farfield monitors were placed to record the embedded scattering power patterns. As the number of sub-arrays is eight, eight scattering power patterns $E_{t_1}(\theta)\ to\ E_{t_8}(\theta)$ were recorded while each pattern corresponds to the state when one element ON and the rest OFF. These patterns, same as ones of realistic TMRAs in Chapter 4, contains not only amplitude and phase information but also inter-element coupling effects. However, scattering from the ground plane is included in these embedded patterns.

Let the double-layer bowtie dipole TMRA be modulated by the original time sequence (12.5% duty cycle switch-On time) in **Fig.7.3**. Matlab was employed to calculate the scattering power patterns of harmonic frequencies using **Eq.4.2**. The fundamental frequency scattering pattern was predicated using the following formula,

$$\mathrm{F}_m(\theta) = \sum_{\mathrm{i}=1}^{8} \mathrm{E}_{\mathrm{t_i}}(\theta) * (\tau_{\mathrm{ioff}} - \tau_{\mathrm{ion}}) \qquad \textbf{Eq.7.9}$$

The scattering patterns of the fundamental and first three positive/negative harmonics of the proposed double-layer bowtie dipole TMRA are shown in **Fig.7.12a** and beam steering is successively re-produced at the fundamental and harmonic frequencies. It is noted that more energy is located at the fundamental frequency, which agrees with the theoretical predication in **Fig.7.7**. When the time sequence and increase element-On time is set at 0.188 duty cycle, the obtained scattering pattern (shown in **Fig.7.12b**) shows an improved power distributions at fundamental and harmonic frequencies. The results of the double-layer bowtie dipole TMRA agree with those of the double-layer ideal isotropic

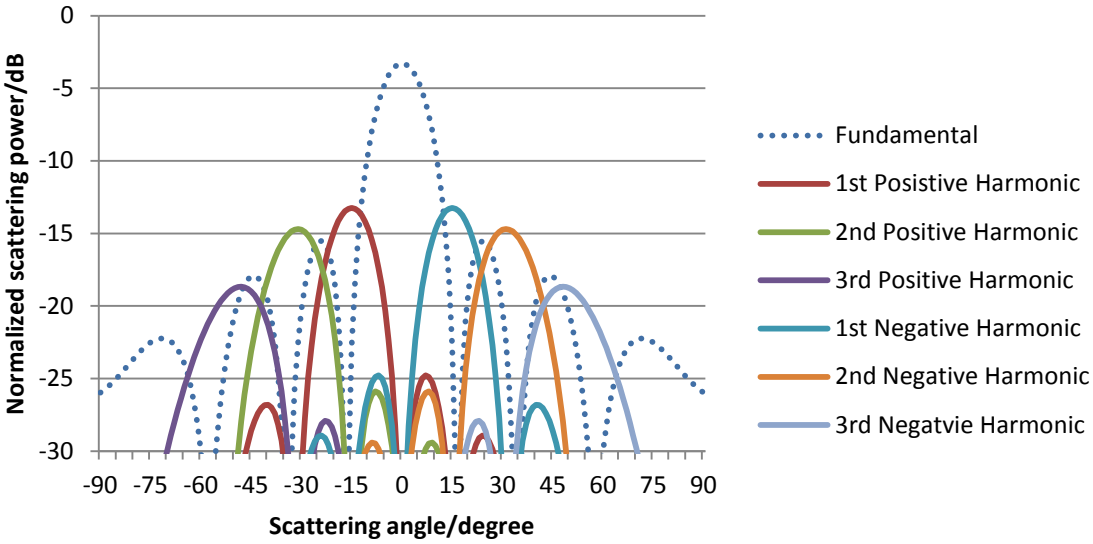

a. pulse width is 12.5% duty cycle.

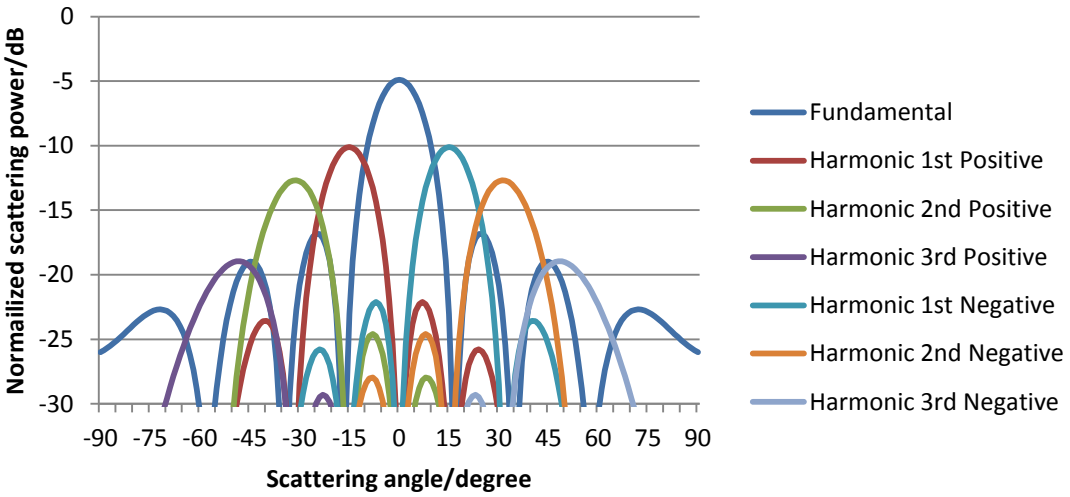

b. pulse width is 0.188 duty cycle.

Fig.7.12 Scattering power patterns of an 8x2 single layer TMRA based on bowtie dipole element with different pulse widths.

TMRA shown in **Fig.7.9**. The peak of the fundamental decreases by 2 dB while the peaks of 1st and 2nd harmonics increase by almost 3 dB and 2 dB respectively. The 3rd harmonic peak keeps at the same level.

7.4 Conclusion

This chapter discusses the power efficiency of TMRA systems'. Due to the special modulation scheme applied, the TMRA systems suffers power loss as the feeding wave transmits through the reflector elements when they are OFF. One way to improve the efficiency is to simply change the switch sequence and increase the element-On time. Another way is to use a double-layer TMRA. The double-layer TMRA consists of a front layer of reflector elements and a back ground plane. The element from the front layer and its corresponding element in the back plane operates alternatively as the switch of time. Thus at any instant, there is an element scattering the energy.

A simple model was built to explain the basic ideal of double-layer TMRA with numerical analysis based on array factor and Fourier series. The double-layer TMRA concept were further developed into a double-layer TMRA based on bow-tie dipole elements and Aluminium ground plane. CST Microwave studio was employed to examine the bowtie dipole double-layer TMRA. Both the results from ideal simplified model and the bowtie dipole model suggests that double-layer TMRA with an improved time sequence can significantly improve the total power efficiency.

Chapter 8 CONCLUSION AND DISCUSSION

8.1 Conclusion

This thesis introduces time modulated reflector arrays (TMRAs), which have been described, analyzed and demonstrated experimentally. The TMRA is based on a topology which is similar to that of a conventional reflectarray, but element time switching is used instead of element phasing to control the array radiation pattern. By controlling the elements switch on and off times, the TMRA is able to mimic the functions of conventional phased reflector arrays. Moreover, TMRA have been proved to provide additional function to steer the harmonic beams synchronously.

Chapter 3 introduces the concepts of the TMAs and TMRAs. Simple examples of TMAs and TMRAs based on ideal isotropic elements are analyzed using array factors and Fourier series theory. The operation mechanisms of TMAs and TMRAs are similar but TMRAs use a layout of reflectarrays, which consists of a feeding antenna and a grid of switch-controlled scattering elements. A TMRA based on isotropic elements exhibits similar characteristics to that of a conventional TMA with the same number of elements and switching sequence. TMRAs are also configured to perform beam steering and side lobe suppression functions.

Chapter 4 presents an experimental TMRA based on an array of PIN diode controlled bowtie dipole elements. The experimental TMRA was based on an array of PIN diode controlled bowtie dipole elements. The TMRA system was designed, constructed and simulated in a commercial full-wave electromagnetic simulator. Moreover, the bowtie dipole TMRA prototype has been made and measured in a

modified version of a NRL reflectivity measurement system. Measured data from the experimental TMRA confirms the operational functionality of the system. The prototype can conduct harmonic beam steering and locate the first three harmonic beams at the directions of 16°, 32° and 48° respectively.

In Chapter 5, TMRAs are shown to have the ability to conduct adaptive beamforming. MVDR beamforming and LCMV beamforming algorithms generates a complex weighting matrix, which can be used to allocate the maximum of the antenna array pattern in the desired direction while minimizing the responses in the angles of interference. TMRAs present an approach linking the weighting matrix calculated by beamforming formulas and the time switching sequence. By applying the weighting matrix using time sequences, TMRAs are able to form beams, which maximize the response in the desired direction and null in the directions of interferences or jammers. Both MVDR and LCMV approaches have been verified both on isotropic element TMRAs and realistic bowtie dipole TMRAs. The results suggest that TMRAs can conduct the adaptive beamforming algorithms at lower level harmonic frequencies.

Chapter 6 introduces the parabolic TMRA, which consists of a grid of scattering elements which lay a parabola and the feeding antenna placed at the focus of the parabola. Parabolic TMRAs are designed for the situation when the feeding antenna TMRAs are placed in a close distance. The ideal of the parabolic TMRA has been verified by an ideal example based on isotropic scattering elements and a realistic model based on bowtie dipole sub-arrays. Both of examples suggest that parabolic TMRAs are able to conduct basic beam steering and beamforming functions. However, the form pattern shapes generated by the beam-steering time sequence became distorted when the feeding source was placed very close to the reflector elements. This is because of the phase differences between the element feeding paths. But the MVDR beam forming function was perfectly

deployed in parabolic TMRAs as the feeding path differences can be compensated for the beamforming algorithm.

Chapter 7 discusses efficiency of the TMRA. In TMAs, the power allocated in the sidebands (harmonic frequencies) due to the periodically time modulation affects the system efficiency. In addition conventional TMRAs, which consist of single layer reconfigurable elements, suffers energy loss due to the wasted energy when the scattering element is OFF (non-scattering). The proposed double-layer TMRA aims to increase the overall system performance using an additional scattering layer and a modified time sequence. Double layer TMRAs add a second layer of elements, which scatter when first layer elements are OFF. The double-layer TMRA is explained using a simple theoretical model. A realistic bowtie dipole two-layer TMRA is then analysed in a full wave simulation. The performance of a double-layer TMRA conducting a beam steering function is carried out and compared with that of a single layer TMRA.

8.2 Novelty and discussions

8.2.1 Initiative

This is first time in the researchers' community in which the time-modulation method has been applied to reflectarrays. Time modulated or time switched arrays have been a popular topic for over a decade. Introducing time as a new dimension in the antenna arrays allows many of the beamforming functions associated with conventional phased arrays, such as beam steering, direction finding and adaptive nulling to be realised without the need for phase shifters. Scientists from all over the world have focused the research on the time modulated arrays, which require a complex feeding network. The TMRAs proposed in this thesis have reproduced identical functions without the need for

complex feeding network. TMRAs provide a good alternative to TMA systems and bring a new way of managing the scattering patterns for reflectarrays.

8.2.2 Inter-element coupling

The inter-element coupling in antenna arrays is always a challenge for researchers. Scientists have tried different means to predicate and compensate mutual couplings [**98**] [**99**]. In [**100**], S. Yang and Z. Nie uses optimized time sequence to compensate mutual coupling in a TMA. They have successfully realized a -30 dB Taylor sidelobe suppression on a 16 element TMA. In this thesis, the ground work for introducing TMRAs is based on presumed isotropic elements without mutual coupling. Such assumptions are un-realistic in antenna design. A more practical TMRA based on bowtie dipole elements has been proposed. When designing the bowtie dipole TMRA prototype, CST Microwave studio has been employed to simulate the bowtie dipole TMRA performance including the effects of inter-element coupling. This is a good way to examine and investigate mutual coupling before a prototype is made.

In the beamforming section, inter-element coupling was considered as prior knowledge. CST Microwave studio calculated the embedded patterns including antenna array amplitude, phase components and inter-element coupling. The patterns were put into MVDR/LCMV beamforming formulas alone with other prior knowledge such as elements' scattering patterns, positions and phase differences. Hence TMRAs understand the existence of such effects and compensate for them when calculating the weight matrices and time sequences.

8.2.3 Cost and system complexity

Although adaptive phased array antenna systems provide supreme functionality of antenna beamforming and null steering, their applications have been limited because of

high manufacturing costs and their complex system configuration. In the last two decades, scientists were trying to explore its commercial usage in cellular base stations of mobile communication systems [**101**] [**102**] [**103**]. However, it is still very hard to find their application in other areas of mobile communication, for instance the end-user terminals. Furthermore, the cost of the system significantly increases as the number of antenna elements increases. This is because each of the elements requires an identical set of high-gain/low-noise amplifiers and a phase shift unit. This would result in large system volume, high power consumption, high system complexity and high producing costs.

The TMRA systems, on the other hand, uses PIN diodes without need of phase shift units. The price of one PIN diode is 1/500 or even 1/1000 of the phase shift unit. Moreover, as the system only has one feed port, TMRAs do not require an additional RF amplifier and feeding network. Increasing the number of TMRA element only requires the addition of switching control circuits. TMRAs thus are simpler and cheaper way compared to phased arrays.

8.2.4 Millimetre-wave frequency applications

Efficiency of phased arrays decreases dramatically at millimetre-wave frequencies. This is mainly because of the use of transmission lines in the feeding networks become significantly lossy at higher frequencies. Reflectarrays, which are the hybrid of aperture antennas and antenna arrays, have a great advantage in efficiency as they do not need the lossy feeding network and can steer the antenna beam using active components.

TMRAs have the same benefits as reflectarrays as they also do not need the feeding lines. This makes TMRAs the best option from the TMAs family in the millimetre-wave applications.

8.3 Future work

This part of the research was mainly focused on the concept and description of time-modulated reflector-arrays along with their basic functions to steer the beam and form scattering patterns. The outcomes and results suggest the TMRAs are in their initial stage and future investigations need to be carried out to further explore and improve their performance and functionality.

In Chapter 4, a realistic bowtie dipole TMRA prototype was built and tested. Although the TMRA prototype performed satisfactorily, the results suggest PIN diode switches (Siemens BA585) suffers time delays when the switch duty cycles are relatively small. This part of the work can be improved in the future by

- Taking the time delay as a factor when calculating the time sequence.
- Finding alternative switches with less time delay.

Sequentially, research efforts could be put into realising advanced modulation schemes using TMRAs. As the TMRAs are able to conduct adaptive beamforming, they could guide the propagation direction of the signal and conduct a direction dependent modulation [**104**]. Furthermore, the concept of orbital angular momentum, which although widely used in optical communications [**105**] is new to the area of microwave communications [**106**] [**107**], could be realised using a circular TMRA.

Finally, as stated in the beginning, TMRAs are still at their initial stages. Work need to done to improve their performance, robustness and functionality. Beside bowtie dipoles, TMRAs should try other shapes of scatterers such as squares, ring, and aperture. Circular polarization and the dual polarization will be practised using TMRAs. The theoretical analysis of TMRAs have approved the feasibility of adaptive beamforming based on TMRAs. A TMRA prototype including an adaptive beamforming system is in the future research plan. Furthermore, a measurement system designed for TMRAs

instead of the NRL arch will benefit the future research. The TMRAs based on PIN diodes have proven the functionality of TMRAs. Finally, mm-wavelength TMRAs, which operate at THz frequency band, will be feasible if fabrication and measurement system is solved. As the developing of meta-material technology, photo-conductive material, ferro-electric films, graphene will be used in the THz TMRAs. In conclusion, TMRAs still need the research community to explore. It is very glad to see more research outcome of TMRAs appears in the future.

REFERENCES

[1] H. Shanks and R. W. Bickmore, "Four-dimensional electromagnetic radiators," *Can. J. Phys.*, vol. 37, no. (3), pp. 263–275, 1959.

[2] W. H. Kummer, A. T. Villeneuve, T. Fong, and F. Terrio, "Ultra-low sidelobes from time-modulated arrays," *IEEE Tran. Antennas and Propagat.*, vol. 11, no. 5, pp. 633-639, 1963.

[3] J. C. Bregains, J. Fondevila-Gomez, G. Franceschetti, and F. Ares, "Signal radiation and power losses of time-modulated arrays," *IEEE Trans. on Antennas and Propag.*, vol. 56, no. 6, pp. 1799-1804, 2008.

[4] L. Poli, P. Rocca, L. Manica, and A. Massa, "Handling sideband radiations in time-modulated arrays through particle swarm optimization," *IEEE Trans. on Antennas and Propag.*, vol. 58, no. 4, pp. 1408-1411, 2010.

[5] S. Yang, Y. B. Gan, A. Qing, and P. K. Tan, "Design of a uniform amplitude time modulated linear array with optimized time sequences," *IEEE Trans. Antennas and Propag.*, vol. 53, no. 6, pp. 2337-2339, Jul. 2005.

[6] L. Poli, P. Rocca, and A. Massa, "Sideband radiation reduction exploiting pattern multiplication in directive time-modulated linear array," *IET Microw. Antennas & Propag.*, vol. 6, no. 2, pp. 214-222, 2012.

[7] Y. Tong and A. Tennant, "Reduced Sideband Levels in Time-Modulated Arrays Using Half-Power Sub-Arraying Techniques," *Antennas and Propagation, IEEE Transactions on*, vol. 59, no. 1, pp. 301-303, Jan. 2011.

[8] Y. Tong, A. Tennant, and R.J. Langley, "Beam steering techniques for time-switched arrays," in *Antennas & Propagation Conference*, Loughborough, NOV. 2009, pp. 223-236.

[9] G. Li, S. Yang, and Z. P. Nie, "A hybrid analog-digital adaptive beamforming in time-modulated linear arrays," *Electromagnetics*, vol. 30, no. 4, pp. 364-365, May 2010.

[10] P. Rocca, L. Poli, G. Oliveri, and A. Massa, "Adaptive Nulling in Time-Varying Scenarios Through Time-Modulated Linear Arrays," *Antennas and Wireless Propagation Letters, IEEE*, vol. 11, pp. 101-104, 2012.

[11] G. Li, S. Yang, and Z. P. Nie, "Direction of arrival estimation in time modulated antenna arrays with unidirectional phase center motion," *Antennas and Propagation, IEEE Transactions on*, vol. 58, no. 4, pp. 1105-1111, Apr. 2010.

[12] A. Tennant, "Experimental two-element time-modulated direction finding array," *IEEE Trans. on Antennas and Propag.*, vol. 58, no. 3, pp. 986-988, Mar. 2010.

[13] Y. Tong and A. Tennant, "A Two-Channel Time Modulated Linear Array With Adaptive Beamforming," *Antennas and Propagation, IEEE Transactions on*, vol.

60, no. 1, pp. 141-147, Jan. 2012.

[14] H.F. Abu Tarboush et al., "A Reconfigurable Wideband and Multiband Antenna Using Dual-Patch Elements for Compact Wireless Devices," *Antennas and Propagation, IEEE Transactions on*, vol. 60, no. 1, pp. 36-43, Jan. 2012.

[15] E. Bruce and A. C. Beck, "Experiments with Directivity Steering for Fading Reduction," *Radio Engineers, Proceedings of the Institute of*, vol. 23, no. 4, pp. 357-371, April 1935.

[16] J. Condon. (2013, Dec) NRAO. [Online]. http://www.cv.nrao.edu/course/astr534/RadioTelescopes.html

[17] J. R. Ford, I. D. Kruger, and H. Perkel, "Rotating radar antenna," US 2947989 A, Nov. 28, 1956.

[18] R. L. Haupt and M. Lanagan, "Reconfigurable Antennas," *Antennas and Propagation Magazine, IEEE*, vol. 55, no. 1, pp. 49-61, Feb. 2013.

[19] Wikipedia. (2014, July) Wikipedia. [Online]. http://en.wikipedia.org/wiki/RF_MEMS

[20] M. Safari, C. Shafai, and L. Shafai, "X-Band Tunable Frequency Selective Surface Using MEMS Capacitive Loads," *Antennas and Propagation, IEEE Transactions on* , vol. 63, no. 3, pp. 1014-1021, March 2015.

[21] G. I. Kiani, T. S. Bird, and K. Y. Chan, "MEMS enabled frequency selective surface for 60 GHz applications," in *Antennas and Propagation (APSURSI), 2011 IEEE International Symposium on*, 2011, pp. 2268-2269.

[22] D. Anagnostou, M. Khodier, J. C. Lyke, and C. G. Christodoulou, "Fractal antenna with RF MEMS switches for multiple frequency applications," in *IEEE Antennas and Propagation Society International Symposium*, San Antonio, 2002, pp. 22-25.

[23] T. Debogovic and J. Perruisseau-Carrier, "Low Loss MEMS-Reconfigurable 1-Bit Reflectarray Cell With Dual-Linear Polarization," *Antennas and Propagation, IEEE Transactions on*, vol. 62, no. 10, pp. 5055-5060, Oct. 2014.

[24] G. Wang, T. Polley, A. Hunt, and J. Papapolymerou, "A high performance tunable RF MEMS switch using barium strontium titanate (BST) dielectrics for reconfigurable antennas and phased arrays," *Antennas and Wireless Propagation Letters, IEEE*, vol. 4, pp. 217-220, 2005.

[25] Y. Dai, H. Sun, P. Li, and H. Yin, "Design of a millimeter-wave MEMS antenna array," in *Antennas and Propagation (APCAP), 2012 IEEE Asia-Pacific Conference on*, 2012, pp. 55-56.

[26] W. Gautier et al., "Hybrid Integrated RF-MEMS Phased Array Antenna at 10GHz," in *Microwave Conference, 2008. EuMC 2008. 38th European* , 2008, pp. 139-142.

[27] C. Guclu, J. Perruisseau-Carrier, and O. Civi, "Proof of concept of a dual-band circularly-polarized RF MEMS beam-switching reflectarray," *IEEE Trans.Antennas Propag.*, vol. 60, no. 11, pp. 5451 -5455, 2012.

[28] H. Legay et al., "A steerable reflectarray antenna with MEMS controls," in *Phased*

Array Systems and Technology, 2003. IEEE International Symposium on , OCT. 2003, pp. 494-499.

[29] T. Aboufoul, A. Alomainy, and C. Parini, "Reconfiguring UWB Monopole Antenna for Cognitive Radio Applications Using GaAs FET Switches," *Antennas and Wireless Propagation Letters, IEEE*, vol. 11, pp. 392-394, 2012.

[30] L.N. Pringle et al., "A reconfigurable aperture antenna based on switched links between electrically small metallic patches," *Antennas and Propagation, IEEE Transactions on* , vol. 52, no. 6, pp. 1434-1445, Jun 2004.

[31] Microsemi-Watertown, *The PIN diode circuit designers' handbook*. Watertown: Micrcosemi Corp., 1998.

[32] S. Nikolaou et al., "Pattern and frequency reconfigurable annular slot antenna using PIN diodes," *Antennas and Propagation, IEEE Transactions on*, vol. 54, no. 2, pp. 439-448, Feb. 2006.

[33] J. Lim, G. Back, Y. Ko, C. Song, and T. Yun, "A Reconfigurable PIFA Using a Switchable PIN-Diode and a Fine-Tuning Varactor for USPCS/WCDMA/m-WiMAX/WLAN," *Antennas and Propagation, IEEE Transactions on*, vol. 58, no. 7, pp. 2404-2411, July 2010.

[34] P. D. Grant, M. W. Denhoff, and R. R. Mansour, "A Comparison between RF MEMS Switches and Semiconductor Switches," in *Proceedings of the 2004 International Conference on MEMS, NANO and Smart Systems*, 2004, pp. 515-521.

[35] Sanyo Semicon Device. (2014, Feb.) SVC704 Datasheet. PDF. [Online]. http://pdf1.alldatasheet.com/datasheet-pdf/view/200901/SANYO/SVC704.html

[36] N. Behdad and K. Sarabandi, "A varactor-tuned dual-band slot antenna," *Antennas and Propagation, IEEE Transactions on* , vol. 54, no. 2, pp. 401-408, Feb 2006.

[37] S.V. Hum, M. Okoniewski, and R. J. Davies, "Modeling and Design of Electronically Tunable Reflectarrays," *Antennas and Propagation, IEEE Transactions on*, vol. 55, no. 8, pp. 2200-2210, Aug. 2007.

[38] P. Qin, A.R. Weily, Y.J. Guo, T.S. Bird, and Chang-Hong L., "Frequency Reconfigurable Quasi-Yagi Folded Dipole Antenna," *Antennas and Propagation, IEEE Transactions on*, vol. 58, no. 8, pp. 2742-2747, Aug. 2010.

[39] L. Zhang, F. Yang, and A.Z. Elsherbeni, "Analysis and design of a reconfigurable dual-strip scanning antenna," in *Antennas and Propagation Society International Symposium, 2009. APSURSI '09*, 2009.

[40] J. Valasek, "Piezo-Electric and Allied Phenomena in Rochelle Salt," *Physical Review Letters,* no. 17, pp. 475-481, Apr. 1921.

[41] L. Yan et al., "Ba0.5Sr0.5TiO3–Bi1.5Zn1.0Nb1.5O7 composite thin films with promising microwave dielectric properties for microwave device applications," *Applied Physics Letters* , vol. 85, no. 16, pp. 3522-3524, 2004.

[42] S. S. Gevorgian and E. L. Kollberg, "Do we really need ferroelectrics in paraelectric phase only in electrically controlled microwave devices?," *Microwave Theory and Techniques, IEEE Transactions on*, vol. 49, no. 11, pp. 2117-2124,

2002.

[43] S. W. Liu et al., "High-dielectric-tunability of ferroelectric (Pb,Sr)TiO3 thin films on (001) LaAlO3," *Applied Physics Letters*, vol. 85, no. 15, pp. 3202-3204, OCT. 2004.

[44] Y. Yashchyshyn and J.W. Modelski, "Rigorous analysis and investigations of the scan antennas on a ferroelectric substrate," *Microwave Theory and Techniques, IEEE Transactions on*, vol. 53, no. 2, pp. 427-438, 2005.

[45] R.R. Romanofsky, "Advances in Scanning Reflectarray Antennas Based on Ferroelectric Thin-Film Phase Shifters for Deep-Space Communications," *Proceedings of the IEEE* , vol. 95, no. 10, pp. 1968-1975, Oct. 2007.

[46] M. R. Chaharmir, J. Shaker, M. Cuhaci, and A. Sebak, "Novel photonically-controlled reflectarray antenna," *Antennas and Propagation, IEEE Transactions on*, vol. 54, no. 5, pp. 1134-1141, April 2006.

[47] S. Bildik et al., "Reconfigurable liquid crystal reflectarray with extended tunable phase range," in *Radar Conference (EuRAD), 2011 European*, Oct. 2011, pp. 404-407.

[48] G. Perez-Palomino, J.A. Encinar, M. Barba, and E. Carrasco, "Design and evaluation of multi-resonant unit cells based on liquid crystals for reconfigurable reflectarrays," *Microwaves, Antennas & Propagation, IET*, vol. 6, no. 3, pp. 348-354, Dec. 2012.

[49] R. Marin, A. Moessinger, F. Goelden, S. Mueller, and R. Jakoby, "77 GHz Reconfigurable Reflectarray with Nematic Liquid Crystal," in *Antennas and Propagation, EuCAP 2007*, 2007, pp. 1-5.

[50] G. K. Geim and K. S. Novoselov, "The rise of graphene," *Nature Materials*, vol. 6, no. 183, 2007.

[51] E. Carrasco, M. Tamagnone, and J. Perruisseau-Carrier, "Tunable Graphene Reflective Cells for THz Reflectarrays and Generalized Law of Reflection," *Applied Physics Letters*, vol. 102, no. 10, pp. 103-104, 2013.

[52] X. Zhu, L. Wu, Y. Guo, and W. Wu, "Tunable graphene FSS for terahertz applications," in *Antennas and Propagation Society International Symposium (APSURSI) IEEE*, 2014, pp. 2104-2105.

[53] C. Cheng, B. Lakshminarayanan, and A. Abbaspour-Tamijani, "A Programmable Lens-Array Antenna With Monolithically Integrated MEMS Switches," *Microwave Theory and Techniques, IEEE Transactions on*, vol. 57, no. 8, pp. 1874-1884, 2009.

[54] C. A. Balanis, *Antenna Theory*. New Jersey: John Wiley & Sons, 2005.

[55] C. A. Balanis, "Arrays: Linear, Planar, and Circular," in *Antenna Theory*. New Jersey: Wiley, 2005, pp. 283-371.

[56] F. Nicholas, *Advanced Array Systems, Applications and RF Technologies*. London: Academic Press, 2000.

[57] K. F. Braun. (1909, Dec) Electrical oscillations and wireless telegraphy. [Online]. http://www.nobelprize.org/nobel_prizes/physics/laureates/1909/braun-lecture.pdf

[58] S. Jeon, Y. Kim, and D. Oh, "A new active phased array antenna for mobile direct broadcasting satellite reception," *Broadcasting, IEEE Transactions on*, vol. 46, no. 1, pp. 36-40, 2000.

[59] R. Schulze, R.E. Wallis, R.K. Stilwell, and Cheng Weilun, "Enabling Antenna Systems for Extreme Deep-Space Mission Applications," *Proceedings of the IEEE* , vol. 95, no. 10, pp. 1976-1985, 2007.

[60] G. Zhang et al., "Phased Array Radar Polarimetry for Weather Sensing: A Theoretical Formulation for Bias Corrections," *Geoscience and Remote Sensing, IEEE Transactions on*, vol. 47, no. 11, pp. 3679-3689, 2009.

[61] S. P. Stapleton and G. S. Quon, "A cellular base station phased array antenna system," in *Vehicular Technology Conference, 1993.*, 1993, pp. 93-96.

[62] H. L. Van Trees, *Optimum Array Processing: Part IV of Detection, Estimation, and Modulation Theory*. New York: Wiley, 2002.

[63] B. Allen and M. Ghavami, *Adaptive Array Systems Fundamentals and applticatio*ns. Chichester: John Wiley & Sons, 2005.

[64] H. Kamoda, T. Iwasaki, J. Tsumochi, T. Kuki, and O., Hashimoto, "60-GHz Electronically Reconfigurable Large Reflectarray Using Single-Bit Phase Shifters," *Antennas and Propagation, IEEE Transactions on*, vol. 59, no. 7, pp. 2524-2531, July 2011.

[65] J. Perruisseau-Carrier and A. K. Skriverviky, "Monolithic MEMS-based reflectarray cell digitally reconfigurable over a 360 degree phase range," *IEEE Antennas Wireless Propag. Lett.*, vol. 7, pp. 138-141, 2008.

[66] S. V. Hum and J., Perruisseau-Carrier, "Reconfigurable Reflectarrays and Array Lenses for Dynamic Antenna Beam Control: A Review," *Antennas and Propagation, IEEE Transactions on*, vol. 62, no. 1, pp. 183-198, Jan. 2014.

[67] D. M. Pozar, S. D. Targonski, and H.D. Syrigos, "Design of millimeter wave microstrip reflectarrays," *IEEE Trans. Antennas Propag.*, vol. 45, no. 2, pp. 287-296, 1997.

[68] M. R. Chaharmir, J. Shaker, M. Cuhaci, and A. Sebak, "Reflectarray with variable slots on groundplane," *Inst. Elect. Eng. Proc. Microwaves Antennas Propag.,* vol. 150, no. 6, pp. 436-439, 2003.

[69] J. Huang and R. J., Pogorzelski, "A Ka-band microstrip reflectarraywith elements having variable rotation angles," *IEEE Trans. Antennas Propag.*, vol. 46, no. 5, pp. 650 -656, 1998.

[70] K. H. Sayidmarie and M. E. Bialkowski, "Investigations into phase characteristicsof a single-layer reflectarray employing patch or ring elements of variablesize," *IEEE Trans. Antennas Propag.*, vol. 56, no. 11, pp. 3366 -3372, 2008.

[71] M. Bozzi, S. Germani, and L. Perregrini, "Performance comparison of differentelement shapes used in printed reflectarrays," *IEEE Antennas Wireless Propag. Lett.*, vol. 2, no. 1, pp. 219 -222, 2003.

[72] J. Rodriguez-Zamudio, J.I. Martinez-Lopez, J. Rodriguez-Cuevas, and A.E., Martynyuk, "Reconfigurable reflectarraysbased on optimized spiraphase-type elements," *IEEETrans. Antennas Propag.*, vol. 60, no. 4, pp. 1821-1830, 2012.

[73] J. Perruisseau-Carrier and P. Pardo, "Unit cells for dual-polarized and polarization-flexiblereflectarrays with scanning capabilities," in *Proc.Eur. Conf. Antennas Propag. (EuCAP2009)*, 2009.

[74] Z. Chen, J. Liu, and L. Li, "Design of scalable beam steering system of phased array radar," in *Radar (Radar), 2011 IEEE CIE International Conference on*, 2001, pp. 1153,1156.

[75] B. Pueo, J. Escolano, and M. Roma, "Precise control of beam direction and beamwidth of linear loudspeaker arrays," in *Sensor Array and Multichannel Signal Processing Workshop Proceedings, 2004 ,* July 2014, pp. 538-541.

[76] H. Kosaka et al., "Photonic crystals for micro lightwave circuits using wavelength-dependent angular beam steering," *Appl. Phys. Lett.*, vol. 74, no. 10, pp. 1370-1372, 1999.

[77] J. Liu, A. B. Gershman, Z. Luo, and K. M. Wong, "Adaptive beamforming with sidelobe control using second-order cone programming," in *Sensor Array and Multichannel Signal Processing Workshop Proceedings, 2002*, Aug. 2002, pp. 461-464.

[78] H.R. Ward, "Properties of Dolph-Chebyshev Weighting Functions," *Aerospace and Electronic Systems, IEEE Transactions on*, vol. AES-9, no. 5, pp. 785-786, Sep. 1973.

[79] Y. Wang, A. Tennant, and R. J. Langley, "A phase modulated RF tag," in *Loughborough Antenna and Propagation Conference*, Loughborough, 2011.

[80] Arduino. (2012, May) Arduino UNO. [Online]. http://www.arduino.cc/

[81] Siemens, "BA 585 Data Sheet," Semiconductor Group, Data Sheet 1994.

[82] R. D. Jones and Jr. W. E. Doherty. (1998) PIN diode circuit designer handbook. Online. [Online]. http://www.ieee.li/pdf/pin diode handbook.pdf

[83] SGS-Thomson Microelectronics, "2N2369 High Frequency Saturated Switch Data Sheet," Data Sheet 1989.

[84] CST. CST. [Online]. http://www.cst.com

[85] S.W. Varade, "Robust Algorithms for DOA Estimation and Adaptive Beamforming for Smart Antenna Application," in *Emerging Trends in Engineering and Technology (ICETET), 2009 2nd International Conference on*, Nagpur, 2009, pp. 1195 - 1200.

[86] D. Ezri, "The impact of synchronization on receive beamforming with null steering in OFDM MIMO systems," in *Electrical & Electronics Engineers in Israel*

(IEEEI), 2012 IEEE 27th Convention of, Eilat, 2012, pp. 1-4.

[87] H. H. Chen, S. C. Chan, and K. L. Ho, "Adaptive Beamforming Using Frequency Invariant Uniform Concentric Circular Arrays," *Circuits and Systems I: Regular Papers, IEEE Transactions on*, vol. 54, no. 9, pp. 1938-1949, Sep. 2007.

[88] V.O. Joseph, "Design and implementation of a novel real time target tracking scheme for passive SONARs using MVDR beam forming and Kalman filtering," in *Ocean Electronics (SYMPOL), 2009 International Symposium on*, Cochin, 2009, pp. 23 - 29.

[89] Y. Wang and A. Tennant, "MVDR beamforming applied to a time-modulated reflector-array," in *Antennas and Propagation Conference (LAPC)*, Loughborough, 2013, pp. 591-594.

[90] Y. Wang and A. Tennant, "LCMV beamforming applied to a time-modulated reflector-array: Concept and simulations," in *Microwave, Antenna, Propagation and EMC Technologies for Wireless Communications (MAPE), 2013 IEEE 5th International Symposium on*, Chengdu, 2013, pp. 338-342.

[91] B.D. Van Veen and K.M. Buckley, "Beamforming: a versatile approach to spatial filtering," *ASSP Magazine, IEEE*, vol. 5, no. 2, pp. 4-24, April 1988.

[92] J. Capon, "High-resolution frequency-wavenumber spectrum analysis," *Proc. IEEE*, pp. 1408-1418, Aug 1969.

[93] H. L. Van Trees, "Optimum waveform estimation," in *Detection, Estimation, and Modulation Theory: Part IV Optimum Array Processing*. New York: Wiley, 2002, pp. 440-445.

[94] Y. Wang and A. Tennant, "Time-modulated reflector array," *Electronics Letters*, vol. 48, no. 16, pp. 972-974, 2012.

[95] H. Rajagopalan and Y., Rahmat-Samii, "Dielectric and Conductor Loss Quantification for Microstrip Reflectarray: Simulations and Measurements," *Antennas and Propagation, IEEE Transactions on*, vol. 56, no. 4, pp. 1192-1196, 2008.

[96] J. A. Zornoza and M.E. Bialkowski, "Design of a shaped beam multi-layer microstrip reflectarray with Australia and New Zealand coverage pattern," in *Phased Array Systems and Technology, 2003. IEEE International Symposium on*, 2003, pp. 488-493.

[97] J. A. Encinar and J. A. Zornoza, "Three-layer printed reflectarrays for contoured beam space applications," *Antennas and Propagation, IEEE Transactions on*, vol. 52, no. 5, pp. 1138,1148, May 2004.

[98] A.H. Mohammadian, S.S. Soliman, M.A. Tassoudji, and L. Golovanevsky, "A Closed-Form Method for Predicting Mutual Coupling Between Base-Station Dipole Arrays," *Vehicular Technology, IEEE Transactions on*, vol. 56, no. 3, pp. 1088-1099, May 2007.

[99] H. Lui, H. T. Hui, and M. Leong, "A Note on the Mutual-Coupling Problems in Transmitting and Receiving Antenna Arrays," *Antennas and Propagation*

Magazine, IEEE, vol. 51, no. 5, pp. 171-176, Oct. 2009.

[100] S. Yang and Z. Nie, "Mutual coupling compensation in time modulated linear antenna arrays," *Antennas and Propagation, IEEE Transactions on*, vol. 53, no. 12, pp. 4182-4185, Dec 2005.

[101] S. Anderson, M. Millnert, M. Viberg, and B. Wahlberg, "An adaptive array for mobile communication systems," *Vehicular Technology, IEEE Transactions on*, vol. 40, no. 1, pp. 230-236, Feb. 1991.

[102] V. Genc, S. Murphy, Y. Yu, and J. Murphy, "IEEE 802.16j Relay-based Wireless Access Networks: An Overview," *IEEE Wireless Communications Magazine, Special Issue on Recent Advances and Evolution of WLAN and WMAN Standards*, 2008.

[103] Y. H. Chen, J. Chen, P. C. Hsien, D. Chang, and J. Huang, "Performance evaluation of mobile WiMAX beam forming network implemented by RF digital step attenuators," in *14th European Wireless Conference*, 2008, pp. 1-6.

[104] Y. Wang, A. Tennant, and R. J. Langley, "Direction Dependent Modulation of a RFID Tag," in *EuCap*, 2012.

[105] Y. Yue et al., "Mode Properties and Propagation Effects of Optical Orbital Angular Momentum (OAM) Modes in a Ring Fiber," *Photonics Journal, IEEE*, vol. 4, no. 2, pp. 535-543, April 2012.

[106] A. Tennant and B. Allen, "Generation of radio frequency OAM radiation modes using circular time-switched and phased array antennas," in *Antennas and Propagation Conference (LAPC), 2012*, Loughborough, 2012, pp. 1-4.

[107] O. Edfors and A. J. Johansson, "Is Orbital Angular Momentum (OAM) Based Radio Communication an Unexploited Area?," *Antennas and Propagation, IEEE Transactions on*, vol. 60, no. 2, pp. 1126-1131, Feb. 2012.

APPENDEX I MATLAB CODING

NOT INCLUDED IN THE ELECTRONIC VERSION OF THE THESIS

APENDEX II FORMULAS DERIVATIONS

- Derive **Eq.3.10** from **Eq.3.7** and **Eq.3.9** .

Given that,

$$s_{im} = \frac{1}{T_0}\int_0^{T_0} I_i(t)\, e^{-jm\frac{2\pi}{T_0}t} dt \qquad \textbf{Eq.3.9}$$

$$I_i(t) = \begin{cases} 1, & nT_0 + t_{ion} \le t < nT_0 + t_{ioff} \\ 0, & others \end{cases} \qquad \textbf{Eq.3.7}$$

Substitute $I_i(t)$ in **Eq.3.9** using **Eq.3.7**

$$s_{im} = \frac{1}{T_0}\int_{t_{ion}}^{t_{ioff}} 1 * e^{-jm\frac{2\pi}{T_0}t} dt$$

$$s_{im} = \frac{jT_0}{2\pi m T_0}\int_{t_{ion}}^{t_{ioff}} e^{-jm\frac{2\pi}{T_0}t} d\left(-jm\frac{2\pi}{T_0}t\right)$$

$$s_{im} = \frac{j}{2\pi m}\left(e^{-jm\frac{2\pi}{T_0}t_{ioff}} - e^{-jm\frac{2\pi}{T_0}t_{ion}}\right)$$

Let $\tau_{ioff} = \frac{\mathrm{t_{ioff}}}{T_0}$ and $\tau_{ion} = \frac{\mathrm{t_{ion}}}{T_0}$. We also assume $\tau_{all} = \tau_{ioff} + \tau_{ion}$ and $\tau_\delta = \tau_{ioff} - \tau_{ion}$,the s_{im} can rewrite as

$$s_{im} = \frac{j}{2\pi m}\left(e^{-j\pi m(\tau_{all}+\tau_\delta)} - e^{-j\pi m(\tau_{all}-\tau_\delta)}\right)$$

$$s_{im} = \frac{j}{2\pi m} e^{-j\pi m(\tau_{all}+\tau_\delta)}\left(e^{-j\pi m\tau_\delta} - e^{j\pi m\tau_\delta)}\right)$$

$$s_{im} = \frac{j}{2\pi m} e^{-j\pi m(\tau_{all})}(-2j \cdot sin\,(\pi m\tau_\delta)$$

$$s_{im} = \frac{1}{\pi m} e^{-j\pi m(\tau_{all})} sin\,(\pi m\tau_\delta)$$

Replace $\tau_{all} = \tau_{ioff} + \tau_{ion}$and $\tau_\delta = \tau_{ioff} - \tau_{ion}$, gives the Equation 3.10,

$$s_{im} = \frac{sin\{\pi m(\tau_{ioff}-\tau_{ion})\}}{\pi m} e^{-j\pi m(\tau_{ioff}+\tau_{ion})} \qquad \textbf{Eq.3.10}$$

APENDEX III CST MICROWAVE STUDIO SETUP

For Planar TMRA

Solver	Time-domain solver accuracy: -30 dB
Source	Plane wave
Frequency range	8.5 GHz to 10.5 GHz
Boudary conditions	OPEN (add space)
Mesh cell setup	local mesh cells were added in PIN diode regions
Monitor	9.5 Farfield monitor set at 10 meters away from TMRA
Excitation signal	Gaussian

For Parabolic TMRA

Solver	Integral Equation solver accuracy: 1e-3
Source	Imported Farfield source
Frequency range	8.5 GHz to 10.5 GHz
Boudary conditions	OPEN (add space)
Mesh cell setup	surfaces: 3 steps of wavelength
Monitor	9.5 Farfield monitor set at 10 meters away from TMRA
Excitation signal	Single frequency 9.5 GHz